POLITECNICO DI TORINO

Collegio di Ingegneria Chimica e dei Materiali

Master of Science Course in Materials Engineering

Master of Science Thesis

Impact of stereolithography process parameters on microstructure and properties of alumina manufactured parts

Supervisors: Sara BIAMINO and Diego MANFREDI

Candidate: Sophie BADIN

October 2020

Acknowledgments

Introduction

The development of additive manufacturing (AM) began in the 1980s [1]. Contrary to subtractive manufacturing where cutting tools remove material from a block, and contrary to forming manufacturing which requires a mould, AM is a family of processes in which parts are produced layer by layer.

AM has been rapidly established as a reliable fabrication route for development of prototypes and parts from polymers and then from metals. However, the interest of such technology to manufacture ceramic parts is recent. Different techniques have been studied by universities and laboratories, such as Robocasting, inkjet 3D-printing or Selective Laser Sintering (SLS) but companies are showing more and more interest in a technique called "stereolithography" (SLA).

SLA is an historical process since it was the first to be developed and to obtain a patent. This technology uses a liquid photosensitive polymer resin as feedstock, which is cured thanks to the energy of a laser beam. At the beginning, it was only possible to produce polymeric materials but recently, researchers managed to produce ceramic parts using a ceramic suspension. However, the development of this technique being relatively recent for the ceramics, it is not fully mastered yet. A lot of phenomena are not understood, and processes needs an optimization to improve material integrity and properties.

Many experiments have been carried out using alumina, a technical ceramic for which industrialists are showing more and more interest, due to its exceptional characteristics [2]. Thus, parts and components made of alumina are increasingly used in aerospace (for thermal barrier as example), in automotive, biomedical, electronics (such as electrical insulator) and other applications.

The performance of the 3D printed alumina samples is influenced by their microstructural characteristics and phase composition. The microstructural features such as shape and orientation distribution of pores noticeably affects the thermo-mechanical properties of materials [3].

Many parameters come into plays in the quality of the final part (*Figure 1*). It is then impossible to study all parameters together. Most of the research works already done focus on the suspension formulation, on process parameters such as speed and layer thickness and on post-process parameters. Indeed, the complete SLA process for ceramics includes debinding and sintering stages. Thus, post-processing parameters must be chosen carefully because they influence the final microstructure and properties.
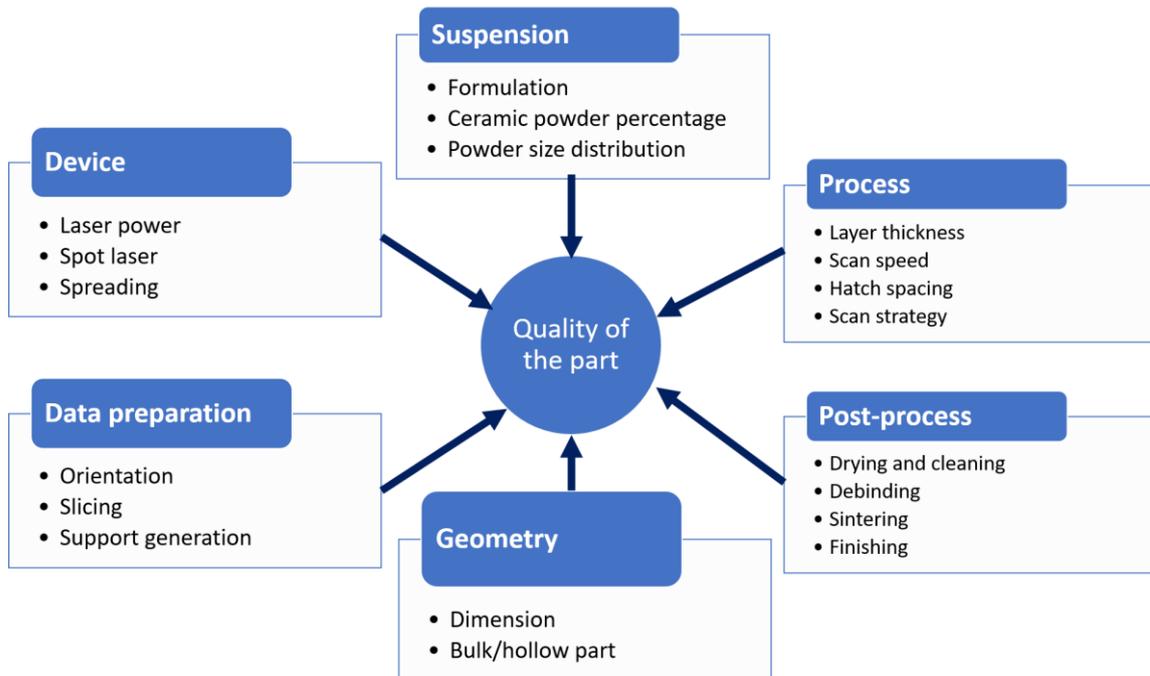
Figure 1 : Parameters influencing quality of a part in SLA

The aim of this dissertation is thus to show an overview of the works that has been carried out on the impact of the various parameters on the microstructure and on the physical properties (density, shrinkage, conductivity, etc.) and mechanical properties (stiffness, etc.). In the long term, we will try to identify the parameters to be used to obtain the best properties, with a homogeneous microstructure.

This research was supposed to be conducted at IRCER (Research Institute on Ceramics), one of the pioneer centres in SLA for ceramics parts. Unfortunately, no experiments were made because of health crisis and this master thesis is only bibliographic.

Table of contents

Riassunto in italiano

1. Contesto e obbiettivo della tesi

Lo sviluppo della fabbricazione additiva è iniziato negli anni '80. All'inizio, il suo obiettivo era quello di ridurre i tempi di produzione di modelli e prototipi, ed è solo negli anni 2000 che si è sviluppato anche il suo utilizzo per la produzione diretta di prodotti ad alte prestazioni in piccole serie. Contrariamente ai processi convenzionali, la fabbricazione additiva permette di produrre pezzi complessi in un periodo di tempo molto breve e ad un costo ridotto perché non sono necessari stampi e/o lavorazioni aggiuntive (sottrazione di materiale) [4].

La stereolitografia (SLA) è una delle prime tecniche di fabbricazione additiva ad essere nata, con attrezzature brevettate nel 1984 da Charles Hull [5]. In origine, questa tecnica permetteva la produzione di parti realizzate solo con materiali plastici, ma si è rivelata molto promettente anche per la produzione di parti in materiale ceramico. Tuttavia, poiché lo sviluppo di questa tecnica è relativamente recente per gli oggetti in materiale ceramico, non è ancora completamente padroneggiata. Molti fenomeni non sono ancora compresi e il processo deve essere ottimizzato per produrre pezzi con le migliori caratteristiche possibili.

Lo scopo di questa tesi di laurea è quindi quello di mostrare una panoramica dei lavori relativi alla stereolitografia di parti in allumina e più specificamente sull'impatto dei vari parametri sulla microstruttura e sulle proprietà fisiche e meccaniche. Si cerca così di individuare i migliori parametri da utilizzare per ottenere le migliori caratteristiche, con una microstruttura omogenea. Questa ricerca doveva essere condotta presso l'IRCER (Istituto di ricerca sui ceramici) a Limoges, uno dei centri pionieri in SLA per le parti in materiale ceramico e comprendere anche dell'attività sperimentale. Purtroppo, la parte sperimentale non è potuta partire a causa della crisi sanitaria, pertanto questa tesi è solo bibliografica.

1.1 La fabbricazione additiva

La fabbricazione additiva riunisce diverse tecnologie che rendono possibile la produzione di parti, a partire da un modello digitale, aggiungendo materiale in strati successivi. In primo luogo, un modello 3D dell'oggetto da produrre viene creato digitalmente utilizzando un software CAD (Computer Aided Design) o acquisendo digitalmente un oggetto 3D già esistente. Il modello viene poi esportato in formato STL (Standard Triangulation Language), un formato che trasforma il modello geometrico in un mesh, definendo la superficie del pezzo con un insieme di triangoli orientati. Infine, l'oggetto digitale viene tagliato da un software dedicato alla produzione additiva in una moltitudine di sezioni trasversali (chiamate "slices"), con uno spessore che varia da 25 a 100 μm [6]. Il file risultante viene inviato alla macchina da stampa 3D (*Figura 1*).
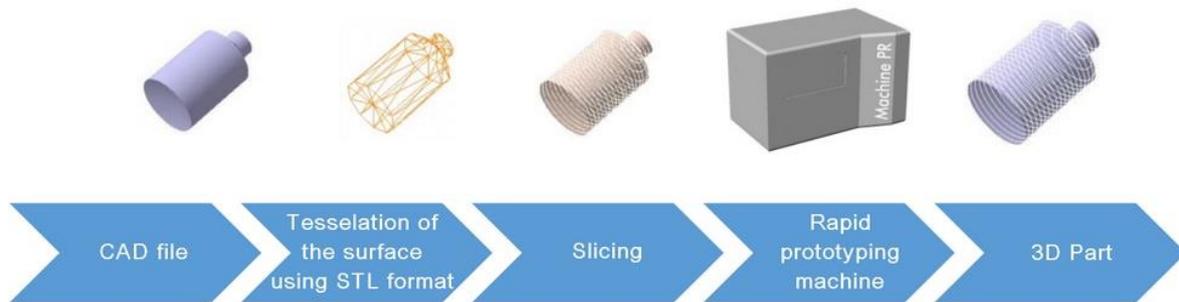
Figura 1 : Processo per la fabbricazione additiva

Le tecniche di produzione additiva possono essere classificate a seconda del tipo della materia prima (*Figura 2*).
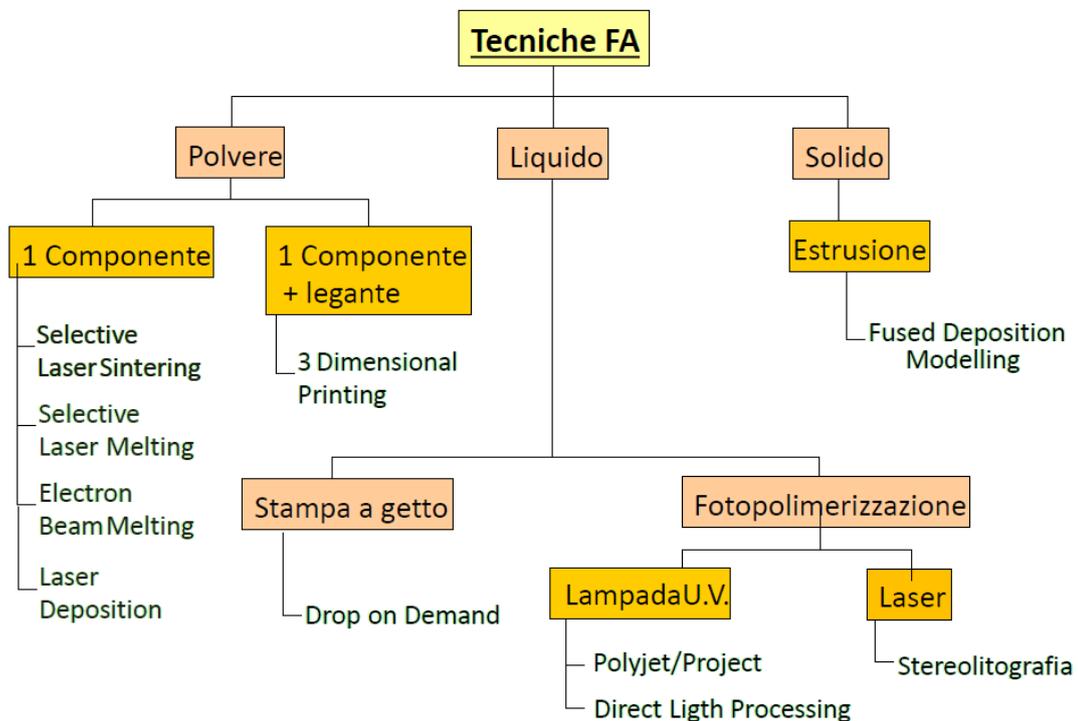
Figura 2 : Classificazione tecniche di fabbricazione additiva [4]

1.2 La stereolitografia

Un serbatoio viene riempito con una resina fotosensibile, che contiene uno o più monomeri/oligomeri e un fotoiniziatore sensibile ai raggi UV. Una piattaforma che si muove lungo l'asse Z è immersa nel serbatoio ad una profondità corrispondente ad uno "slice". Un raggio laser UV a controllo digitale scansiona la superficie lungo gli assi X e Y, seguendo il modello corrispondente ad uno strato 2D del modello numerico. Grazie all'energia del laser, si verifica una reazione di polimerizzazione e le aree scansionate si induriscono. La piattaforma scende poi con un incremento, definito come lo spessore di uno "slice", e viene rivestita con un nuovo strato di resina liquida utilizzando un sistema di distribuzione [7]. L'operazione viene poi ripetuta fino alla completa realizzazione del pezzo (*Figura 3*).
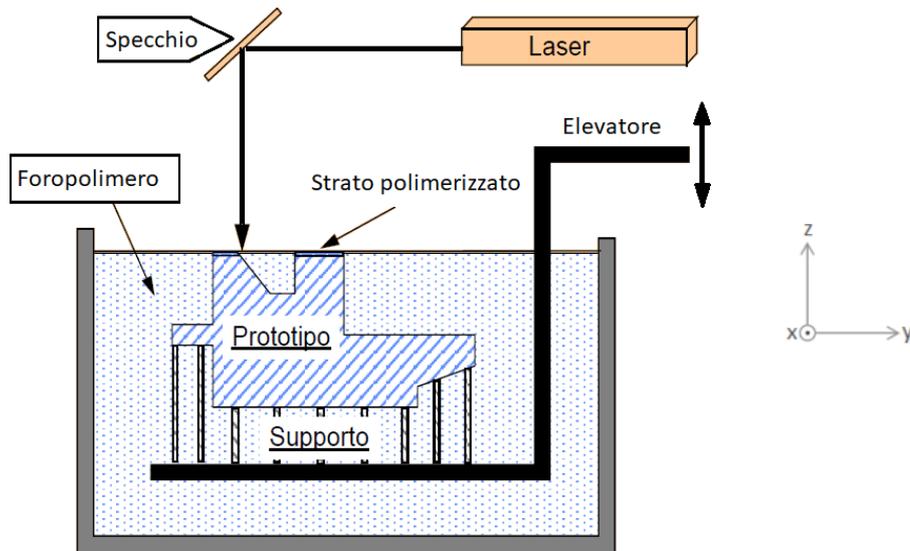
Figura 3 : Stereolitografia [4]

Per la produzione di parte in materiale ceramico mediante stereolitografia, si usa la resina fotosensibile caricata con polvere ceramica (dal 50 al 65% in massa), nonché un disperdente, al fine di aumentare la stabilità della pasta (evitando sedimentazione e agglomerati di polvere). Durante il processo di produzione, il sistema fotosensibile si indurisce sotto l'azione della radiazione laser UV e le particelle ceramiche vengono "intrappolate" in una matrice polimerizzata [8].

Sebbene il processo di progettazione e produzione sia lo stesso che per le materie plastiche, alla fine del processo, la parte ceramica che ne risulta è una parte grezza, detta «verde». Le fasi di deceratura e sinterizzazione devono quindi essere effettuate per ottenere una parte densa. La fase di deceratura consiste nell'eliminazione del legante polimerico ed è una fase molto delicata perché può portare a cricche e/o deformazioni del pezzo. Al termine del processo di deceratura, il pezzo è costituito esclusivamente da un aggregato di particelle ceramiche a bassa coesione [8]. È quindi necessaria una fase di sinterizzazione per consolidare la parte e densificarla. La forza motrice della sinterizzazione, attivata dalla temperatura, è la riduzione dell'energia superficiale della polvere attraverso meccanismi di diffusione allo stato solido [9].

La densificazione, che corrisponde ad un'eliminazione della porosità, porta ad una diminuzione generale del volume del pezzo, chiamato "ritiro". Questo ritiro di sinterizzazione del pezzo deve essere tenuto in considerazione durante la fase CAD, così come ogni possibile deformazione del pezzo. In questo modo viene creato un primo pezzo e le dimensioni del pezzo digitale vengono adeguate dopo il calcolo del ritiro.

2. Allumina

Il materiale che è stato scelto come caso studio in questa tesi è l'allumina (Al_2O_3), perché la maggior parte degli studi di ricerca sono stati realizzati proprio con questo materiale, che è di crescente interesse per il settore industriale. L'allumina si trova naturalmente nella bauxite, dov'è idratata e mescolata con ossido di ferro. Questa allumina viene poi estratta dalla bauxite e viene utilizzata principalmente per produrre alluminio. Tuttavia, l'allumina ad alta purezza

può essere utilizzata in una varietà di applicazioni ingegneristiche, nell'industria elettronica, aerospaziale, automobilistica, biomedica e in altri settori. Questi campi sfruttano le notevoli proprietà dell'allumina, ovvero la sua resistenza alle alte temperature, l'elevata rigidità e durezza e la resistenza alla corrosione e all'usura. Inoltre, l'allumina è un isolante elettrico, una proprietà molto utile per le applicazioni elettroniche [10]. La *Tabella 1* riporta alcune proprietà dell'allumina a secondo il grado di purezza. I gradi A1-A5 sono gradi di alta purezza con almeno il 99% di allumina e i gradi A6 e inferiori sono gradi meno puri, contenente dal 80% al 99% di allumina.

Tabella 1 : Proprietà dell'allumina prodotta con processi convenzionali [10]

Grado	Al2O3	%Porosità	Modulo di Young (GPa)	Resistenza a flessione media (MPa)
A1	≥ 99.6	0 - 2	380 - 410	210-500
A2	≥ 99.8	<1	380 - 405	150-450
A3	≥ 99.5	<1	398 - 400	300-600
A4	≥ 99.6	3 - 6	340 - 380	150-450
A5	≥ 99.0	1 - 5	340 - 380	150-500
A6	96.5 – 99.0	1 - 5	340 - 375	150-450
A7	94.5 - 96.5	1 - 5	300 - 370	180-360
A8	86.0 - 94.5	2 - 5	260 - 330	150-350
A9	80.0 - 86.0	3 - 6	260 - 330	200-300

3. Parametri che influenzano la qualità del pezzo finale

3.1 Fattori

Molti fattori entrano in gioco nel processo di stereolitografia (*Figura 4*). Questi fattori sono sia legati al sistema fotosensibile utilizzato, sia ai parametri di produzione (velocità del raggio laser, potenza del raggio laser, spessore dello strato, ecc.), o ancora ai parametri di post-processo.
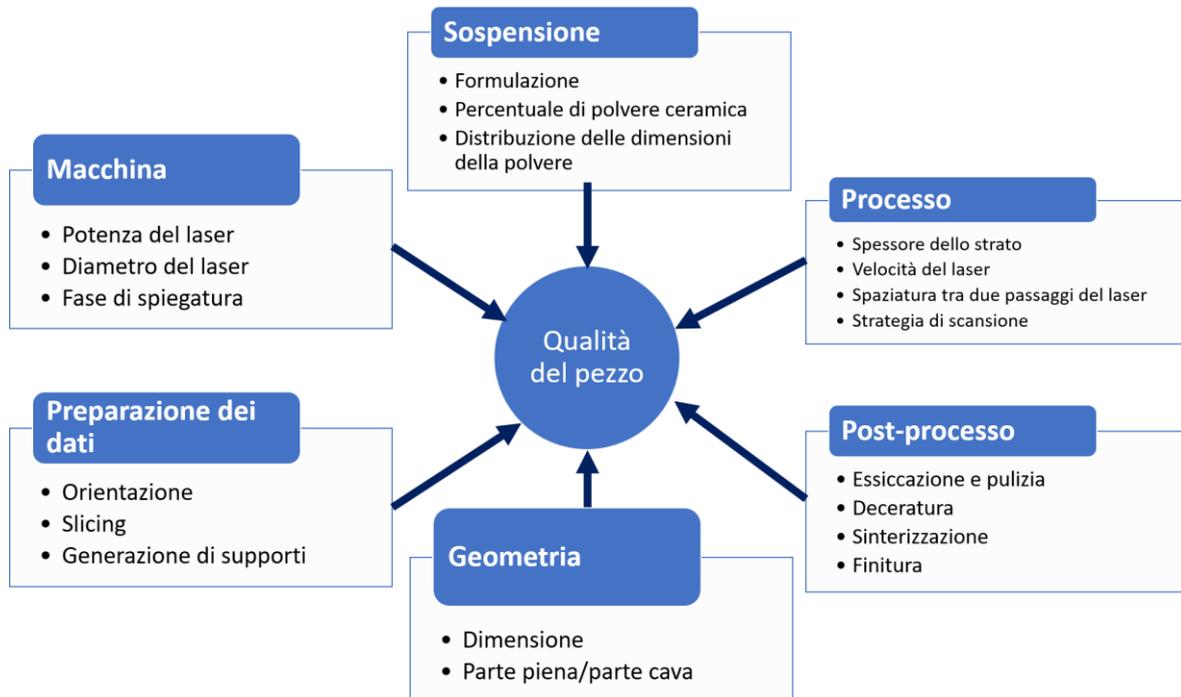
Figura 4 : Parametri che influenzano la qualità del pezzo finale

3.2 Esposizione

Durante il passaggio del laser UV, il materiale riceve una certa esposizione, definita come il tasso di energia ricevuta dal sistema fotosensibile per unità di superficie (E), espresso in mJ/cm² [8]. Questa esposizione dipende dalla profondità z e dalla distanza dal centro del fascio y (*Figura 5*).
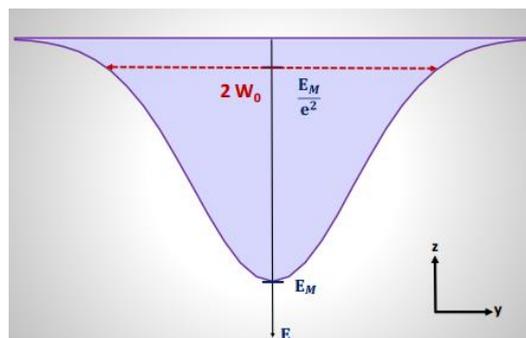
Figura 5 : Vista schematica bidimensionale dell'esposizione [8]

Per un raggio laser presumibilmente gaussiano, la sua espressione è data dalla seguente formula [11] :

$$E(y,z) = \sqrt{\frac{2}{\pi}} \left(\frac{P_L}{v_L W_0}\right) \exp\left(-\frac{2y^2}{W_0{}^2}\right) \exp\left(-\frac{z}{D_p}\right) \qquad \text{Eq. 1}$$

Con:

- P_L la potenza laser in W

- W_0 il raggio dello spot laser gaussiano in m

- V_L la velocità di scansione del laser in m/s

- D_p la profondità di penetrazione del laser in m

Affinché si verifichi la reazione di polimerizzazione, il sistema deve essere sottoposto almeno all'energia di polimerizzazione critica (E_C), che è un parametro intrinseco al sistema fotosensibile. Quindi, per avere una reazione di polimerizzazione, si deve avere $E(y,z) > E_C$. Inoltre, per garantire un buon legame chimico tra gli strati, la profondità di polimerizzazione deve superare la profondità del singolo "slice".

3.3 Profondità di polimerizzazione e profondità di penetrazione laser

La profondità di polimerizzazione (C_d) è un parametro importante che determina l'omogeneità della polimerizzazione e quindi l'accuratezza della formabilità. La sua espressione è data dall'Eq. 2.

$$C_d = D_p \ln \frac{E_M}{E_C} \qquad \text{Eq. 2}$$

$$D_p = \frac{2d}{3Q\phi} \qquad \text{Eq. 3}$$

$$Q = \left(\frac{\Delta n}{n0}\right)^2 \left(\frac{d}{\lambda}\right)^2 \qquad \text{Eq. 4}$$

dove E_M è l'esposizione massima, d è la dimensione media delle particelle della polvere di ceramica, ϕ è la frazione di volume della polvere di ceramica nella sospensione, λ è la lunghezza d'onda dell'irradiazione, $n0$ è l'indice di rifrazione della resina, Δn è la differenza di indice di rifrazione tra la polvere di ceramica e la soluzione di monomero.

Nei paragrafi successivi sono riportati i principali risultati ottenuti dai ricercatori sull'impatto di alcuni di questi parametri sulle caratteristiche delle parti in allumina prodotte.

4. Principali risultati

4.1 Impatto del feedstock sulla densità delle parti sinterizzate

Come visto con l'equazione 3, D_p è funzione della concentrazione volumetrica della polvere, del diametro delle particelle e della differenza di indice di rifrazione tra la soluzione polimerizzabile UV e la polvere ceramica [12]. È quindi possibile modificare la profondità di penetrazione del laser, e di conseguenza la profondità di polimerizzazione, regolando la dimensione delle particelle, che permetterà, tra le altre cose, di soddisfare i requisiti di formabilità e sinterizzabilità.

Wu et al. [13] hanno deciso di testare diverse dimensioni di particelle di allumina in sospensione per stampare parti in stereolitografia e di valutare diversi trattamenti di deceratura (in aria o sottovuoto). Hanno testato una sospensione con solo polveri di dimensioni micrometriche di 9 µm (campione 1), un'altra con solo polveri di dimensioni nanometriche di 50 nm (campione 3) e, infine, hanno testato una sospensione che aveva contemporaneamente polveri nanometriche e polveri micrometriche (campione 2) con un rapporto in peso di 1:1.

Le morfologie ottenute dopo deceratura e sinterizzazione sono mostrate in *Figura 6*. Nessun campione mostra difetti, come cricche o delaminazioni, dopo la sinterizzazione, nemmeno il campione 2 la cui microstruttura del pezzo verde era disomogenea.
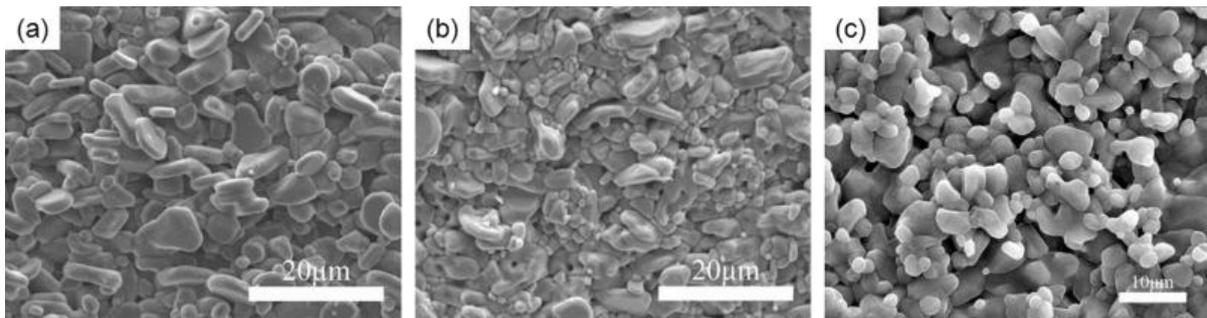
Figura 6 : Immagini al SEM che rivelano la morfologia dei campioni sottoposti al processo di deceratura termica: a) campione 1, b) campione 2, c) campione 3. [13]

Per quanto riguarda le densità (*Figura 7*), i risultati mostrano che la densità dei campioni contenenti contemporaneamente particelle sia di dimensioni micrometriche che di dimensioni nanometriche (campione 2) è largamente superiore a quella della polvere di dimensioni micrometriche (campione 1) e leggermente superiore a quella della polvere di dimensioni nanometriche (campione 3). Nel campione 2 (*Figura 6(b)*) nanoparticelle sferiche di allumina occupano gli spazi vuoti tra i grani di dimensioni microscopiche, e questa combinazione spiega perché la densità di questo campione è la più alta tra le altre. L'utilizzo di una distribuzione bimodale è quindi un approccio fattibile e a basso costo per ottenere parti più dense.
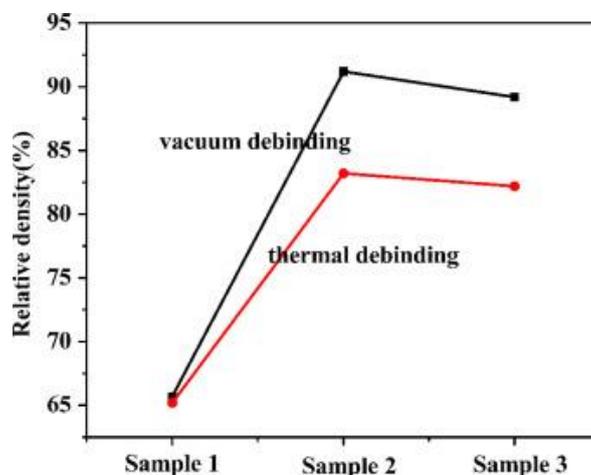
Figura 7 : Confronto delle densità relative dei diversi campioni dopo deceratura. Sia deceratura sottovuoto (vaccum debinding) che deceratura termica (thermal debinding) [13]

4.2 Impatto dei parametri di stampaggio

Come mostrato nell'equazione 1, il valore dell'esposizione all'interno del sistema fotosensibile dipende sia dai parametri intrinseci del sistema fotosensibile (E_C e D_p), dal parametro intrinseco alla sorgente laser (W_0) ma anche dai parametri di produzione V_L e P_L.

J. Tarabeux [8] e K. Cieżki [14] hanno studiato nove combinazioni di parametri di stampa V_L e P_L, che portano a diversi valori di esposizione (*Tabella 2* dove E_{10L} è la massima esposizione ricevuta da dieci strati continui di pasta di allumina) ed è stato studiato l'effetto sul modulo di Young dei campioni verdi e sinterizzati e sulla densità e resistenza a frattura dei campioni sinterizzati prodotti. I campioni sinterizzati sono stati sottoposti a deceratura per 30 minuti a 30°C e sinterizzazione per 2 ore a 1650°C, entrambi in aria.

Tabella 2 : Piano prove sperimentali

Esperienza	E01	E02	E03	E04	E05	E06	E07	E08	E09
E_{10L}(mJ/cm²)	465,7	222,2	170,0	434,6	238,6	362,2	776,0	598,7	310,4

4.2.1 Modulo di Young dei campioni verdi

I moduli di Young variano da 970 MPa per E03 a 1580 MPa per E08, cioè una differenza di 610 MPa tra il modulo più basso e quello più alto. Pertanto, il controllo della rigidità delle parti verdi richiede un'attenta scelta dei parametri di produzione.

Nel confrontare il modulo di Young e l'esposizione E_{10L}, hanno trovato che i due parametri sono collegati in modo quasi lineare su una scala semi-logaritmica, con un coefficiente di correlazione di 0,97. L'ipotesi di linearità è rafforzata dal fatto che con la regressione lineare (in rosso in *Figura 8*) si ottiene un modulo di Young pari a zero per un'esposizione di 20 mJ/cm², valore che corrisponde all'energia di polimerizzazione critica del sistema studiato. Così, quando l'esposizione è approssimativamente uguale all'energia critica di polimerizzazione, il sistema è liquido e quindi il valore del modulo diventa zero [8].
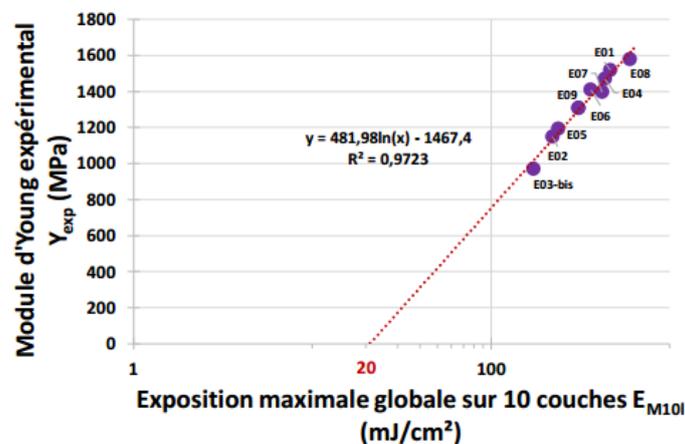
Figura 8 : Modulo di Young in funzione di E_{10L} per le parti in allumina verde (Moduli di Young in ordinata e E_{10L} in ascisse) [8]

4.2.2 Densità dei campioni sinterizzati

I valori di densità, ottenuti per i pezzi sinterizzati, sono simili per tutti i campioni, indipendentemente dal tasso di esposizione, e vanno da 3,75 a 3,78 g/cm^3. Questi valori corrispondono ad una densità relativa del 95%. Pertanto, le misure non mostrano un'influenza significativa della scelta dei parametri di processo della stereolitografia sulle densità ottenute [8]. Possiamo pertanto dire che la densità che si ottiene dopo sinterizzazione è maggiormente influenzata dal feedstock di partenza piuttosto che dai parametri di processo veri e propri. Tuttavia, il relatore di J. Tarabeux e K. Ciężki mi ha oralmente comunicato che questi risultati sembrano singolare e che forse le misure sono state fatte in modo sbagliato. Sarebbe quindi interessante fare di nuovo questi esperimenti.

4.2.3 Modulo di Young dei campioni sinterizzati

I moduli di Young trovati per i campioni sinterizzati variano da 270 a 402 GPa (*Figura 9*), valori in linea con quelli trovati in letteratura (*Tabella 1*) per le parti in allumina prodotte con processi convenzionali. Nella *Figura 9,* E_{33} corrisponde al modulo di Young parallelo alla direzione di stampa e E_{11} corrisponde al modulo di Young perpendicolare alla direzione di stampa. Per tutti i test eseguiti, i valori del modulo di Young E_{11} ed E_{33} seguono generalmente la stessa evoluzione dell'esposizione E_{10L}. Pertanto, i parametri di stampa, che influenzano l'esposizione, giocano un ruolo importante nella rigidità delle parti sinterizzate [14].
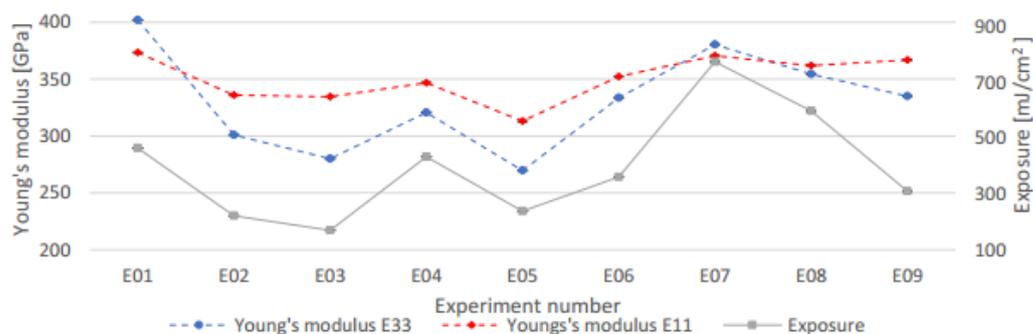
Figura 9 : I moduli di Young e l'esposizione secondo le diverse esperienze (exposure = esposizione) [14]

Si noti anche che E_{33} è mediamente inferiore a E_{11} per la maggior parte dei campioni. Questa differenza si spiega con il fatto che in stereolitografia le parti vengono prodotte strato per strato secondo Z o 3 (direzione di stampa), creando una microstruttura anisotropa. Infatti, spesso una delaminazione è presente nella microstruttura tra gli strati lungo l'asse Z (*Figura 10*), che indebolisce la parte lungo questa direzione.
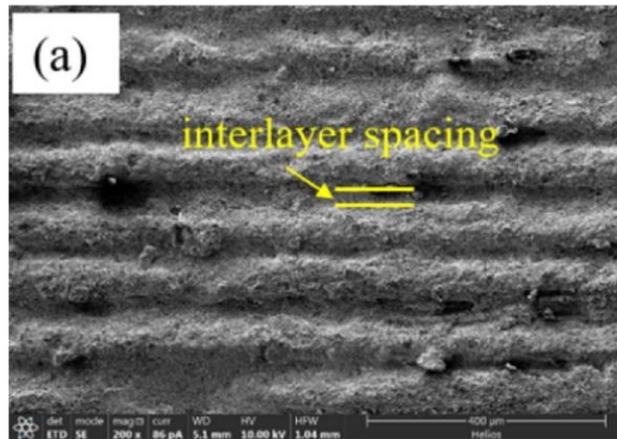
Figura 10 : Esempio di un'immagine al SEM che mostra la delaminazione dopo sinterizzazione (qui a 1100°C) di una superficie lucidata[15]

Pertanto si può trarre la seguente conclusione: un tasso di esposizione più elevato induce un indurimento maggiore del verde grazie alla maggior polimerizzazione del sistema ceramico. Inoltre, la profondità di polimerizzazione dipende dal valore dell'esposizione cioè maggiore è l'esposizione, maggiore è la profondità di polimerizzazione e quindi maggiore è la quantità di pasta polimerizzata. Pertanto, maggiore è l'esposizione, migliore è il legame tra gli strati del materiale al verde e questo inevitabilmente si rifletterà sull'adesione degli strati dopo sinterizzazione.

4.2.4 Resistenza a rottura per i campioni sinterizzati

I valori di resistenza a rottura ottenuti con testi di flessione biassiale vanno da 107 MPa a 164 MPa, valori inferiori a quelli ottenuti in letteratura per le parti prodotte con processi convenzionali. Infatti, sui pezzi fabbricati per pressatura, i valori di sollecitazione ottenuti per flessione biassiale sono compresi tra 350 e 550 MPa (*Tabella 1*). Questa differenza può essere spiegata dalla porosità elevata trovata nei campioni fabbricati con stereolitografia.

Come per il modulo di Young, la curva della resistenza a rottura segue la stessa evoluzione dell'esposizione. Questo risultato indica per la seconda volta che l'esposizione ricevuta durante la produzione di parti verdi ha un impatto sul comportamento meccanico delle parti sinterizzate.

4.3 Impatto dello spessore dello strato sulle proprietà e sulla microstruttura

Li et al. [16] hanno studiato l'impatto dello spessore di strato sulla microstruttura e sulle proprietà meccaniche delle parti in allumina allo stato verde e sinterizzata. Hanno testato 4 diversi spessori, da 30 µm a 120 µm con un passo di 30 µm, mantenendo costanti tutti gli altri parametri.

Per strati di 30 µm non si vede alcuna interfaccia fra gli strati ma una sezione trasversale perfettamente continua (*Figura 11 (a)*). Ciò significa che per strati sottili l'adesione grazie alla polimerizzazione di ogni strato è molto buona. Tuttavia, per gli strati più spessi (da 60 µm a 120 µm) sono visibili linee parallele evidenziate dalle frecce nere sulle relative immagini

(*Figura 11 (b), (c) e (d)*). I ricercatori attribuiscono la presenza di queste linee ad un insufficiente adesione tra gli strati adiacenti, causato da una limitata profondità di penetrazione nella sospensione. Questi risultati mostrano quindi che quanto più spessi sono gli strati, tanto maggiore è il rischio di delaminazione a causa di una scarsa adesione tra gli strati.
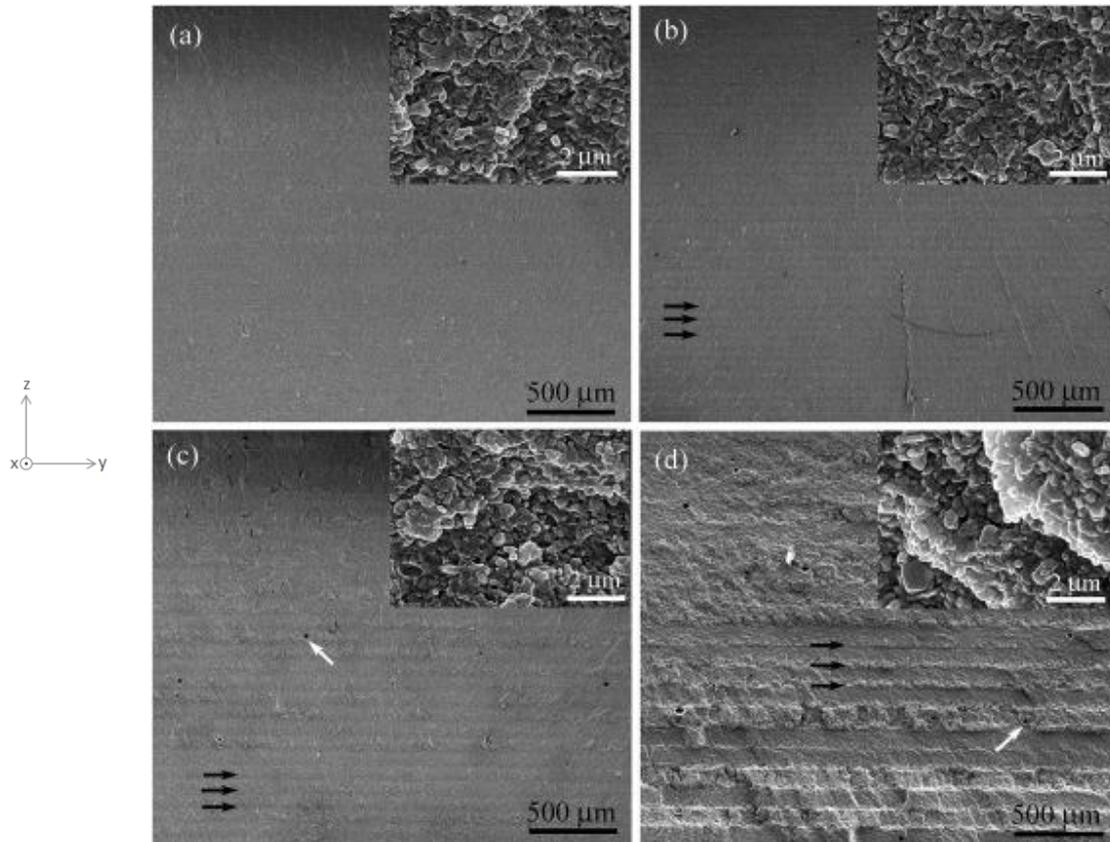
Figura 11 : Micrografie di campioni verdi con diversi spessori di strato: a) 30 µm; b) 60 µm; c) 90 µm; d) 120 µm. [16]

Grazie all'ingrandimento visibile in alto a destra delle immagini, si può notare che le polveri ceramiche sono interconnesse dal legante polimerizzato e distribuite uniformemente per i campioni con strati da 30 µm, 60 µm e 90 µm. Tuttavia, per il campione con strati da120 µm, la distribuzione non è uniforme e le polveri tendono ad agglomerarsi, con conseguente morfologia più irregolare e rugosa.

Per quanto riguarda le porosità (misurata con ingrandimento al SEM), quest'ultima inizia ad essere critica quando lo spessore raggiunge i 90 µm (frecce bianche sulle *Figura 11 (c) e (d)*). I pori sono probabilmente generati dalla formazione di bolle durante la fase di deposizione della sospensione ceramica. Questi pori possono ridurre notevolmente la resistenza del componente dopo la sinterizzazione perché non riescono ad essere eliminati durante la sinterizzazione stessa.

La durezza ed il modulo elastico sono stati tracciati in funzione dello spessore dello strato (*Figura 12*).
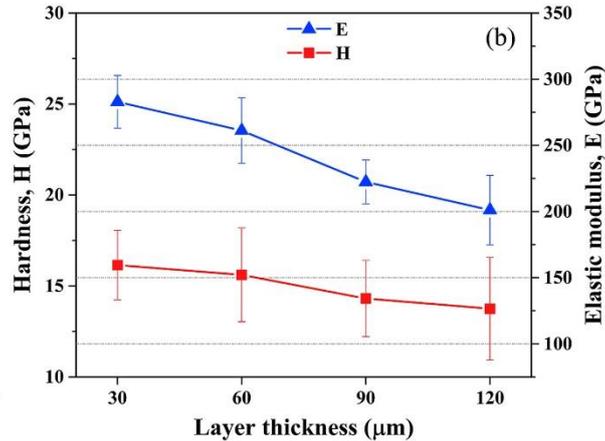
Figura 12 : Variazione di durezza e di modulo di Young per i quattro campioni (Hardness = durezza; Layer thickness = Spessore di strato; Elastic modulus = Modulo di Young) [16]

Il valore medio della durezza (H) diminuisce leggermente con l'aumentare dello spessore di strato, da 16,15 ± 1,91 GPa a 13,75 ± 2,82 GPa. Mentre il modulo di Young (E) diminuisce più bruscamente con l'aumento dello spessore dello strato. Questi effetti sono imputabili alla minor densità relativa associata ad uno spessore dello strato più elevato.

4.4 Impatto dei parametri post-processo sulla microstruttura e sulle proprietà

4.4.1 Proprietà e microstruttura prima e dopo post-processo

F. Azarmi et al. [17] [3] hanno cercato di valutare le caratteristiche microstrutturali e le proprietà delle parti in allumina prodotte mediante stereolitografia, prima e dopo deceratura e sinterizzazione. Per il campione verde, il modulo di Young medio misurato era di 15,3 GPa e per il campione dopo deceratura e sinterizzazione, era di 363,3 GPa. Come nella tesi di dottorato di J. Tarabeux [8], i risultati mostrano che la stereolitografia è un processo affidabile in quanto la rigidità trovata dopo sinterizzazione è simile a quella dei campioni realizzati con metodi convenzionali. Tuttavia, J. Tarabeux [5] ha trovato un modulo di Young di 1,5 GPa per i campioni verdi, cioè un ordine di grandezza inferiore a quello trovato da F. Azarmi e I. Sevostianov [14]. Questa differenza è difficile da spiegare, poiché entrambi hanno usato una pasta di allumina commerciale di 3DCeram. Pertanto, è probabilmente dovuta a diversi parametri di stampaggio (sconosciuti per F. Azarmi e I. Sevostianov) o alle diverse tecniche utilizzate per la caratterizzazione (prove di microtrazione per J. Tarabeux e metodo della vibrazione a flessione per F. Azarmi e I. Sevostianov).

Inoltre, risultati hanno mostrato che il coefficiente di conducibilità termica aumenta tra il campione verde e il campione sinterizzato (*Tabella 3*). Il valore ottenuto per il campione dopo sinterizzazione è nell'intervallo riportato per i campioni di allumina sinterizzata prodotti con metodi convenzionali.

Campione	Coefficiente di conducibilità termica W/m°C
Verde	5.17 ± 1.05
Dopo deceratura	8.37 ± 1.78
Dopo deceratura e sinterizzazione	26.81 ± 3.5
Allumina (α-Al$_2$O$_3$) – Altamente porosa	$7{-}10$
Allumina (α-Al$_2$O$_3$) - Pressato a freddo, sinterizzato	$22{-}30$

4.4.2 Influenza del tipo di essiccazione sull'integrità del materiale

Zhou et al. [18] hanno dimostrato che asciugare le parti tramite polietilene glicole (PEG), un essiccante liquido, era più adatto, poiché con questo metodo di essiccazione il ritiro era omogeneo e non appariva alcuna deformazione, contrariamente all'essiccazione tradizionale in aria (*Figura 13*). Hanno inoltre ottenuto una densità più elevata con l'utilizzo del PEG.
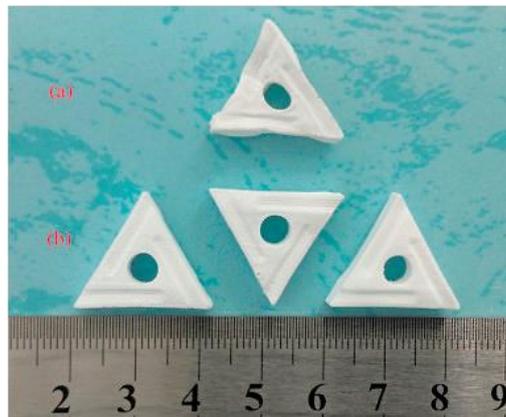
Figura 13 : (a) Campione verde essiccato attraverso un processo di essiccazione naturale e (b) campioni verdi essiccati tramite un processo di essiccazione assistita da un liquido essiccante (PEG) *[18]*

4.4.3 Influenza del tipo di deceratura sui difetti e sulla densità delle parti in allumina

Sono stati testati tre diversi cicli di deceratura da Zhou et al. [18]: una pirolisi in aria, una deceratura sottovuoto e un profilo di deceratura in due fasi che consiste in una fase sottovuoto seguita da una pirolisi in aria. La deceratura per pirolisi in aria e il profilo di deceratura sottovuoto sono mostrati in *Figure 8.3(a)*, e il profilo di deceratura in due fasi è mostrato in *Figure 8.3(b)*. Tutti i campioni sono poi stati sottomessi allo stresso ciclo di sinterizzazione (fino a 1650°C).
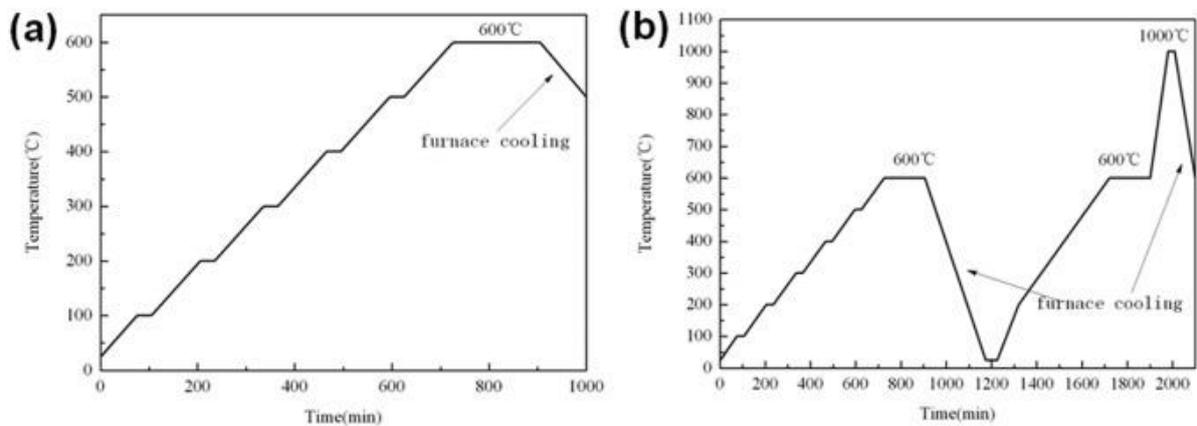
Figura 14 : (a) Deceratura per pirolisi ad aria e deceratura sottovuoto e (b) Decetura in due fasi. [18]

La deceratura in aria ha portato ad un numero elevato di difetti macroscopici. Gli autori attribuiscono questi difetti "all'altissimo tasso di pirolisi del composto organico". Durante la pirolisi, il gas si crea a causa della decomposizione non può fuoriuscire dal campione, generando un'alta pressione all'interno del corpo che si traduce in delaminazione e cricche.

Il tasso di pirolisi può essere abbassato utilizzando il vuoto perché il gas, durante la deceratura, può fuoriuscire più facilmente dai canali tra le particelle del corpo ed è per questo che i ricercatori hanno provato la deceratura sottovuoto. Tuttavia, anche se hanno osservato meno difetti, sono apparse anche alcune cricche, probabilmente perché il carbonio residuo nel campione dopo deceratura produce gas durante il processo seguente di sinterizzazione

Infine, per ottenere pezzi senza difetti, hanno adottato una deceratura in due fasi. Il primo passo è identico alla deceratura sottovuoto e il secondo passo, in aria, è stato fatto secondo la *Figure 8*.3*(b)*. Questa seconda fase ha lo scopo di eliminare il carbonio residuo prima del processo di sinterizzazione. Con questo terzo metodo non sono stati osservati difetti, quindi sembra essere il metodo più appropriato. Tuttavia, la deceratura è almeno due volte più lunga della semplice pirolisi ad aria o sottovuoto e i produttori dovranno scegliere tra un metodo con meno difetti o più rapido.

4.4.4 Microstruttura e proprietà in base alla temperatura di sinterizzazione

Li et. al [15] hanno studiato l'evoluzione della microstruttura e delle proprietà in funzione della temperatura di sinterizzazione dei campioni di allumina prodotti da SLA e sinterizzati sottovuoto. L'uso del vuoto ha lo scopo di eliminare la formazione di difetti come le cricche causate dal carbonio residuo durante la sinterizzazione e per un migliore controllo del ritiro e quindi della deformazione. La temperatura di deceratura è la stessa per tutti gli esperimenti (deceratura in un forno a muffola), ma sono state testate sette diverse temperature di sinterizzazione, da 1100°C a 1350°C con 50°C di differenza tra ogni temperatura.

Per tutte le temperature di sinterizzazione studiate, i campioni mostrano della delaminazione (*Figura 10*). L'evoluzione della distanza tra gli strati è mostrata nella *Figura 15*. L'allumina sinterizzata a 1100°C ha una maggiore distanza tra gli strati ("interlayer spacing" sulla *Figura 10)* rispetto a tutti gli altri campioni sinterizzati a temperature più elevate. Questa distanza è

dovuta alla volatilizzazione della resina che c'è stata durante il processo di deceratura, che lascia una bassa adesione tra gli strati che non riesce ad essere recuperata durante una sinterizzazione condotta a 1100°C. Quando la temperatura raggiunge i 1150°C-1250°C, la forza motrice del processo di sinterizzazione aumenta e favorisce un migliore legame tra gli strati. Tuttavia, una volta che la temperatura raggiunge i 1300°C, il ritiro del campione aumenta notevolmente, causando un aumento notevole della delaminazione tra gli strati.
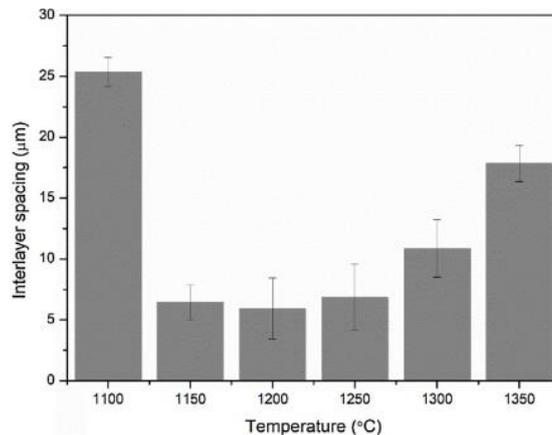
Figura 15: Evoluzione della spaziatura tra gli strati a diverse temperature di sinterizzazione [15]

Un'analisi del ritiro mostra che il ritiro aumenta con la temperatura di sinterizzazione e che è diverso a seconda della direzione considerata (*Figura 16*). Il ritiro è simile nelle direzioni X e Y ma è maggiore nella direzione Z. Questo ritiro maggiore è probabilmente dovuto ai deboli legami tra gli strati lungo la direzione Z e quindi al maggior tasso di porosità che non vengono recuperate in sinterizzazione.
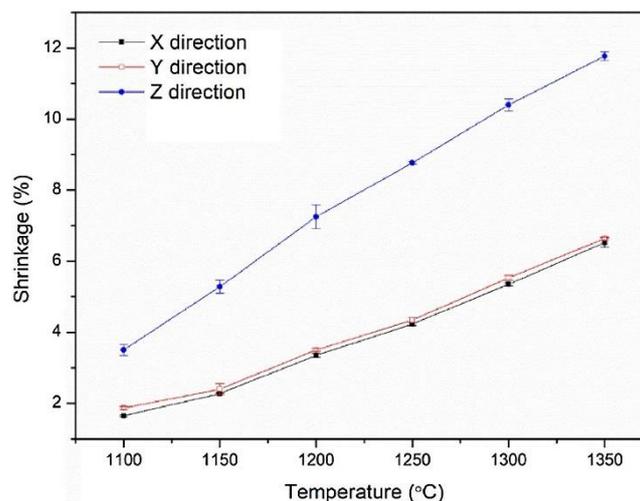
Figura 16: Ritiro in campioni sinterizzati a diverse temperature sotto vuoto [15]

La densità apparente è aumentata da 2,4 a 2,9 g/cm^3 e la porosità aperta è diminuita dal 38,7% al 23,8%, mentre la temperatura di sinterizzazione è aumentata da 1100 a 1350 °C. Inoltre, hanno mostrato che più alta è la temperatura di sinterizzazione, maggiore è la resistenza alla flessione grazie alla diminuzione della porosità. E da notare che in questo studio, non si cerca

ad ottenere pezzi densi perché i ricercatori cercano a produrre anime in ceramica ("ceramic cores" in inglese) e di conseguenza, è necessaria una porosità superiore al 20%.

Conclusione e prospettive future

Gli studi finora condotti mostrano che tutti i parametri di processo, dalla materia prima ai parametri post-processo, devono essere selezionati in modo appropriato. Nel complesso, una sospensione contenente una distribuzione di particelle bimodali dà una densità più elevata rispetto ad una distribuzione unimodale. In secondo luogo, più alto è il valore di esposizione, più rigide e resistenti sono le parti. Più sottili sono gli strati, più alta è la durezza e la rigidità. Infine, l'essiccazione con un essiccante liquido è più adatta dell'essiccazione ad aria e la deceratura sottovuoto è migliore di una deceratura ad aria. Inoltre, la temperatura di sinterizzazione non deve essere né troppo bassa perché risulterebbe non efficace né troppo elevata poiché ciò aumenta il rischio di delaminazione.

Tuttavia, è difficile confrontare gli studi e di dare valori precisi da utilizzare per avere le migliori caratteristiche perché molto dipende dalle specifiche attrezzature e modalità utilizzate dai diversi gruppi di ricerca. I ricercatori, infatti, utilizzano condizioni diverse: resine con diverse formulazioni, diversi tipi di post-lavorazione, ecc. Inoltre, il più delle volte non specificano i parametri utilizzati, come la velocità, la potenza, ecc. mentre per confrontare i risultati, è necessario che le condizioni siano le stesse. Così, in futuro, sarebbe interessante fare gli stessi esperimenti ma sempre nelle stesse condizioni, con lo stesso dispositivo, la stessa quantità di polvere, gli stessi parametri di deceratura e sinterizzazione, ecc. Inoltre, è importante notare che per passare a processi di tipo industriale si dovrà spesso scegliere tra prestazioni e tempi di costruzione. Per esempio, le parti con strati sottili presentano migliori proprietà meccaniche ma sono molto più lunghe da produrre, così come l'utilizzo di deceratura in due fasi.

1. Alumina

1.1. Generality on ceramics

To begin with, it is essential to define what a ceramic material is, and to situate it in relation to other materials. As a reminder, a "material" is a solid that has properties of use, i.e. that "serves a purpose" [19].

From a chemical point of view, the composition of ceramics corresponds to a combination of metallic atoms (such as aluminium, calcium, titanium, cerium...) with non-metals or metalloids (oxygen, carbon, nitrogen, boron and silicon). The only ceramics that do not correspond exactly to this criterion are a very small number of covalent compounds of boron and silicon with nitrogen and carbon, with special properties: Si_3N_4, SiC, BN, B_4C and B_4C_3. However, to be qualified as "ceramic", a material must have undergone shaping followed by a passage at high temperature during its manufacturing process. In almost all cases, the high-temperature step (generally over 800°C) is a baking, which causes what is called "sintering" (detailed later). This criterion eliminates many possible combinations of atoms since the solid under consideration cannot be fired. For example, sodium chloride (NaCl) is indeed a solid composed of a metal (sodium Na) and a non-metal (chlorine Cl) but it is not a ceramic because it is not possible to make parts from sodium chloride by shaping and baking [19].

1.2. Refractory ceramics

Refractory ceramics are structural ceramics that resist at high temperatures. According to the standards (ISO/R836 and AFNOR NF B 40-001), refractory materials are materials and products other than metals and alloys (without excluding those containing a metallic component), which have a pyroscopic resistance equivalent to at least 1500°C. It means that refractory materials must withstand a minimum temperature of 1500°C without softening and without collapsing under their own weight according to the pyroscopic strength test standard. This standardised test [ISO 528 1983: Refractories - Determination of pyroscopic strength (refractoriness)] consists of determining a "sagging temperature" using reference fusible watches (pyroscopic cones) under specified conditions. *Figure 1.1* shows a fusible cone before and after firing at a given temperature [20].
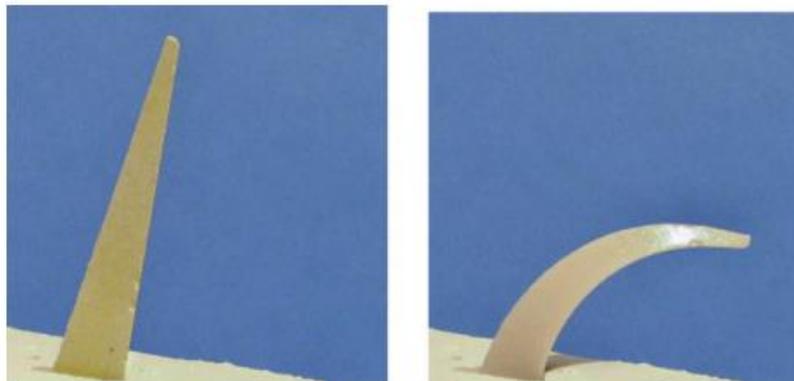
Figure 1.1 : Temperature measurement using fuse watches [20]

Refractory ceramics are mainly composed of oxides, sometimes carbides, nitrides whose melting temperature is very high. They keep their cohesion without significant dimensional change up to their limit temperature of use. Above this temperature, a progressive melting occurs.

Refractories perform several functions [20]:

- **Barrier** function: to ensure the safety of personnel and protect industrial installations operating at high temperatures.

- **Thermal insulation** function: to contain heat within equipment with limited heat losses.

- **Container** function: to confine solid, liquid or gaseous charges in containers (furnaces, reactors) at high temperatures without altering their composition and to transport gases, solids or hot liquids in pipes.

1.3. Classification

The variety of refractory ceramics is such that their classification can be approached in different ways: by the chemistry and mineralogy of the main constituent or by the density and the porosity of the ceramic [20].

- **Classification by the chemistry**

There are three families:

- **Acid refractories** of the SiO_2-Al_2O_3 system, made of silica, clay, andalusite, mullite, bauxite and alumina, as raw material.

- **Basic refractories** made from raw materials of magnesia, dolomite, chromite. These refractories have a much higher initial melting temperature than the refractories of the SiO_2-Al_2O_3 family.

- **Special refractories**, made from a wide variety of raw materials such as zirconia, ZrO_2-SiO_2, carbides, nitrides or ultra-refractory materials such as thorium oxide for very specific uses (nuclear applications).

- **Classification by the density**

There are dense refractories and light refractories. Lightweight refractories have thermal insulation properties and have an open porosity greater than 45%. Below this porosity value, refractory ceramics are considered « dense ».

1.4. Properties of ceramics regarding other materials

Ceramics have three important advantages over other competing materials: the raw materials used for their manufacture are relatively available and inexpensive, they are low-density compared to metals and they resist at very high temperatures, where most metals lose their strength. Furthermore, they have optical, electrical, chemical, magnetic, and thermal properties that make them irreplaceable in many industries, especially in the manufacture of electronic

and computer equipment. On the other hand, they present a very important defect, which is their great fragility (*Table 1.1*).

Table 1.1 : Comparative physical characteristics of ceramics, metals and polymers (orders of magnitude) [19]

Materials Features	Ceramics	Metals and alloys	Polymers
Melting temperature (°C)	1000-2500	600-1600	100-300
Density (in regard to water)	3-6	2-20	1
Vickers Hardness (GPa)	10-30	0.2 - 4	0.1 - 1
Young's modulus (GPa)	200-400	100-200	0.5 - 3
Shock resistance	Low	Very high	Very high
Machinability	Really low	Really high	Intermediate
Coefficient of thermal dilatation $(10^{-6}K^{-1})$	5 - 10	5 - 20	50 - 200
Electrical conductivity (S.m^{-1})	$10^{-13} - 10^{-18}$	$10^6 - 10^7$	$10^{-13} - 10^{-18}$
Thermal conductivity (W.m^{-1}.K^{-1})	10	200	0,3

In summary, compared to metals, ceramics are high-temperature resistant, thermal and electrical insulating, stiff and are hard materials. Compared to polymers, ceramics are much more resistant and their coefficient of thermal dilatation is lower, which can be useful for aerospace applications.

1.5. The case of alumina

This study focuses on alumina Al_2O_3 which is one of the best-known technical ceramics and is part of the refractory family. Alumina, also known as "aluminium oxide", is the second most abundant metal oxide in the earth's crust after silica. It comes in the form of a very stable white powder and can be found in different forms, where each has a unique crystal structure and properties [21] :

- The form α, which is the stable form and has a compact hexagonal structure

- Metastable phases, including the cubic γ and η phases, the monoclinic θ phase, the hexagonal χ phase, the orthorhombic κ phase and the δ phase that can be tetragonal or orthorhombic.

Alumina is found naturally in bauxite where it is hydrated and mixed with iron oxide. It is extracted by subjecting the rock to high temperatures and pressures and bringing it into contact with soda ash. A process, invented by the chemist Bayer and which still bears his name today, has been industrially exploited since the end of the 19th century (*Figure 1.2*).
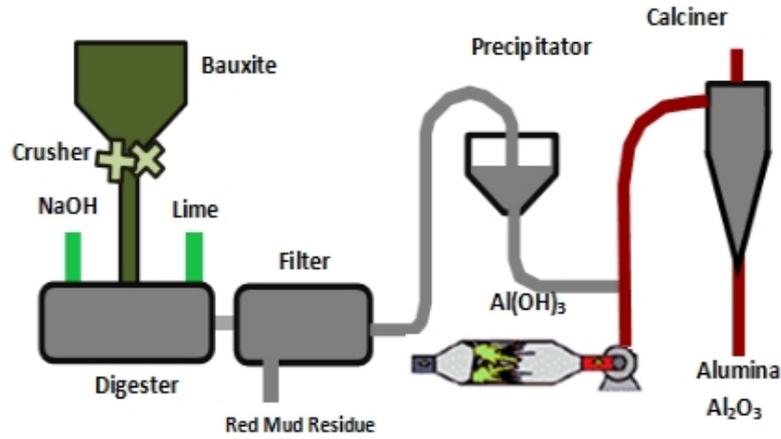
Figure 1.2 : Bayer process [22]

The Bayer process is the main industrial means of refining bauxite to produce alumina. In this process, bauxite ore (containing 30-55% of Al_2O_3) is washed with a sodium hydroxide solution at 175°C. The suspension is then filtered, sent to a high temperature calcination furnace (1000°C) and transformed into a fine, white powder called "alumina". A large amount of the aluminium oxide thus produced is then melted in the electrolytic process to produce aluminium [23]. However, alumina is also used to produce parts. High purity alumina (up to 99,99% purity) can be used in diverse engineering applications (*Figure 1.3*) in various fields, such as aerospace, automotive, biomedical and electronics [24].

Figure 1.3 : Diversity of components in alumina

1.5.1. Properties of alumina parts made by conventional manufacturing

In this study, only α-alumina is considered and its properties depend of the grade of purity. The density of alumina varies from 3 to 3.98 g/cm^3. High purity alumina has high mechanical properties (*Table 1.2* and *Table 1.3*) but offers also wear resistance, corrosion resistance, capability to withstand high temperatures and thermal stresses, high electric insulation and improved dielectric properties. High purity alumina ceramics with controlled composition and particle size can offer desired properties at low costs as needed for many engineering applications [24].

1.5.1.1. Elasticity

The usual ranges of elastic properties of engineering alumina at room temperature are summarized in *Table 1.2*. The grades A1 to A5 are high-alumina grades with at least 99% of alumina and the grades A6 and below are less pure grades, containing from 80% to 99% of alumina.

Table 1.2 : Typical values of elastic properties at room temperature for engineering alumina ceramics according to porosity levels [2]

Grade	Al_2O_3	Porosity%	Young's modulus (GPa)	Shear modulus (GPa)	Poisson's ratio
A1	≥ 99.6	0 - 2	380 - 410	158 - 164	0.24 - 0.27
A2	≥ 99.8	<1	380 - 405	161 - 164	0.22 - 0.25
A3	≥ 99.5	<1	398 - 400	161 - 163	0.23 - 0.26
A4	≥ 99.6	3 - 6	340 - 380	140 - 150	0.24 - 0.26
A5	≥ 99.0	1 - 5	340 - 380	130 - 145	0.24 - 0.26
A6	96.5 – 99.0	1 - 5	340 - 375	120 - 140	0.24 - 0.25
A7	94.5 - 96.5	1 - 5	300 - 370	110 - 140	0.23 - 0.25
A8	86.0 - 94.5	2 - 5	260 - 330	100 - 130	0.22 - 0.25
A9	80.0 - 86.0	3 - 6	260 - 330	100 - 130	0.22 - 0.25

According to *Table 1.2*:

- Young's modulus seems to increase with the increase of alumina purity and with the decrease of porosity. Young's modulus traduces the stiffness of the material which is defined as the ratio of stress (force per unit area) to strain (proportional deformation) in the linear elasticity regime of a uniaxial deformation.

- Shear modulus, which is defined as the ratio of shear stress to the shear strain, seems to have the same evolution as Young's modulus.

- Poisson's ratio, that describes the expansion or contraction of a material in directions perpendicular to the direction of loading, does not change noticeably according to purity or porosity.

1.5.1.2. Strength, toughness and hardness

Mechanical properties at room temperature are summarized in *Table 1.3*. According to this table, it seems that average strength and fracture toughness, which is the ability to resist to crack propagation, tend to increase when Al_2O_3 content is increasing. However, the strength of ceramic is a statically quantity with a relatively wide scatter. Indeed, ceramic materials have a so-called "brittle" fracture behaviour and break at a stress that can vary greatly from one specimen to another. This dispersion is due to the presence of defects in variable quantities,

distorting the classical hypothesis of homogeneity of mechanical behavior. That is why, a Weibull analysis is presented immediately after.

Table 1.3 : Mechanical properties of engineering alumina ceramics at ambient temperature. [2]

Grade	Avg. flexural strength (MPa)	Avg. compressive strength (MPa)	Weibull modulus	Fracture toughness (MPa√m)	Hardness (HV1.0)
A1	210-500	>4000	5-10	3.0-6.0	1500-2000
A2	150-450	>4000	6-12	3.5-6.0	1500-1900
A3	300-600	>3000	na	4.0-5.0	na
A4	150-450	>4000	na	4.5-4.9	na
A5	150-500	>4000	na	3.5-5.5	1300-1700
A6	150-450	>3000	na	3.0-5.0	1200-1600
A7	180-360	>3000	6-16	2.5-6.0	1200-1400
A8	150-350	>2500	5-15	3.0-4.1	900-1200
A9	200-300	>2000	na	2.5-3.5	800-1000

1.5.1.3. <u>Weibull analysis</u>

For materials considered as perfect, the theoretical breaking strengths are in the range of 0.1 to 0.5 times the value of the Young's modulus [25]. They are directly related to the breaking of atomic bonds. For example, high-density alumina has a theoretical fracture strength of 47 GPa. In practice, however, the actual fracture strength is much lower, around 400 MPa. Griffith [26] explains this difference in fracture strength by the presence of defects in the microstructure, which disrupt the perfect order of atomic stacking. The theoretical maximum stress is then reached by stress concentration in the vicinity of these defects.

According to Griffith's theory [26], for a given volume, the larger the sample, the greater the risk of sample breakage. Therefore, a small part will have a lower probability of containing defects that could initiate rupture than a larger part. The largest defect is not always the most critical defect, depending on the orientation of the defect and the direction of stress. Indeed, the most critical defect is the one oriented perpendicular to the direction of stress, which differs according to the loads (uniaxial, biaxial, etc.).

The characteristics of the defects (types, sizes, orientation) then become random variables, almost impossible to quantify. The stress at rupture of a material under a given load becomes a statistical variable and the rupture has a random character. The rupture is thus associated with a probability of occurring under the given conditions.

By applying the Weibull model to a three-dimensional structure under uniaxial tensile loading, the total probability of failure is described by [25] :

$$P(\sigma,V) = 1 - \exp\left(-\frac{V}{V_0}\left(\frac{\sigma - \sigma_u}{\sigma_0}\right)^m\right) \qquad (1.1)$$

With:

- P, the probability of total failure of the structure for stress σ and the volume V of the specimen

- m, the dimensionless Weibull modulus, which accounts for the dispersion of the values of stress at break

- σ_u, the threshold stress below which no rupture is possible.

- σ_0, the shape parameter that makes no real physical sense. In the case of a study on brittle materials, it allows the graphic representation of the Weibull model to be positioned in relation to the stress axis.

- V_0, reference volume, which is unitary - $1m^3$ for example - allowing to adjust the dimension of the form factor.

The Weibull modulus reflects the probabilistic nature of the material's fracture behavior. The higher the modulus, the lower the dispersion and ceramics have a Weibull modulus between 1 and 20, composites around 30 and the most brittle metals have a modulus greater than 50. P. Auerkari gives in *Table 1.3* example of Weibull modulus for alumina according to purity grade.

In most cases, the threshold constraint σ_u is set to zero. Thus, even for low values of applied stress, there will be a very low probability of failure (but not zero). This assumption makes it easier to determine the Weibull modulus and the shape parameter. In addition, [27] has shown that for test campaigns with a limited number of specimens, a two-parameter Weibull model is more suitable than a three-parameter model.

To determine the Weibull parameters, the simplest method is the linear regression method. Simply take twice the logarithm of the Weibull formula (equation (1.2)) and plot the stress at break as a function of its probability of failure [25]:

$$\text{Ln (ln (1-P))} = m \, (\ln (\sigma) - \ln (\sigma_0)) \tag{1.2}$$

The Weibull modulus corresponds graphically to the slope of the line drawn from the experimental data and the shape parameter is deduced from the intercept at the origin in *Figure 1.4*.
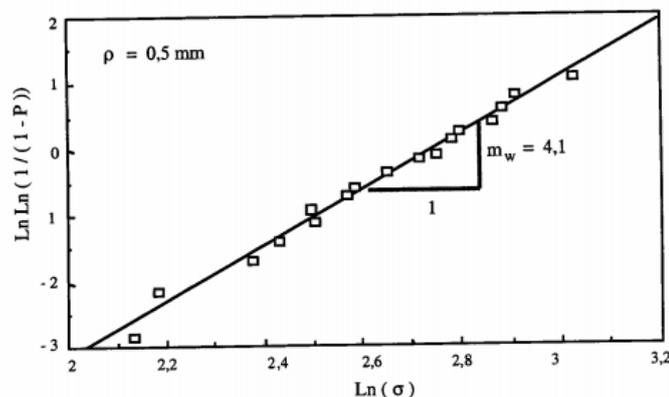
Figure 1.4 : Estimation of WEIBULL parameters [28]

- **Influence of the number of specimens on the determination of the Weibull parameters**

The choice of a suitable determination method is essential for obtaining a correct estimation of the Weibull parameters. Nevertheless, many authors have shown that the number of specimens influences the precision in the determination of Weibull parameters. A study [27] has shown that from 60 experimental values, the error of estimation of the Weibull modulus is less than 2.5% and is about 5% for 30 values. They state that below 20 experimental values, the parameters determined are unreliable.

1.5.2. Properties of alumina parts used in stereolithography

In this report, the process studied is stereolithography, of which principle is explained later. The nominal properties of the sintered alumina are given in *Table 1.4,* by taking as example the material provided by the company 3D Ceram. This company is cited in many articles and is a reference in additive manufacturing for ceramics.

Table 1.4 : The nominal properties of the sintered alumina used for SLA manufacturing [3D Ceram (Limoges, France-http://3dceram.com)].

Material property	Sintered alumina
Density (g/cm^3)	3.9
Vickers Hardness (HV)	16.4
Young's Modulus (GPa)	360.8
Poisson's ratio	0.242
Thermal Conductivity (W/m$^\circ$C)	26.1

2. Manufacturing for alumina parts

The steps to produce ceramic parts are outlined in the following figure:
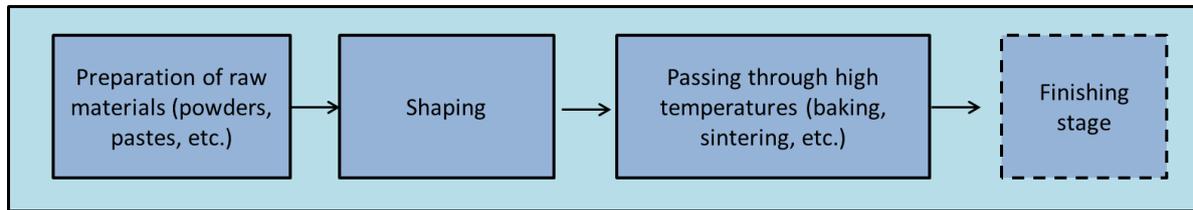
Figure 2.1 : Steps in the elaboration of a ceramic piece

The elaboration of the raw materials is an essential stage which determines the composition of the future piece and conditions the following stages, i.e. the choice of the shaping process and the baking conditions. Finishing is shown in *Figure 2.1* in a dotted frame, which means that this step is not always essential, and there are many ceramic pieces that do not require this step.

There are many techniques for shaping, which can be conventional manufacturing or, most recently, additive manufacturing (*Figure 2*.2).
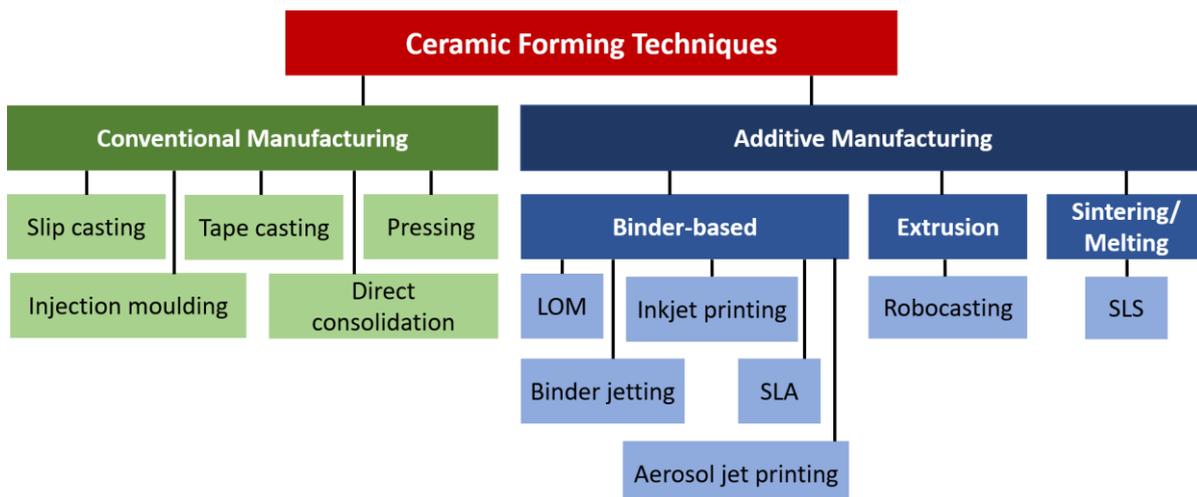
Figure 2.2 : Shaping for ceramics

The shaping processes are often the same for traditional ceramics (red, white or art ceramics) and for technical ceramics. *Table 2.1*, which lists these different techniques according to the amount of liquid used to prepare the raw material, indicates those that are rather specific to traditional ceramics and technical ceramics. The proportions of the liquid phase can vary greatly depending on the contents of other possible additives (binders and plasticisers), which themselves have a major influence on the viscosity of pastes and slurries. The table also provides information on the rates of production associated with these techniques, which vary considerably from one to another.

Table 2.1 : Summary for the different shaping technics for ceramics [19]

Proportion of liquid in raw materials	Name of the process	Traditional ceramics	Technical ceramics	Production rate
Liquid suspensions (30 – 50 %)	Slip casting/ injection	Yes	Yes	Slow (Few parts/hour)
Soft pastes (20 – 30 %)	Turning/ calibration	Yes	No	Slow (Few parts/hour)
	Moulding	Yes	Rare	Fast (hundreds of parts/hour)
	Extrusion	Yes	Yes	Fast (hundreds of parts/hour)
Dry pastes, powders and pellets (0 – 2 %)	Injection	No	Yes	Fast (hundreds of parts/hour)
	Pressing	Yes	Yes	Fast (hundreds of parts/hour)
Powders (0 %)	Hot pressing	No	Rare	Very slow (less than 1 part/hour)
Powders or pastes (0 – 50 %)	Additive manufacturing	No	Yes	Very slow (less than 1 part/hour)

Alumina being a technical ceramic, only the techniques allowing its shaping will be briefly described.

2.1. Slip casting

Traditionally used for table ceramics or sanitary ware, slip casting is the only technique, apart from new additive technologies, that can be used to obtain parts with complex geometry (tureens, cups, sinks, etc.). This method has evolved considerably over the last thirty years or so with its implementation in the field of technical ceramics and the introduction of two innovative processes: pressure injection and tape casting.

The principle of this method (*Figure 2.3*) is based on the manufacture of a mould made of porous material (plaster) into which the slip is emptied. The plaster partially absorbs the water from the slip by capillary action, so that the small suspended particles are deposited on the edges of the mould. After a certain time (often more than 1 hour) the mould is emptied, and the piece is removed from the mould. This last step is delicate, since the piece must not be broken or deformed [19].
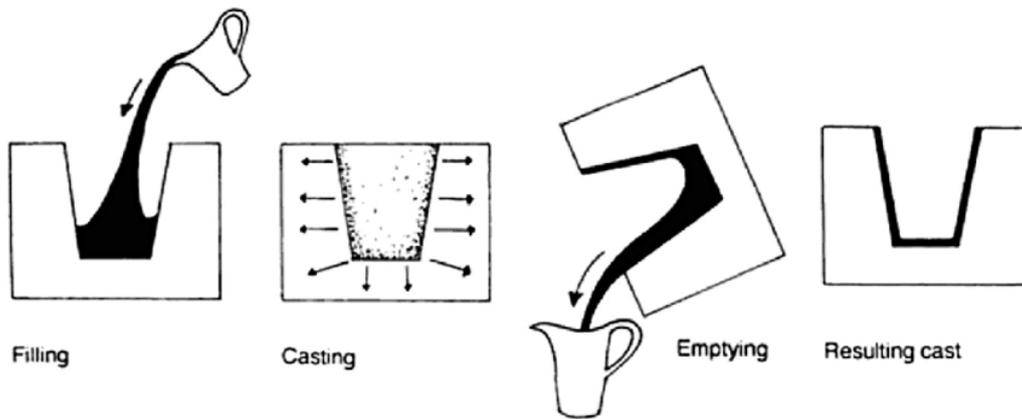
Figure 2.3 : Slip casting [29]

Plaster moulds tend to be replaced by moulds made of porous plastic material, the water being forced out of the moulds by applying a pressure of several tens of bars.

2.2. Extrusion

The extrusion technique (*Figure 2.4*) consists of placing the soft ceramic paste in an extruder from which the paste comes out in the form of "strands" of circular, rectangular, alveolar or other, which can be cut to the desired length, for example by a wire. This method requires the use of pastes with relatively low moisture content but with a high proportion of binders and plasticizers (up to more than 50 %). Pressures are obtained by means of cylinder devices up to several hundred bar or, more often, by means of screw systems.
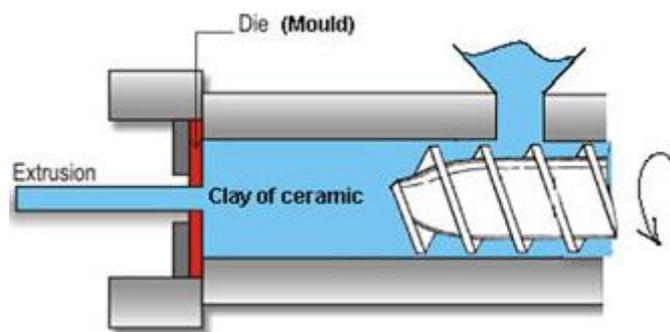
Figure 2.4 : Extrusion process [30]

Traditional ceramics such as hollow bricks or certain tiles are produced in this way, but also technical ceramics such as electronic devices, supports for alveolar catalysts, etc. [19]

2.3. Injection

The shaping of technical ceramics (alumina, zirconia, tungsten carbide...) is frequently done by injecting dry powders using the CIM (Ceramic Injection Molding) process when preparing parts with complex geometries. The principle is very close to those of extrusion, as the moulds that give the shapes are fed with pastes (sometimes heated) by screw type injectors similar to those of extrusion presses. As with extrusion, the pastes usually contain little or no moisture, but

contain always very high quantities of binders and plasticizers (up to 50% to 60%) which must then be removed before cooking (debinding) [19] .

2.4. Pressing of dry pastes, powders and pellets

This technique revolutionised the plate production in the 1980s, thanks to so-called "isostatic pressing" machines. The ceramic raw material has practically no moisture, but only binders and plasticizers in small quantities and is usually in powder form. The powder is injected into a mould, of which at least one part is flexible. Often, only the flexible and movable part of the mould is made of polymer, while the counter-mould is made of a metal alloy.

The powder feed is rather vertical, and once the mould is filled, it is closed tightly. The polymer part is then deformed by a high pressure of several tens or hundreds of bars, transmitted by a liquid, usually oil (*Figure 2.5*). This pressure, evenly distributed over the entire surface of the polymer, is transmitted to powder (hence the adjective "isostatic"). The grains of the ceramic stick together thanks to the pressure, thus creating a relatively solid raw part. The whole process can be automated to produce thousands parts per hour [19].
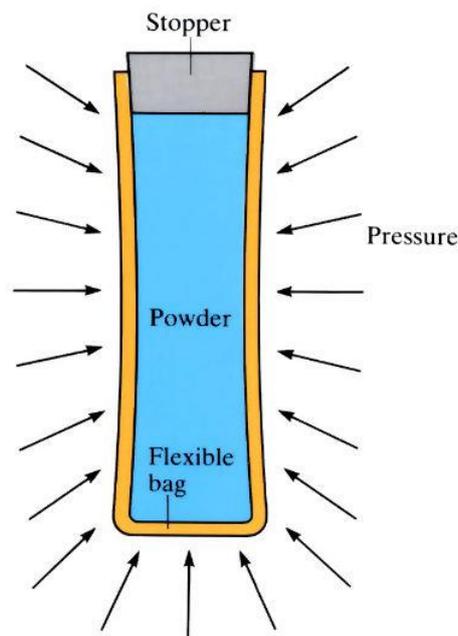

Figure 2.5 : Cold isostatic pressing [31]

3. Additive manufacturing

Additive manufacturing involves a whole series of new technologies that consist of stacking successive layers of ceramic materials. These processes, initially applied to polymers, appeared in the 1980s due to new industrial competitiveness issues. Indeed, additive manufacturing meets the need expressed by industrialists to reduce product development time and consequently, market access time. At the beginning, these techniques were called "rapid prototyping" [4]. "Prototyping" because there were used to produce prototypes and "rapid" because there was no need of creating and producing a mould, and consequently the production of the prototype is faster. These technologies are increasingly used because they allow the production of complex shapes that would otherwise be impossible to obtain.

From the design (computer-aided design, CAD) to the piling of the devices responsible for stacking the successive layers, the pieces can only be built using powerful computer means.

3.1. Digital chain associated with the additive manufacture of ceramic parts

First, a 3D model of the object to be produced is created digitally using CAD (Computer Aided Design) software or by digitally acquiring a 3D object already existing. The model is then exported in STL (Standard Triangulation Language) format, that transforms the geometric model into a mesh, defining the surface of the part by a set of oriented triangles. Finally, the digital object is cut by a software dedicated to additive manufacturing into a multitude of cross-sections, called "slices", with a thickness ranging from 25 to 100 μm. The resulting file is sent to the 3D printing machine (*Figure 3.1*).
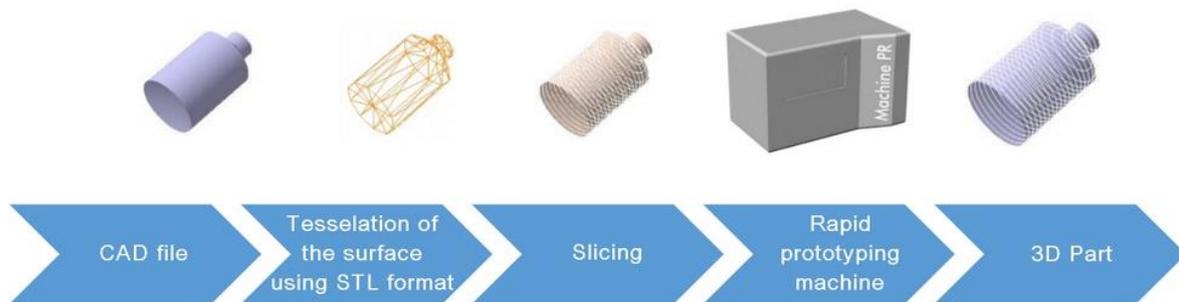
Figure 3.1 : AM process [32]

3.1.1. CAD file

Any part intended to be manufactured in AM must have a digital model that perfectly describes its geometry. This digital model can be obtained in different ways, by using a CAD software or using "reverse engineering" with a 3D object already existing.

- **Direct CAD**

Product development requires attention to the design process, from a preconceived idea to a detailed product description and then to its manufacture. After the conceptualization phase, which can take several forms (sketch, drawing, mock-up or model), it is necessary to produce

a description of the product in a digital form called a "digital mock-up". The 3D CAD software used to create these digital models is based on surface modelling or solid modelling.

In surface modelling, the object is defined by its envelope, its boundary surfaces. The description of the surfaces is carried out using parametric polynomial equations. Emphasis is placed on style/form considerations rather than technological considerations. These are models mainly intended for the aeronautics, automotive or industrial design industries.

Solid modelling is more widespread than surface modelling. It integrates the notion of matter and uses primitives (generally 2D sketches), allowing the creation of volumes thanks to various operations (extrusion, revolution...). These volumes combined together lead to the final solid; or a succession of Boolean operations (union, intersection, subtraction) performed on generic solids (sphere, cylinder, parallelepiped) [33].

- **Reverse engineering**

Geometric modelling also involves knowing how to reconstruct objects from the digitalization of existing objects when the digital model is unavailable or non-existent. This is known as "reverse engineering" or "reverse design". This technique is used in a wide variety of fields such as art (for instance, for the reproduction of statues) or the medical field (for instance, to produce custom-made prostheses).

Reverse engineering (*Figure 3.2*) is based on the acquisition of a cloud of points representing the envelope surfaces of the scanned element. These sets of points are then processed using surface reconstruction software to define the skin of the object using mathematical entities and it is then exported to CAD software. The 3D model is finally modified and adapted to its environment and internal architecture.

1. Part to digitise   2. Point cloud   3. Creation of geometric entities   4. 3D model

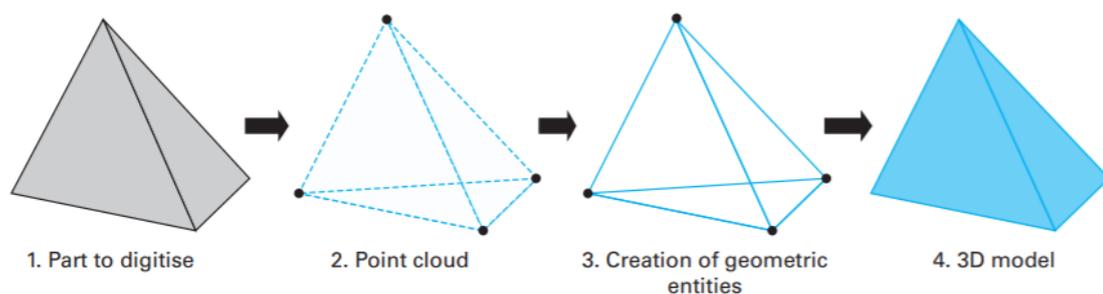*Figure 3.2 : Reverse engineering process [33]*

At the end of the CAD or reverse engineering work, the created file will have to be converted and checked in order to be usable for manufacturing.

3.1.2. STL format

The STL file is the standard for transferring CAD data to the AM machines. It is independent of the CAD software used and it serves as a very simple descriptor of part geometries by

approximating the envelope surfaces using a set of triangles (or facets) and their normals. These elements are obtained by a facetization operation called "tessellation" [33].

The creation of STL file requires optimal surface modelling. Surfaces must be perfectly closed and oriented. If these two conditions are not met, the STL file will be of poor quality, or even unusable later by the machine. To overcome this problem, a file control step with adapted software is necessary.

Frequently detected errors requiring file corrections are as follows (*Figure 3.3*) [33]:

(a) **Under-facetization.** It is generally due to a mesh parameter that is too large (use of the CAD software's default parameter or choice of the wrong parameter). The result is an approximation of the initial large area characterized by the chord error "d" (*Figure 3.3 (a)*) representing the maximum distance between the facet and the surface element it represents. This error can be minimized by increasing the number of facets. However, a finer triangulation can also be annoying because the generated STL files will require a lot of computing time.

(b) **Lack of facets**. It is a hole in the mesh.

(c) **Normal inversion**. The direction of the normal to the triangle makes it possible to know the position of the material, when this one is reversed, there is thus confusion on the direction of the material.

(d) Presence of **non-manifold elements**. These are crushed or superimposed triangles.
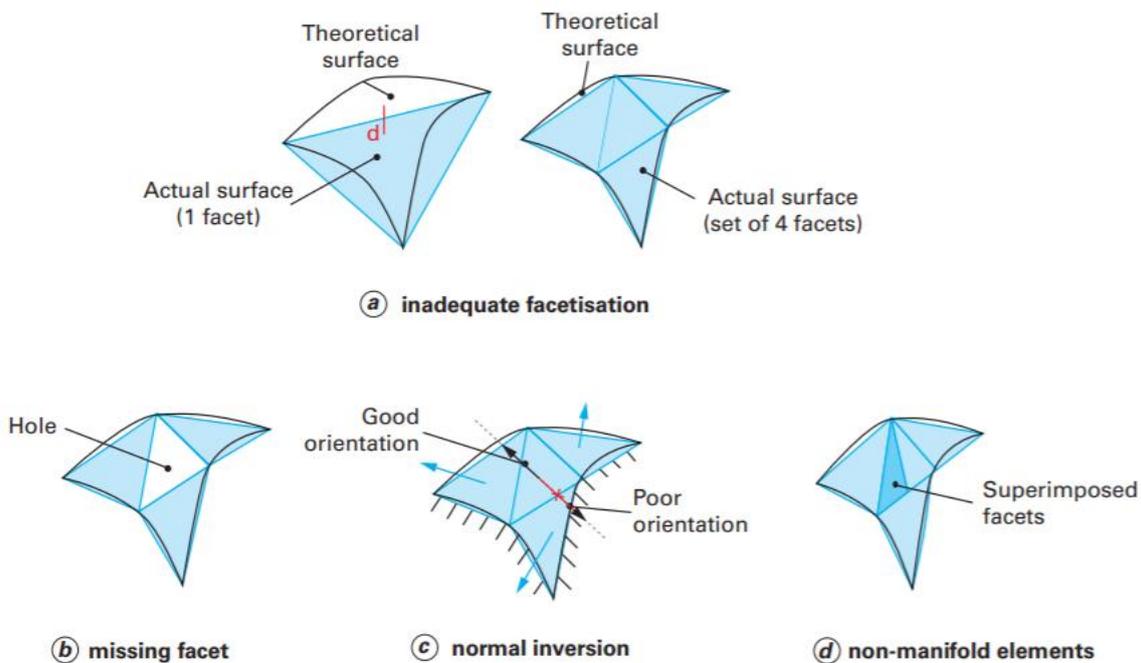

Figure 3.3 : Common STL mistakes (19)

Despite the large number of errors, the STL format remains the most reliable format. In addition, there is software available to help correct these possible errors [4].

3.1.3. Orientation and support generation

Because 3D printing creates parts layer by layer, finished parts may have variations in resistance depending on the orientation of the parts during printing, with different properties in the X, Y and Z axes. Choosing the orientation of the part in relation to the work platform is then a crucial step. The orientation will not only determine the resistance but it will also define the final quality of the part, the distribution of heat, the necessary supports, etc. For example, in metal fabrication, it is not possible to print a large flat area without supports because the heat will not evacuate well and will cause deformation of the part [4].

Hollow parts require internal support structures (*Figure 3.4*), not to cave in during the process because of shear stress generated during the spreading, as well as overhanging features [34]. Thus, the supports make it possible to anchor the construction part to the building plate, to protect the side parts against actions that could alter the construction and to support the undercut parts [4].

However, model orientation on the building platform has a strong influence on the building time because it directly controls the numbers of layers that will be necessary to obtain the part. The closer the higher point of the workpiece is to the build table, the lower the number of layers and therefore the shorter the production time. Moreover, the generation of support increases costs and results in a poor surface finishing wherever they are in contact with the part. Thus, an optimization of these structures is needed to decrease build time and cost and to improve surface quality [34].

Figure 3.4 : SLA part with supports (polymer)

After building the part, it is important to remove all the support structures during post processing. Sometimes, due to the complexity of the part, it is not possible to access and remove all the supports structures, unless the material of the support is soluble. Therefore, it is necessary to take into account the accessibility of support structures while designing them.

3.1.4. Slicing

The final step before sending the file to the printing machine is the slicing.

Stereolithography, as well as other processes (SLS, etc.) requires a spreading step. A fine layer of primary material (liquid polymer for SLA) is spread by a scraper and the thickness spread has to be determined numerically, by generating layers in the numerical model called "slices".

The stratification operation of the model is always carried out automatically by a software which also calculates the material deposition paths. As the initial model is in STL format, the slicing tool simply calculates a set of intersections between the flat facets of the model and the different layering planes. These calculations, numerous but relatively simple, are generally done without problem, unless the template in STL format is not correct *(Figure 3.3)*. Most of the time, the operator chose the slicing height (layer thickness), which can be constant or adaptative. The height directly influences the number of layers and therefore the manufacturing time but also the dimensional accuracy of the part (*Figure 3.5*).
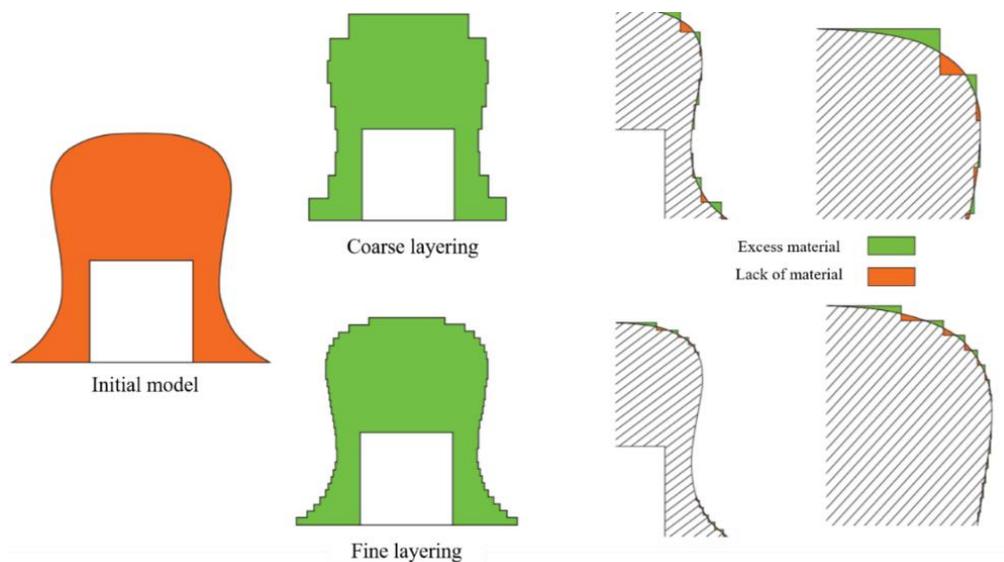
Figure 3.5 : Illustration of how a part is obtained by stacking layers [6]

3.1.5. Drop-off paths

The calculation of the material deposition paths is conducted by software in a semi-automatic way, respecting the operator's requests. Indeed, it is generally up to the operator to specify the filling strategy he wants to adopt to satisfy the desired use (design or functional) [6]. To do so, it is necessary to know the impact of the main adjustment parameters proposed.

The most frequently used paths are the so-called "parallel contour" paths, which result from the calculation of curves parallel to the initial contour of a shape and the "zig-zag" paths that result from the calculation of lines parallel to a given direction within a predefined contour. Usually, it is a mix of the two paths that is used for a layer. The contour of the layer is most of the time done with one or more curves parallel to the outer contour (in blue in the *Figure 3.6*) to have a correct surface state and the rest of the layer is done with zig-zag paths (in orange in the *Figure 3.6*).

Thus, the operator must define *(Figure 3.6)* [6]:

- the number of passes parallel to the outer contour of the layer;
- the distance between these passes;
- the distance of these passes from the outer contour of the layer;
- the direction of the inner "zig-zag" passes;
- the distance between these passes;
- the distance between the inner "parallel contour" passes and the inner "zig-zag" passes;
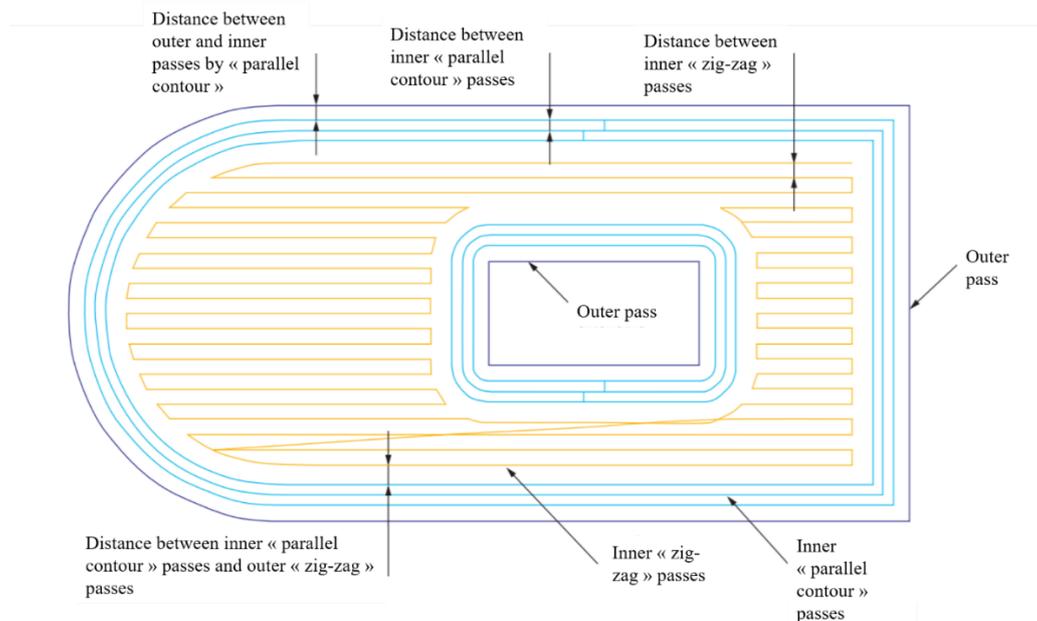
Figure 3.6 : Example of filling paths [6]

All these parameters strongly condition the surface finishing and the resolution of the finished part, as well as its mechanical characteristics (density, Young's modulus, etc.). Indeed, they directly influence the stacking state of the material on the surface (visual and geometric aspect) and inside the part (macroscopic mechanical behaviour). In addition, the final density of the baked part is strongly related to the rate of compaction of the green part [6]. As information, a green part is the part before sintering or firing, whose main constituents are weakly bounded.

Once the operation of calculating the different material deposit/consolidation paths has been completed, it remains to write them in a file with a format that can be understood by the digital control director who controls the machine. The resultant file is finally sent to the printing device.

3.2. Classification and presentation of AM technologies

AM techniques for all materials (polymers, metals and ceramics) can be classified as follows:
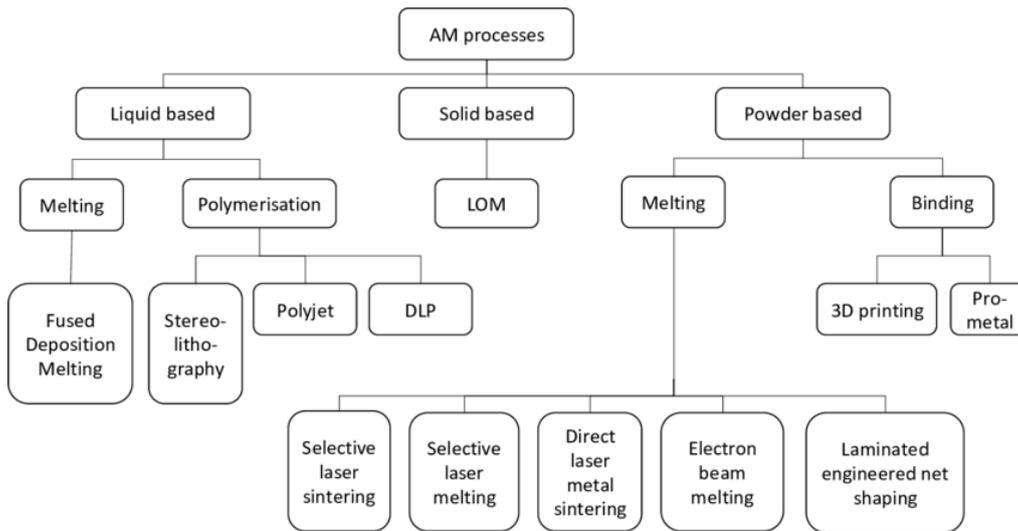
Figure 3.7 : AM classification [35]

The primary material can be liquid, solid or in powders. However, not every technique can be used to manufacture ceramic parts.

The methods that can be used for ceramics are described in the following figure [6] :
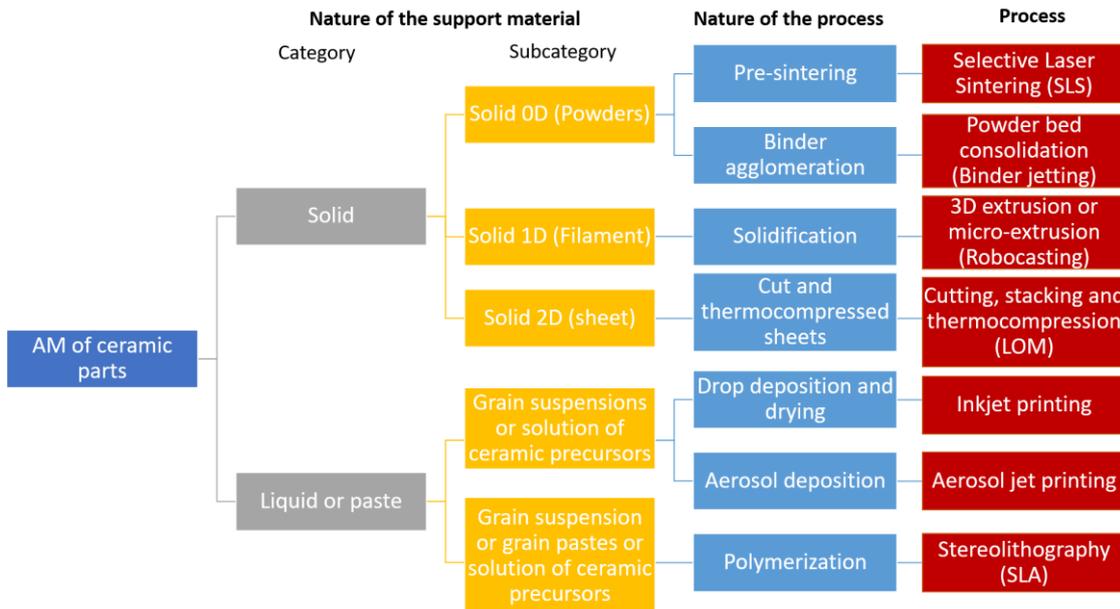
Figure 3.8 : Classification of AM techniques for ceramics

3.2.1. Selective laser sintering (SLS)

The laser sintering method consists of selectively (pre)sintering particles from a previously laid down powder bed on a manufacturing tray (*Figure 3.9*). The energy comes from an infrared laser beam which scans the shape of the section to be produced, for each layer.

Historically, parts made by this process were made of plastic, involving melting of the material, not sintering. Thermoplastic materials are naturally predestined for this process because they

have a low melting temperature. It is therefore more delicate to use materials with high melting points such as high melting point ceramics. Indeed, their densification takes place in the solid state via atomic species transport mechanisms (sintering) and high temperatures are necessary to obtain acceptable densities. Moreover, thermal stresses induced during the sintering process by temperature rises and subsequent cooling, often lead to the formation of cracks in the sintered parts.

Despite these limitations, the process of selective powder sintering for obtaining ceramic parts is developed through two distinct approaches, linked to the sintering ability of the materials used: direct sintering or consolidation by fusion of a secondary phase. In the first case, the laser source directly heats the powder to sinter the particles together to obtain a cohesive part, while in the second case a low melting point organic is added to the powder to bind the particles together. The parts obtained in the second case can be subjected to heat post-treatment [6].
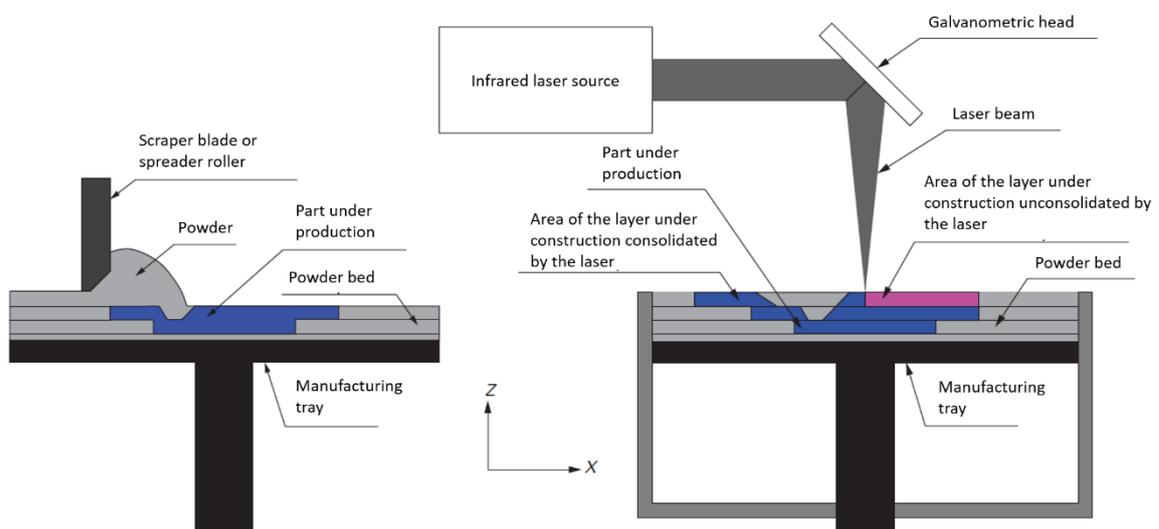
Figure 3.9 : SLS process [6]

3.2.2. Binder jetting

This technology (*Figure 3.1*) is similar to inkjet printing but the construction of each layer begins with the spreading of a powder bed on the manufacturing tray. A printhead that can move in X and Y distributes drops of binder at the points where the part is to be formed in the final layer. The binder so deposited will bridge the powder particles together. Once all the layers necessary for the production of a finished part have been completed, the part is extracted from the powder bed and cleaned to remove all non-agglomerating powder particles. The part then undergoes heat treatments of less than 600°C to remove the binder and then is sintered [6].
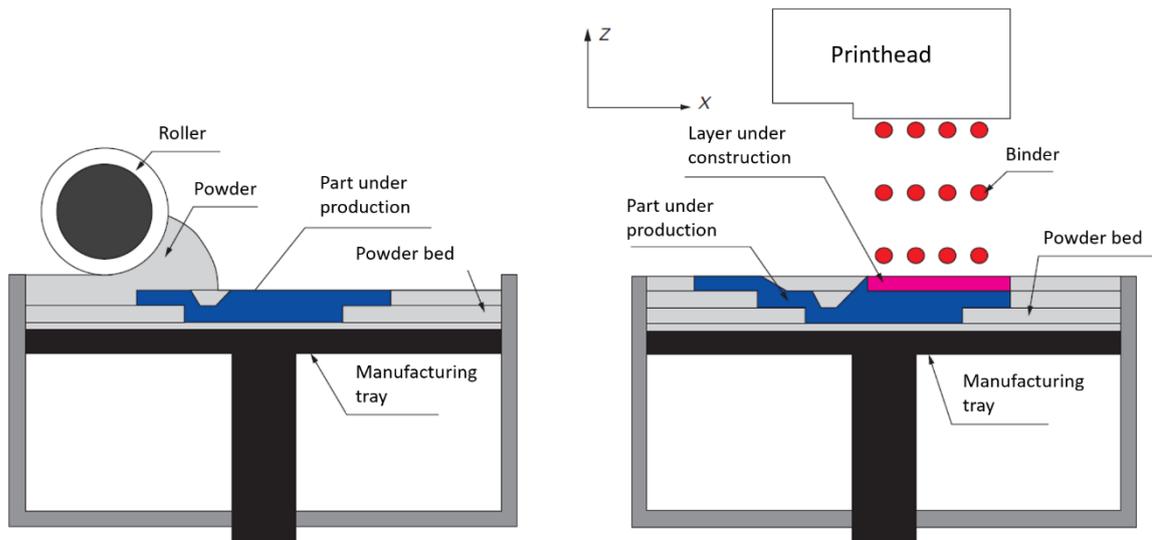
Figure 3.10 : Binder jetting process [6]

3.2.3. Robocasting

This technology is based on extrusion. It finds multiple names depending on the extruded material and the extrusion conditions. The most common names are "Fused Deposition Modelling" (FDM), which involves a fusible phase (e.g. paraffins) which consolidates on cooling and "Robocasting" which is based on the extrusion of a paste or suspension. The ceramic paste pass through an extrusion nozzle and comes out with a form of a strand. The nozzle is positioned in relation to a manufacturing plate to create, layer by layer, a piece by depositing the strands (*Figure 3.11*). Then debinding and sintering are required. [6]
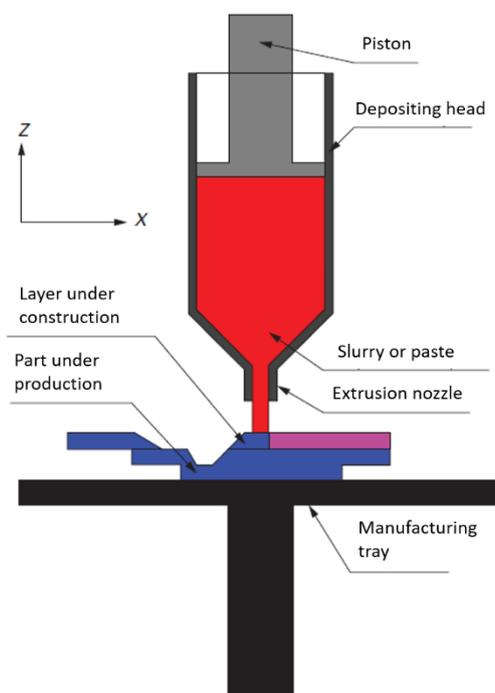
Figure 3.11 : Robocasting process [6]

3.2.4. Laminated Object Manufacturing (LOM)

For LOM process, green strips produced by tape casting or extrusion are used. The shape of each layer is cut in these strips thanks to the energy of a laser and then are stacked. Thanks to thermocompression, the strips adhere together. This process allows therefore to produce 3D objects from 2D ceramic components (*Figure 3.12*) [6]. Then debinding and sintering are required.
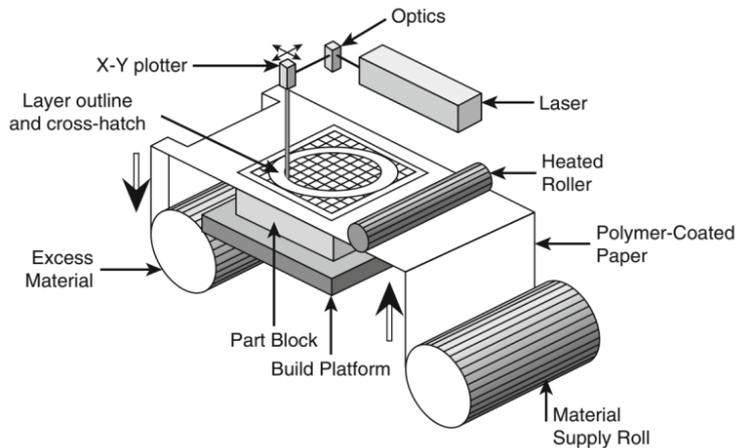
Figure 3.12 : LOM process [36]

3.2.5. Inkjet printing

The inkjet printing process is based on the 2D printing techniques that place, on a substrate, ink drops that penetrate the substrate by capillarity. For additive manufacturing, the production of each layer of the part is achieved in a similar way but contrary to 2D printing, ink is a suspension containing solid and does not penetrate the substrate. First, an ink is loaded with few volume percent of ceramic particles or a solution of precursors of the desired material. Then, this ink is sprayed drop by drop at precise points through calibrated nozzles located in print head(s). The print head(s) are positioned in the XY plane and the Z-axis carries the manufacturing platen (*Figure 3.13*) [6]. Then debinding and sintering are required.
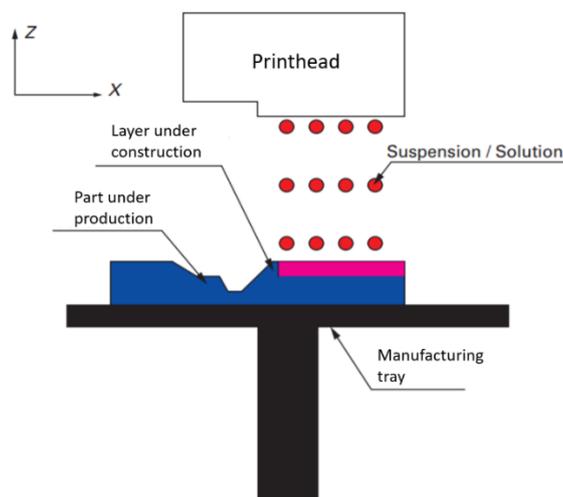
Figure 3.13 : Inkjet printing process [6]

3.2.6. Aerosol jet printing

This technique uses an ink loaded with ceramic particles. The aerosol generated in the spray head is transported to a virtual impactor where it is densified. It is then aerodynamically focused by a gas injected inside a nozzle to impact a substrate at very high speed (*Figure 3.14*) [6]. Then debinding and sintering are required.
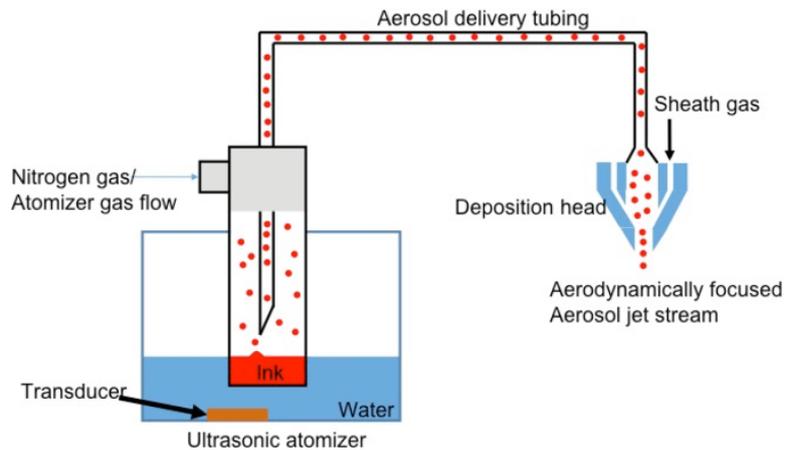
Figure 3.14 : Aerosol printing process [37]

3.2.7. Stereolithography (SLA)

Stereolithography (SLA) is based on the spreading and then curing of a photosensitive resin by polymerization, which is activated by a source of light energy (most often a UV laser). This process was extended to the field of ceramics in the mid-1990s with the development of photosensitive ceramic slurries/pastes.

A layer of ceramic paste sensitive to UV is first spread on a manufacturing tray. Then, a UV laser source comes to polymerize the areas of the layer that need to be hard to form the future part (*Figure 3.15 (b)*). and this process is repeated until the construction, layer by layer, of the complete part. The detailed process is described in part 5.
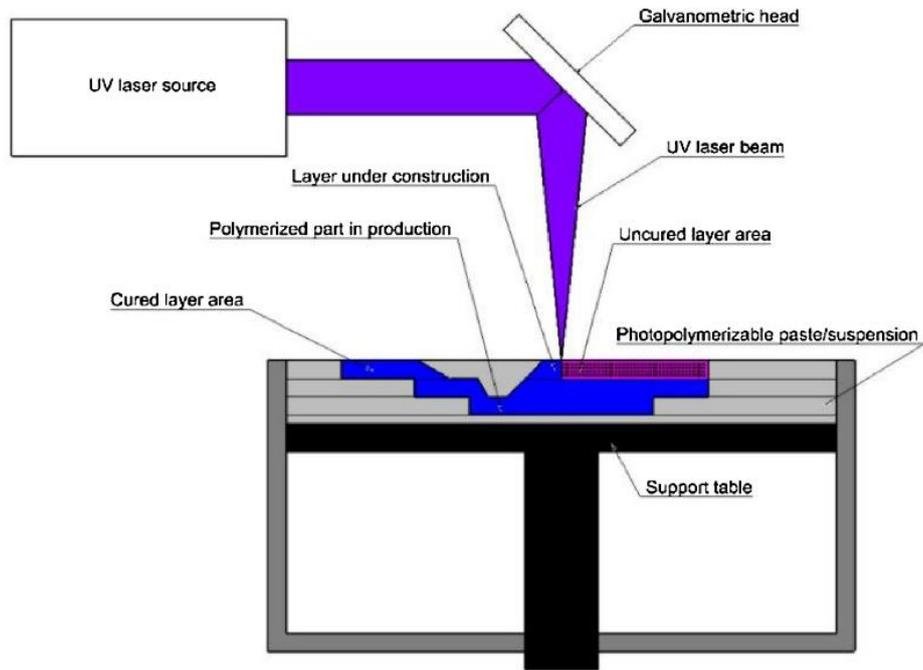
Figure 3.15 : SLA process [6]

3.2.8. Comparison between processes

Benefits and drawbacks of all processes described above are listed in *Table 3.1* [6]. According to this table, SLA is an interesting process, having more benefits than drawbacks. This process combines good mechanical properties, good surface finishing and high resolution, making it a highly competitive process to produce complex parts or prototypes. It is only limited by the use of costly photopolymer which can also be toxic for humans and wildlife. By consequence, this kind of implementation will need to follow strict regulations.

Unlike conventional techniques (pressing, tape casting, etc.), stereolithography allows the production of complex parts. Moreover, it is possible to obtain a part in less than two days, at a reasonable cost because no additional molds and/or machining (material subtraction) are required. However, stereolithography (like most additive manufacturing techniques), may require the addition of supports to prevent sagging of the part, and these supports must be removed mechanically. In addition, dimensional stability is limited due to residual stresses. Finally, this technique presents the problem of "trapped volumes", i.e. uncured liquid material that remains trapped inside the part with no possibility of evacuation [4].

Table 3.1 : Benefits and drawbacks of AM techniques for ceramics [6]

AM process	Resolution	Benefits	Drawbacks
SLA	30 - 100 µm	• Complex architecture • High resolution • Good surface quality • Good mechanical properties • Quick implementation	• Use of organics • Photopolymer cost • Post-treatments necessary (cleaning, debinding and sintering)
Inkjet printing	50 µm	• High resolution • Good surface quality • Wide range of materials	• Use of organics • Thin layers (5 – 10 µm): difficulty to build high parts (above hundreds of microns) • Ink cost • Post-treatment necessary (sintering)
SLS	100 - 500 µm	• Complex architecture • Wide range of materials	• Resolution limited by the powder granulometry (10-100 µm) • Surface roughness • Low density • Weak mechanical properties
Binder jetting	50 – 100 µm	• Simple technology • Wide range of materials • Low cost	• Use of organics • Weak cohesion between layers • Surface roughness • Low density • Weak mechanical properties • Post-treatments necessary (cleaning, debinding and sintering)
Aerosol jet printing	10 – 50 µm	• Strong resolution	• Thin layers • Low deposition speed • Post-treatments necessary
Robocasting	400 – 1000 µm	• Wide range of materials • No loss of materials • Low cost • No cleaning needed after building • Good mechanical properties	• Use of organics • Low resolution (conditioned by the diameter of the nozzle) • Poor surface quality • Post-treatments necessary (debinding and sintering)
LOM	100 µm	• Rapid technology • Good surface quality • Low cost	• Use of organics • Fragility of the ceramic tapes • Minimal layer thickness (100 µm) • Weak cohesion between layers • Simple architectures • Post-treatments necessary (debinding and sintering)

4. Stereolithography

Stereolithography for polymer parts is the first additive manufacturing process to be introduced in 1984, with a first patent delivered by Charles Hull [5]. This process, which was first commercialized by the company 3D System (USA), largely dominated the additive manufacturing market during the 1990s. The development of this technique for ceramics started in the 2000s, especially in Limoges at IRCER with Thierry Chartier.

4.1. Process principle for polymeric materials

A reservoir is filled with a photosensitive resin, which contains one or more monomers/oligomers and a UV-sensitive photo-initiator. Then, a platform movable along Z axis is immersed into the tank at a depth corresponding to a slice. A digitally controlled UV laser beam scans the surface along the X and Y axes (*Figure 4.1*) and according to the pattern corresponding to a 2D layer of the digital model. Thanks to the laser energy, a polymerization reaction occurs and the scanned areas become hard. The platform is then lowered by an increment, defined as the thickness of a slice, and is coated with a new layer of liquid resin by means of a scraper. The process is then repeated until the part is completely manufactured.
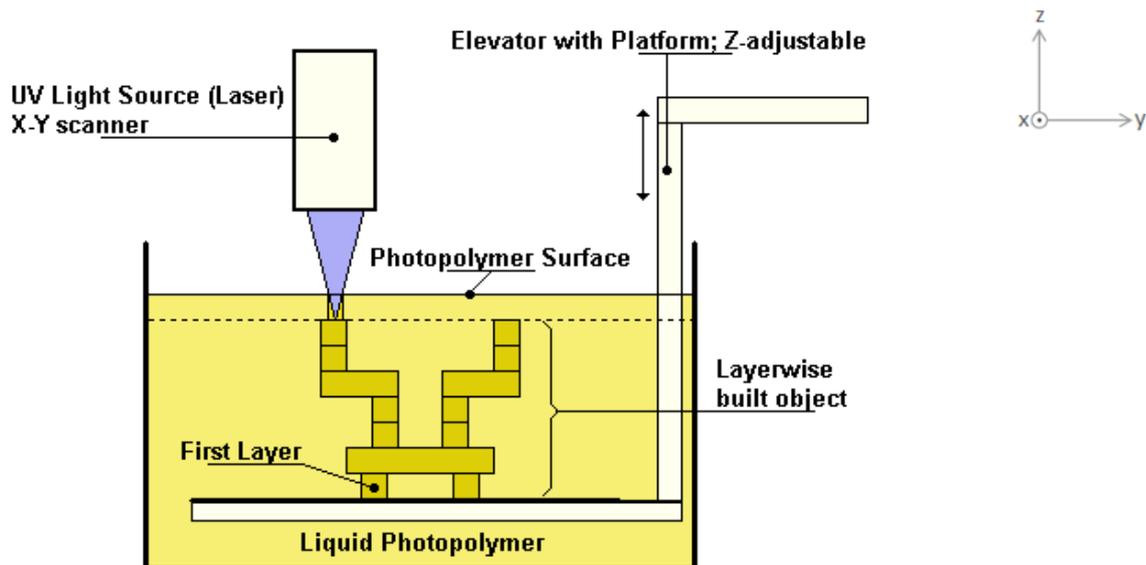
Figure 4.1 : Stereolithography process [38]

4.2. Stereolithography for ceramic materials

For shaping ceramics by SLA, the suspension must contain, in addition to the photosensitive resin, ceramic powder (50 to 65 wt%), as well as a dispersant, in order to increase the stability of the paste (avoiding sedimentation and powder agglomerates). During the manufacturing process, the photosensitive system hardens under the action of the UV laser beam radiation and the ceramic particles are "trapped" in a polymerized matrix.

Even if the design and manufacturing process is the same as for plastics, at the end of the process, the ceramic part obtained is a green part. A debinding and sintering steps must therefore be carried out to obtain a dense part.

The debinding step consists in removing the polymer network: this step is delicate because it can lead to cracks and/or deformations of the part. At the end of the debinding process, the part is only made up of a stack of ceramic particles with low cohesion. A sintering step is therefore necessary to consolidate the part and to densify it. Densification, which corresponds to an elimination of porosity, leads to a general decrease in the volume of the part, called "shrinkage" (see part 6 for details regarding debinding, sintering and shrinkage).

4.3. Photopolymer and photopolymerization

There is a wide choice of monomer/photoinitiator pairs that can solidify by exposure to electromagnetic radiation. However, those used in SLA are generally those sensitive to ultraviolet (UV) light [6].

4.3.1. Photopolymer

Photopolymers are liquid resins sensitive to ultraviolet radiation. The main characteristics that a photopolymer must have can be summarized as follows [4]:

-   Low activation energy;
-   Limited volatility and toxicity;
-   Stable viscosity;
-   Low shrinkage;
-   Low sensitivity to moisture.

Moreover, the rheology (viscosity and behavior) has to be adapted to the deposition of low thickness (i.e 10 µm). Suspensions should have a high percentage of ceramics grains, typically above 50% in volume in order to maintain the cohesion of the part during and after debinding. Despite of the high concentration of ceramics, the suspension must have a high polymerization rate of the reactive suspension, called "reactivity" [6].

In numerous scientific articles, formulation of the suspension is confidential. However, some researchers make their formulation public. It is the case for instance of Li et. al [16]. Their suspension is composed of :

-   48vol% of alumina powder (SAO-030A, SINOCERA, China);

-   A monomer composed of 1,6-hexanediol diacrylate and ethoxylated pentaerythritol tetraacrylate;

-   A Photoinititior which commercial name is Irgacure 184;

-   An alkylamine dispersant ;

-   Polyethylene glycol-400 as plasticizer.

Another example is given by Wu et. al [13], where their premixed solution used to prepare the ceramic suspension consisted of four components:

- 23,75 wt% of acrylamide;

- 1,25 wt% of N, N′ methylenebisacrylamide;

- 10 wt% of glycerine;

- 65 wt% of deionized water.

Then, they added powder and polyvinyl pyrrolidone (PVP) K-15 as dispersant and 1 wt% of the premixed solution of 2-hydroxy-2-methyl-1-phenyl-1-acetone as photoinitiator.

4.3.2. Photopolymerization

The most common reaction used to manufacture parts by SLA is the "radical photopolymerization". The role of the photoinitiator is to start polymerization and hardening of the system by absorption of laser beam energy (hν). To do so, the photoinitiator PI forms two free radicals 2R* (Equation (4.1)) which can form with the monomer(s)/oligomer(s) M, in turn, a new radical RM∗. This new radical can propagate the polymerization reaction (Equation (4.2)). It is then the terminal carbon-carbon double bonds of the monomer(s)/oligomer(s) that break to allow the formation of covalent bonds with free radicals. By successive addition of monomer/oligomer units to the extending polymer chain $RM*_{n+1}$, larger radicals are formed by consumption of the carbon-carbon double bonds (Equations (4.3) and (4.4)) until the end of the polymerization process (Equation (4.5)).

| Initiation | $PI + h\nu \rightarrow PI^* \rightarrow 2R^*$ | (4.1) |

$$R^* + M \rightarrow RM^*$$ (4.2)

| Propagation | $RM^* + M \rightarrow RMM^*$ | (4.3) |

$$RM_n^* + M \rightarrow RM^*_{n+1}$$ (4.4)

| Termination | $RM_n^* + R'M^*_m \rightarrow RM_n + R'M_m$ | (4.5) |
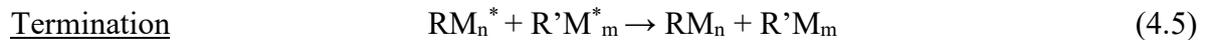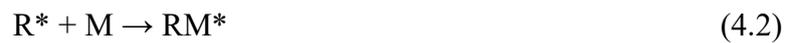
In summary, under the action of a light source, the photo-initiator releases free radicals that will allow the reticulation of the monomers to lead to a rigid polymeric phase around the ceramic grains (*Figure 4.2*).
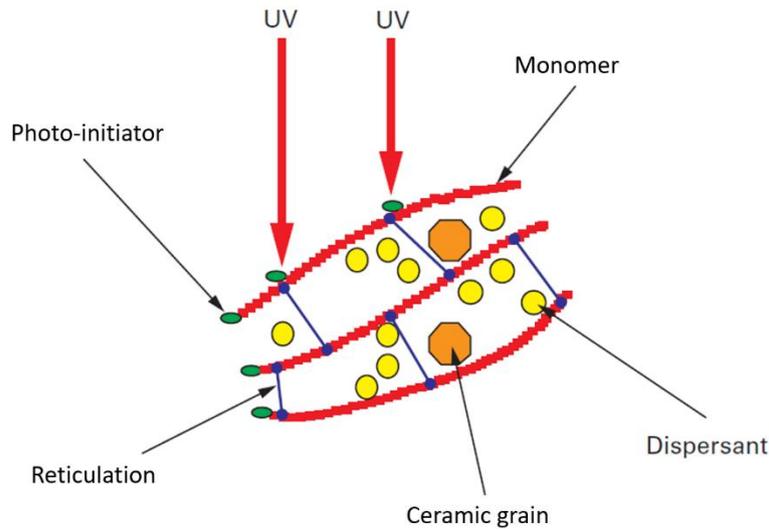
Figure 4.2 : Constituents of a reactive suspension [6]

4.4. Exposure and polymerization

Polymerization under UV laser beam is the basic mechanism of SLA process. The first aspect of the phenomenon was presented in the previous part, with the radical photopolymerization reaction. The second aspect of the phenomenon lies in the delimitation of the phenomenon in space, i.e. the hardened region as a function of the energy emitted by the UV laser beam [8].

During the UV laser passage, the material receives a certain amount of energy by unit area, called "exposure" or "energy dose". Exposure is then defined as the rate of energy received by the photosensitive system per unit area, expressed in mJ/cm².

4.4.1. Cure depth and width for an ideal Gaussian beam with no scattering

Most of the time, the laser used is considered as Gaussian, meaning its intensity decreases according to a Gaussian law from the center of the beam (*Figure 4.3*).
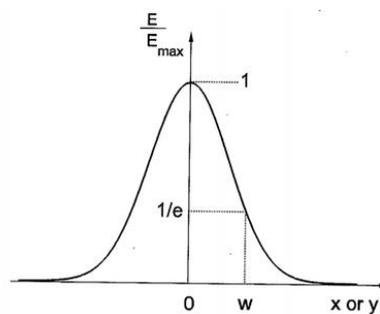
Figure 4.3: Gaussian intensity profile [39]

The distribution of intensity at the surface ($z = 0$) of a Gaussian laser beam varies in the width direction y as [12]:

$$I(y, z = 0) = I_{max} \exp\left(-\frac{2y^2}{W_0{}^2}\right) \qquad (4.6)$$

where y is the distance from the center of the beam and z is the depth from the surface of the suspension; I_{max} is the peak intensity and W_0 the gaussian laser beam radius (w in *Figure 4.3*).

The exposure is equal to the intensity multiplied by illumination time (E = I*t) [12] :

$$E(y, z = 0) = E_M \exp\left(-\frac{2y^2}{W_0{}^2}\right) \qquad (4.7)$$

With E_M the maximum exposure.

Thus, E(y,z = 0) and the intensity are supposed to have the same positional dependence. The resin being absorbent, the exposure at any point within the suspension follows a Beer-Lambert law, meaning that the energy attenuates logarithmically with depth z as:

$$E(y, z) = E(y, z = 0) \exp\left(-\frac{z}{D_p}\right) \qquad (4.8)$$

With D_p the laser penetration depth.

Then, replacing E(y, z = 0) in the equation (4.8) by the equation (4.7):

$$E(y, z) = E_M \exp\left(-\frac{2y^2}{W_0{}^2}\right) \exp\left(-\frac{z}{D_p}\right) \qquad (4.9)$$

Tarabeux et al. [11] have shown that E_M depends on the laser power (P_L), the scan speed (V_L) and on the laser beam radius (W_0) as:

$$E_M = \sqrt{\frac{2}{\pi}}\left(-\frac{P_L}{V_S W_0}\right) \qquad (4.10)$$

Finally, to describe the exposure in the bulk material [12] [11]:

$$E(y,z) = \sqrt{\frac{2}{\pi}}\left(\frac{P_L}{V_S W_0}\right)\exp\left(-\frac{2y^2}{W_0{}^2}\right) \exp\left(-\frac{z}{D_P}\right) \qquad (4.11)$$

Thus, exposure depends on the depth z and on the distance from the center of the beam y (*Figure 4.4*).
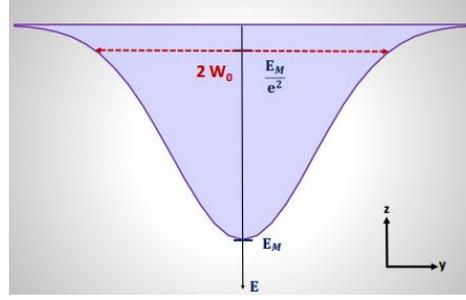
Figure 4.4 : 2-dimensional schematic view of exposure (27)

D_p is the laser penetration depth, defined as the depth in the material where the intensity is reduced by 1/e compared to the maximum intensity of the beam. It traduces the absorption phenomenon, which depends on the reactive system nature and on the laser beam wavelength. This coefficient can be experimentally determined with logarithmic law given by [12]:

$$C_d = D_p \ln \frac{E_M}{E_C} \tag{4.12}$$

Where C_d is the depth of polymerization, and E_C is the critical energy of polymerization, i.e the minimum energy required to start a polymerization reaction. For a loaded monomer, D_p is function of the volume concentration of powder, the particle diameter and the refractive index difference between the UV curable solution and ceramic powder [40]. In fact, D_p can be given by [13]:

$$D_p = \frac{2d}{3Q\phi} \tag{4.13}$$

$$Q = \left(\frac{\Delta n}{n0}\right)^2 \left(\frac{d}{\lambda}\right)^2 \tag{4.14}$$

Where d is the mean particle size of the ceramic powder, ϕ is the volume fraction of the ceramic powder in the suspension, λ is the wavelength of the irradiation, $n0$ is the refractive index of the resin, Δn is the difference in refractive index between the ceramic powder and the monomer solution.

And thus equation (4.12) can be written as:

$$C_d = \frac{2d}{3Q\emptyset} \ln \frac{E_M}{E_C} \tag{4.15}$$

$$C_d = \frac{2d}{3\phi} \left(\frac{n0 \ \lambda}{\Delta n \ d}\right)^2 \ln \frac{E_M}{E_C} \tag{4.16}$$

Moreover, during the laser passage, polymerizable system interacts with the UV laser beam. As mentioned above, the cured region resulting from this interaction can be described by the cure depth C_d but also with the half cure width C_w, creating a 2-dimensions system (*Figure 4.5*).
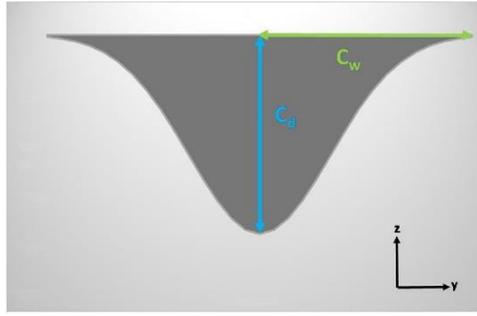
Figure 4.5 : 2-dimensional schematic view of the polymerization depth and half-width [8]

Jacobs showed that the width of the cured line is related to energy dose E_M, the critical exposure E_C, and Gaussian beam width W_0 as :

$$C_w = \sqrt{2}\ W_0 \ln \frac{E_M}{E_C} \qquad (4.17)$$

However, ceramics suspensions are different than conventional photopolymers, largely because ceramic grains cause scattering of the UV radiation.

4.4.2. Scattering phenomenom

Hinczewski et al. [40] has proposed an empirical modification of equation (4.17) for the linewidth of ceramic suspensions, relating the cure width to the energy dose. The Hinczewski model is given for alumina suspensions, by the following equation:

$$C_{Hincz} = F_1 \sqrt{\ln \frac{E_M}{E_{Hincz}}} \qquad (4.18)$$

where F_1 and E_{Hincz} are fitting parameters which depend on the Gaussian beam width and materials parameters (refractive index, solids loadings, etc.). However, according to Gentry et al. [12] this model has a limitation based on the Gaussian light source. This model seems to be no longer valid for higher mode lasers or for more uniform intensity distributions. Additionally, the observed cure widths can be many times larger than the beam width, such that the beam shape is less significant.

Thus, ceramics grains create heterogeneities that lead to a phenomenon of light scattering and impacts polymerization. Indeed, the introduction of ceramic particles of micron and submicron sizes, with an optical index different from that of the resin in the photosensitive system, leads to a diffusion phenomenon during the insolation of the layers.

The scattering phenomenon depends essentially on [8] :

- The nature of the ceramic material

- The percentage of ceramic in the suspension

- The particles size, shape and the granulometric distribution

-   The difference in refractive index between the ceramic powder and the polymerizable system

The scattering of light from ceramic particles can be approximated by the Mie model [12], incorporating a structure factor. This latter allows to account the cross-interactions that comes from the high-volume fraction of ceramic powders. The effect of ceramic particles on the scattering process is related to their refractive index contrast:

$$\frac{\Delta n}{n_0} = \frac{n_{cer} - n_0}{n_0} \tag{4.19}$$

where n_{cer} is the refractive index of the ceramic particles and n_0 is the refractive index of the liquid medium.

For suspensions that have a small refractive index difference between the monomer and the powder, the majority of the energy propagates in the forward direction. Increasing the refractive index contrast ($\Delta n/n_0$) increases the portion of the energy that is scattered to sides. Moreover, this overall widening of the laser beam within the system caused by scattering has been demonstrated by a study on semi-transparent polymer [41]. Consequently, the change in the polymerization process can be described as a widening of the Gaussian laser beam within the reactive system, corresponding to an increase in the half-width of polymerization and a decrease in the depth of polymerization (*Figure 4.6*).
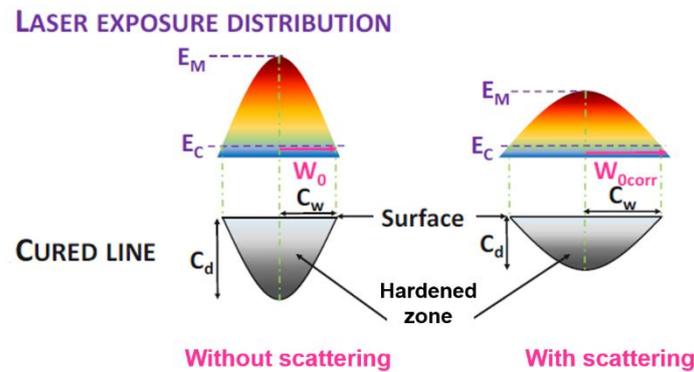
Figure 4.6 : Impact of the scattering phenomenon on the distribution of the laser beam exposure and the hardened line [11]

4.4.3. Homogeneity of polymerization

The laser line construction and layer construction and the limitation of the polymerization depth (C_d) leads to polymerization inhomogeneities (polymerization rate) within the workpiece. The rate of polymerization will directly impact the shrinkage during polymerization and the stiffness of the green part. These disparities affect the physical properties of the green or sintered parts, such as the mechanical properties. It is therefore important to ensure that the system hardening in the volume is as uniform as possible.

The homogeneity of polymerization will depend on the hatch spacing h i.e. the distance between two consecutive laser lines (*Figure 4.7*) and the polymerization depth C_d.
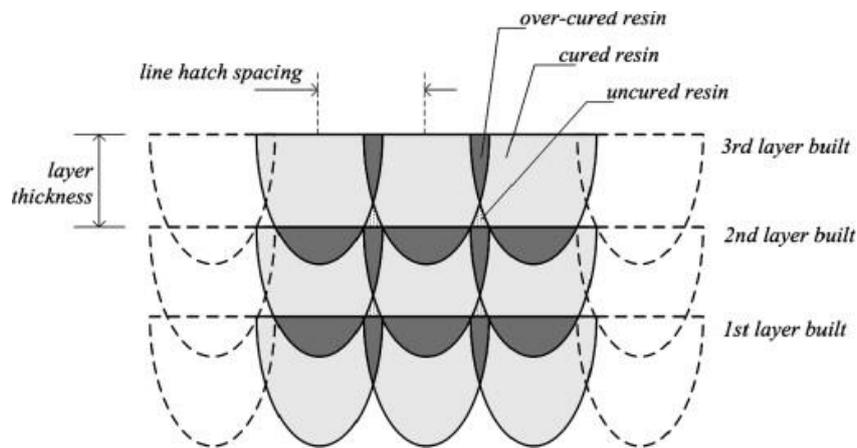
Figure 4.7 : Microstructure section of parts showing three constructed layers [42]

The hatch spacing is mainly set according to the half-width of polymerization C_w, which will impose the dimensional resolution, but also taking into account the manufacturing time. The depth of polymerization C_d will fix the thickness of the layers in order to ensure adhesion between two successive layers and to avoid delamination between layers. It has been shown that, under certain experimental conditions, the laser beam could influence the alumina-based photopolymerizable system on 5 layers of 50µm, i.e. a polymerization depth of 250µm [8].

To conclude on this part, the region hardened by polymerization will depend on the absorption of the laser beam by the photosensitive system as well as on the light scattering due to the fine ceramic particles. To have a polymerization reaction, E(y,z) must be higher than E_C (critical polymerization energy) and to ensure a good chemical bond between layers, the depth of polymerization must exceed the depth of the slices.

5. Post-processing: drying, debinding and sintering

Ceramic green bodies are formed from a polymerized body, also known as a polymer network, in which ceramic particles are trapped. In order to obtain dense and operational ceramic parts, it is necessary to carry out post-treatment steps. These steps consist of debinding followed by sintering.

5.1. Cleaning and drying

After removing the solid part from the vat, it remains liquid suspension in holes and other open structure. Thus, this uncured suspension trapped needs cleaning, with water or alcohol. However, for parts with tight interior features this operation can be delicate [43] and during cleaning stage, grains must not come apart the resin.

Then, when using system based on aqueous acrylamide, it is then important to dry the part to avoid defects apparition. Drying can be conducted in air or in liquid desiccant.

5.2. Debinding

The debinding, which consists in removing the binder i.e the polymer matrix, is a critical step for each slurry-based forming method. The residual carbides resulting from undecomposed organics tend to lower the performance of the ceramic parts and have to be eliminated [13].

The debinding mechanism generally includes a combination of evaporation of low molecular weight polymers, oxidation decomposition and thermal degradation but the components of the system evaporate and decompose at different temperatures and have different behavior. Consequently, during debinding, the parts lose weight and become smaller, the reductions depending on the composition and the proportion of the organic components of the ceramic powder and especially on the cycle temperature chosen. Furthermore, the physical characteristics of the ceramic powder, such as the particle size and the size distribution influence the debinding behavior [44] .

According to Pfaffinger et al. [44], "in the debinding step the organic matrix is burned out at temperatures ranging up to 550°C". However, in some articles, debinding temperature can be higher than 550°C, ranging up to 1000°C [17]. However, the choice of such a high debinding temperature can be questioned. Indeed, the sintering process (see next section) could start at such temperature and could alter the part if not controlled.

During debinding, the diluent evaporates creating open porosity inside the structure of the green part. This porosity, although representing a disadvantage for the final part, has an advantage here since it facilitates the evacuation of pyrolyzed polymers [44].

5.3. Sintering

After shaping and debinding, the assembly of the ceramic grains is brittle, the grains being weakly held together. This is why a second phase, called "sintering" in necessary. Sintering can

be described as the change from a powdered compact to a coherent material under the action of heat. Thanks to the effect of the heat, "bridges" are created between the grains due to internal transfers of materials (*Figure 5.1*). The driving force of sintering, activated by temperature, is then the reduction of the powder surface energy [45].
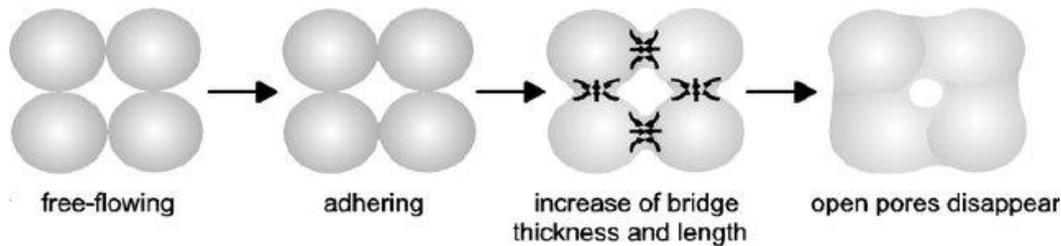

free-flowing   adhering   increase of bridge thickness and length   open pores disappear

Figure 5.1 : Different phase of sintering process [46]

This physical phenomenon is complex and not totally understood yet. It has been the subject of much theoretical work to understand the reaction mechanisms and to improve the empirical processes used in industry [19].

Sintering requires high temperatures, above the "Tammann" temperature of the materials. The so-called Tammann temperature of a material is the temperature above which the atomic mobility can no longer be neglected, which progressively modifies many of its physico-chemical properties. It is not a precise temperature but a "technological" temperature, evaluated at about 0,6 times the melting temperature (expressed in kelvin). For instance, above the Tammann temperature, mechanical properties such as hardness and creep and chemical properties such as atom diffusion and reactivity are modified [19].

During sintering, the shape of the part is preserved but its volume generally decreases (shrinkage phenomenon).

5.4. Shrinkage

Removing the photosensitive resins will lead to shrinkage of more than 10 % and deformation of ceramic parts [15]. According to Gonzalez et al. [47], when sintered at 1600 °C, the expected shrinkage of the ceramic materials fabricated with SLA was about 20-25 % in the X or Y directions, and about 25-30 % in the Z direction. Thus, shrinkage must be considered during CAD stages as well as possible deformations of the part. A first part is created and the dimensions of the digital part are adjusted after shrinkage calculation.

Different research has been made to reduce these inconveniences. One solution could be to increase the inorganic powder content in the slurry. However, these procedures are really complicated and not adapted for industries. Li et al. [48] tried to use surfactants to prepare alumina suspensions, and it was shown that oleic acid provides the best flexural strength. They obtained a 40 vol% alumina suspensions and density of 95 % after sintering. Zhang et al. [49] also managed to prepare alumina slurries (60 vol%) with 5 wt% KOS110 and high solid loading.

6. Influence of feedstock preparation on the density of alumina parts

As seen before, the curing depth C_d is an important parameter which determines the homogeneity of polymerization and thus the accuracy of the formability. As a reminder, the expression of C_d is given by the equation (4.11) and D_p is function of the volume concentration of powder, of the particle diameter and of the refractive index difference between the UV curable solution and ceramic powder [40]. It is therefore possible to modify cure width by adjusting particle size and volume fraction of powder, which will allow to meet the requirements of formability and sinterability.

$$C_d = D_p \ln \frac{E_M}{E_C} \qquad (4.11)$$

Previous research work has shown that a dense green alumina part can be obtained by choosing appropriately the size distribution of particles in the suspension. In particular, Tari et. Al [50] have demonstrated that, in colloidal processing, by combining an appropriate ratio of fine and coarse grains, it was possible to obtain higher density bodies. Therefore, starting from this observation, Wu et al. [13] decided to test different alumina particles size in suspension to print parts by SLA. They tested a suspension with only micro-sized powders of 9µm, another one with only nano-sized powders of 50 nm and finally, the tested a suspension with both nano and micro-sized powders with a 1:1 weight ratio (*Table 6.1*). For all samples, suspensions contained 65 wt% of alumina powders.

Table 6.1 : Starting materials used for the fabrication of the three different types of samples

Samples	Starting material
Sample 1	Micro-sized Al_2O_3 powder
Sample 2	Mixture of micro-sized powder and nano-sized Al_2O_3 nanoparticles
Sample 3	Nano-sized Al_2O_3 powder

Samples have been debound in air and sample 1 and 2 were sintered at 1750 °C, while sample 3 was sintered at 1600 °C for 4 h in a furnace. This difference of heating will be explained later in the section 9.3.2 which talks about debinding.

Morphologies obtained as-printed are compared in the *Figure 6.1*. It seems that for samples with unimodal distribution, i.e sample 1 (*Figure 6.1 (a)*) and sample 3 *(Figure 6.1 (c))*, particles are homogenously distributed throughout the polymer matrix. However for the bimodal distribution (*Figure 6.1 (b)*), nanoparticles appear to be embedded between the micro-sized particles and any inhomogeneity in the green bodies may result in an accumulation of stress during sintering [13].
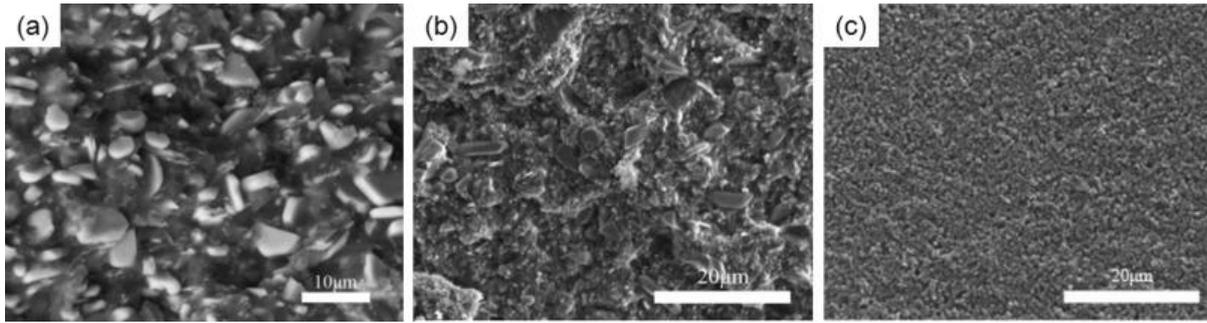
Figure 6.1 : SEM images of the green bodies (a) sample 1, (b) sample 2, (c) sample 3. [13]

Morphologies obtained after thermal debinding and sintering are shown in *Figure 6.2*. No sample shows defects, such as crack or delamination, after sintering, not even sample 2 whose as-printed microstructure was inhomogeneous.
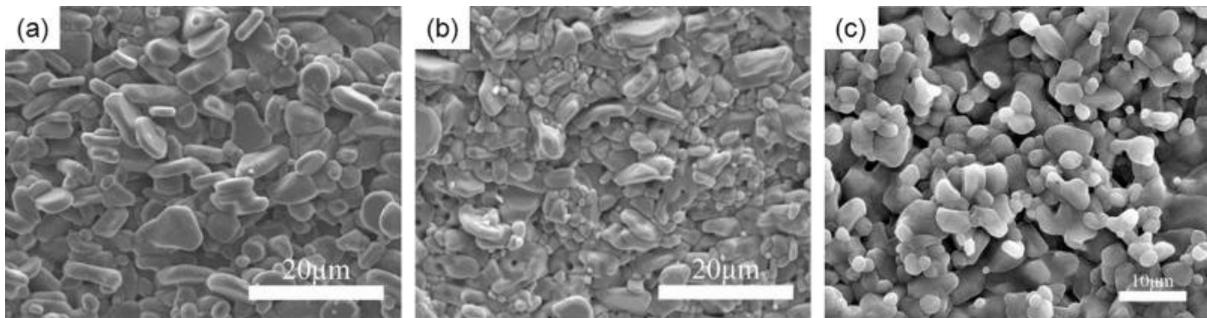
Figure 6.2 : SEM images revealing the morphology of the samples subjected to the thermal debinding process: (a) sample 1, (b) sample 2, (c) sample 3. [13]

Regarding all densities (*Figure 6.3*), it clearly appears that micro-sized particles lead to the lowest density, about 65.2% for sample 1, what can be explained by the microstructure. Indeed, *Figure 6.2(a)* reveals a loose morphology with micro-sized particles piling up irregularly. This low densification is probably due to the sintering kinetics which is lower because of small surface energy of the micro-sized particles.
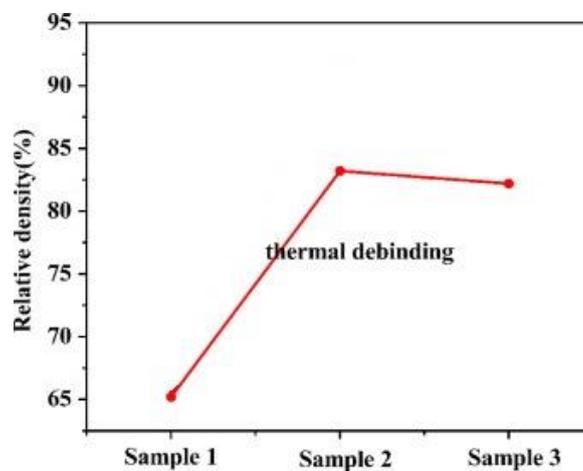
Figure 6.3 : Densities of the different samples after thermal debinding. [13]

On the other hand, sample 2 with bimodal distribution and sample 3 with nano-sized particles have higher densities, 83,2% for sample 2 and 82,2% for sample 3. For sample 3 with nano-sized particles (*Figure 6.2(c)*), grains are homogenously distributed but porosity is clearly visible in the microstructure. However in sample 2 (*Figure 6.2(b),* pores seem to be filled with nanoparticles, i.e spherical alumina nanoparticles take up the gaps between the micro-sized grains, and this combination explains why the density of this sample is the highest among other.

To conclude, the results of this study [13] show that the density of the samples containing both micro-sized and nano-sized particles is largely higher than the monolithic micro-sized powder and slightly higher than the nano-sized powder. Using a bimodal distribution is then a feasible and low-cost approach to obtain denser parts.

7. Impact of the process parameters on properties

7.1. Parameters influencing the stereolithography process

Many factors have an impact on the SLA process. These factors are either related to the photosensitive system used or to manufacturing parameters such as laser beam speed, power, layer thickness, and hatch spacing (*Figure 7.1*).
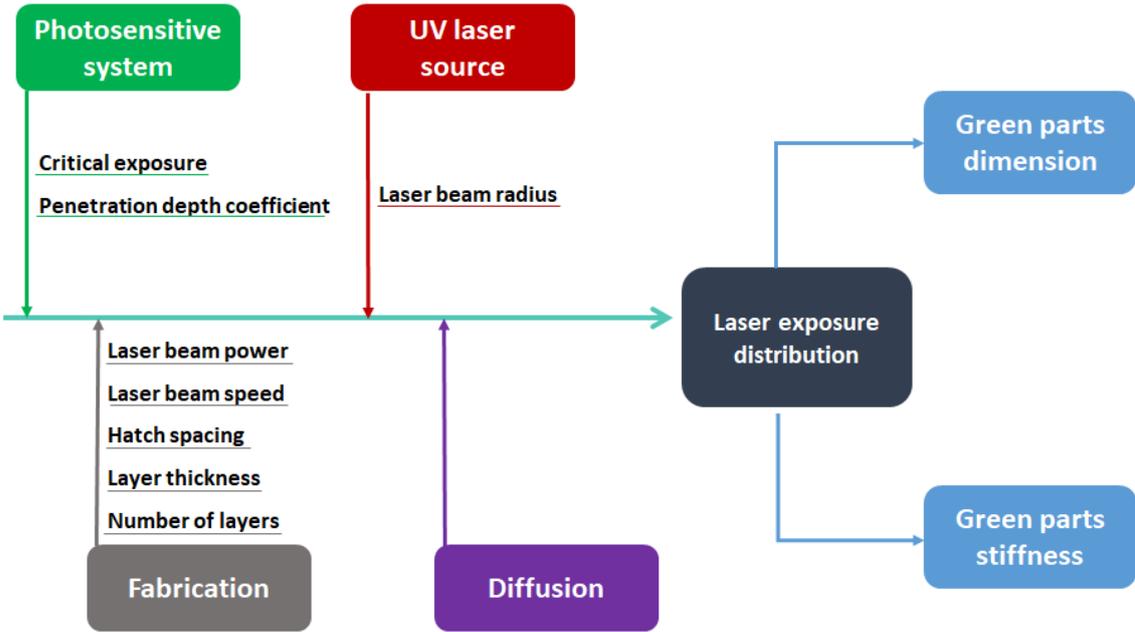
Figure 7.1 : Diagram of factors influencing the SLA process [8]

These different parameters have an influence on the dimension and stiffness of the parts and therefore on the mechanical properties.

7.2. Impact of speed, power and hatch spacing on mechanical properties

J. Tarabeux (doctor from the University of Limoges) and K. Ciężki (Master at the University of Limoges - IRCER) studied different combinations of printing parameters laser speed , laser powder and hatch spacing, to understand their impact on the density of sintered parts and on the mechanical properties of green and sintered parts in alumina by SLA. Experiments were made with a photosensitive alumina paste marketed by 3D-Ceram, loaded at 57 vol.% and having the following particle size distribution: d10=0,5µm, d50=1,61µm, d90=4,28µm. The IRCER SLA machine used is equipped with a UV laser source with a wavelength of 355nm (Innolas Nanio AIR 355 3W).

As a reminder, the expression of exposure within the bulk material is:

$$E(y,z) = \sqrt{\frac{2}{\pi}} \left(-\frac{P_L}{V_L W_0}\right) \exp\left(-\frac{2y^2}{W_0{}^2}\right) \exp\left(-\frac{z}{D_P}\right) \tag{4.10}$$

The laser speed (V_L) and laser power (P_L) take part directly in the exposure expression. Consequently, different combinations lead to different exposure values. Hatch spacing (H) will, however, influence the homogeneity of polymerization.

The combinations tested are the following, where E_{10L} is the maximum exposure received by ten continuous layers of alumina paste :

Table 7.1 : Experimental test plan

Experiment	E01	E02	E03	E04	E05	E06	E07	E08	E09
P_L [mW]	125	125	100	175	175	175	250	225	225
V_L [mm/s]	2500	3500	5500	2500	3500	4500	1500	3500	4500
H [µm]	20	30	20	30	40	20	40	20	30
E_{10L} [mJ/cm²]	465,7	222,2	170,0	434,6	238,6	362,2	776,0	598,7	310,4

7.2.1. Results obtained on green alumina parts

A first study was carried out on green alumina parts by J.Tarabeux [8]. It showed that the mechanical properties of the green parts depend on the laser exposure within the photosensitive system. She showed that the higher the power, the greater the hardening of the system and the higher the speed, the lower the hardening of the system. Finally, the greater the hatching distance, the lower the hardening of the system. This is logical since with higher power and lower velocity the system receives more energy. Furthermore, with small hatch spacing, system receives also more energy, but in several time.

Only Young's modulus was studied in this PhD thesis. These moduli were measured by coupling mechanical tensile tests with a digital image correlation technique, a complex method detailed in the thesis [8].

According to the results obtained by J. Tarabeux with parts built following the experimental test plan of the *Table 7.1*, Young's moduli vary from 970 MPa for E03 to 1580 MPa for E08, that is to say a difference of 610 MPa between the lowest and the highest modulus. Consequently, the control of the stiffness of the raw parts requires a wise choice of the manufacturing parameters.

Comparing Young's modulus and E_{10L} exposure, she found that the two parameters were related in a quasi-linear way on a semi-logarithmic scale, with a correlation coefficient of 0.97. This hypothesis of linearity is reinforced by the fact that with the linear regression (in red in *Figure 7.2*), a null Young's modulus is obtained for an exposure of 20 mJ/cm², a value which corresponds to the critical polymerization energy (E_C) of the system studied. Thus, when the exposure is approximately equal to the critical polymerization energy, the system is liquid and therefore the value of the modulus becomes zero.
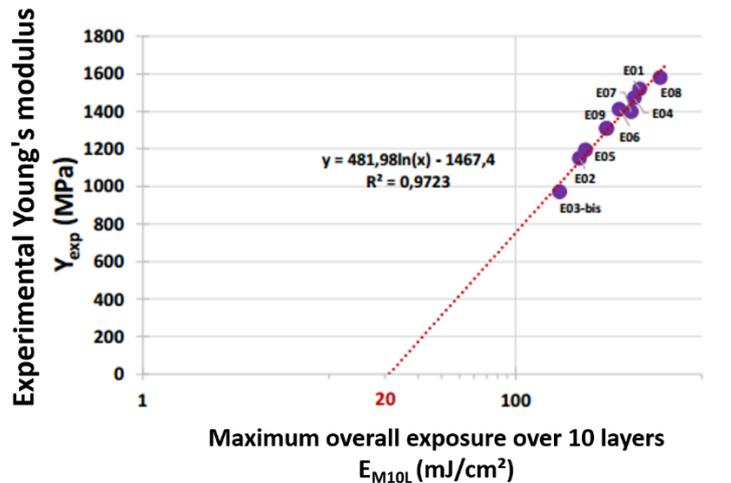
Figure 7.2 : Young's modulus as a function of E10L for green alumina parts [8]

7.2.2. Results obtained on sintered alumina parts

A second study was conducted by J. Tarabeux [5] and K.Cieżk i[11] on sintered alumina parts. The same experimental design as for green parts was followed (*Table 7.1*), but with the addition of a debinding step at 600°C for 30 minutes, followed by sintering at 1650°C for 2 hours.

7.2.2.1. Density

The density can be calculated thanks to Archimedean buoyancy (appendix 1.1). The density values obtained are similar for all samples, regardless of the exposure rate, ranging from 3.75 to 3.78 g/cm^3. These values correspond to a relative density of 95%, i.e. the samples have 5% porosity. However, the supervisor of J. Tarabeux and K. Cieżki told me orally that these results seem unusual and that perhaps the measures were taken in the wrong way. It would therefore be interesting to do these experiments again.

7.2.2.2. Young's modulus

Young's moduli of sintered parts were calculated using the ultrasound technique (Appendix 1.2). This method is more accurate than bending tests and unlike conventional mechanical tests, it is possible to calculate the modulus of anisotropic materials. Indeed, in the case of stereolithographic constructed samples, these latter are considered "transverse isotropic" in the plane (X,Y). This means that properties are isotropic in two directions, X and Y (i.e the properties are the same in these two directions) and are different in the Z direction, the building direction (*Figure 7*.3). This hypothesis has been verified in the thesis of J. Tarabeux [8] where she shows that the ratio between moduli E$_{11}$ (Young's modulus in the X direction) and E$_{22}$ (Young's modulus in the Y direction) varies by a maximum of 2%.
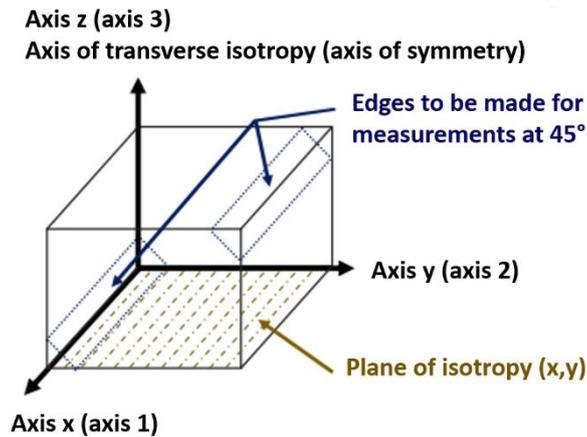
Figure 7.3 : Definition of measurement axes [51]

The Young's moduli measured vary from 270 GPa to 402 GPa (*Figure 7.4*), values in line with those found in the literature in *Table 1.2*, ranging from 260 to 410 GPa, for alumina parts manufactured by conventional processes. These results show therefore that the SLA process is a reliable process and that the post-treatment steps are suitable, despite a densification rate of only 95%.
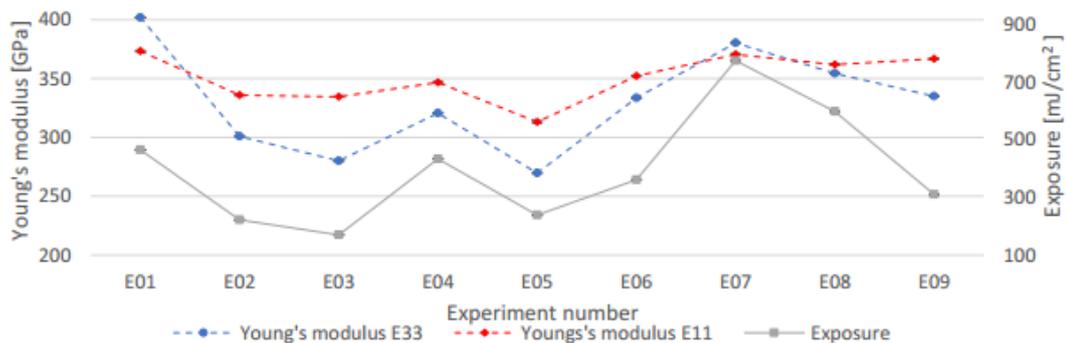
Figure 7.4 : Young's moduli and exposure according to different experiences [14]

For all the tests, Young's moduli E_{11} and E_{33} (E_{33} corresponds to the Young's modulus in the direction Z) follow the same general trend as the E_{10L} exposure. Thus, the printing parameters, which influence the exposure, play an important role in the stiffness of the sintered parts.

A higher rate of exposure induces a stronger curing by polymerization of the ceramic system. In addition, the depth of polymerization depends on the exposure value, i.e. the greater the exposure, the greater the depth of polymerization and therefore the greater the amount of paste cured. Thus, the greater the exposure is, the better the bond between the layers is.

E_{33} is lower than E_{11} for most of the samples and that can probably be explained by an anistropic microstructure (see further in section 8). Indeed, one of the hypotheses put forward by J. Tarabeux to explain the link between exposure and mechanical properties is that the latter will depend on the arrangement of the grains. The arrangement is supposed to be different depending on the rate of exposure and therefore the degree of hardening and polymerisation.

It should be noted that for the highest exposure values, the transverse and longitudinal moduli are almost equal and therefore a high exposure seems to induce less anisotropy in the structure.

7.2.2.3. Maximal strength at break

Stress at break is one of the important mechanical characteristics to be determined for engineering applications. These have been measured by biaxial bending tests (appendix 1.3). Unlike uniaxial bending tests, biaxial bending method has the advantage of generating the maximum tensile and compressive stresses in the central part of the specimen, which eliminates the risk of failure at the ends.

Mechanical four-point bending tests were also carried out in [14], but the results obtained were more scattered and therefore less accurate. As this is a complex and delicate technique, it would be interesting to repeat the four-point bending tests to see if it is possible to increase the accuracy (see Appendix 1.4 for the method).

The stress at break values obtained range from 107 MPa to 164 MPa (*Figure 7.5*), which is lower than the values obtained in the literature for parts manufactured by conventional processes. Indeed, on parts manufactured by pressing in, the stress values obtained by biaxial bending are between 350 and 550 MPa. This difference can be explained by the lower porosity rate stated in Jeong et al. [52], since the powder compaction process ensures better homogeneity of the microstructure.
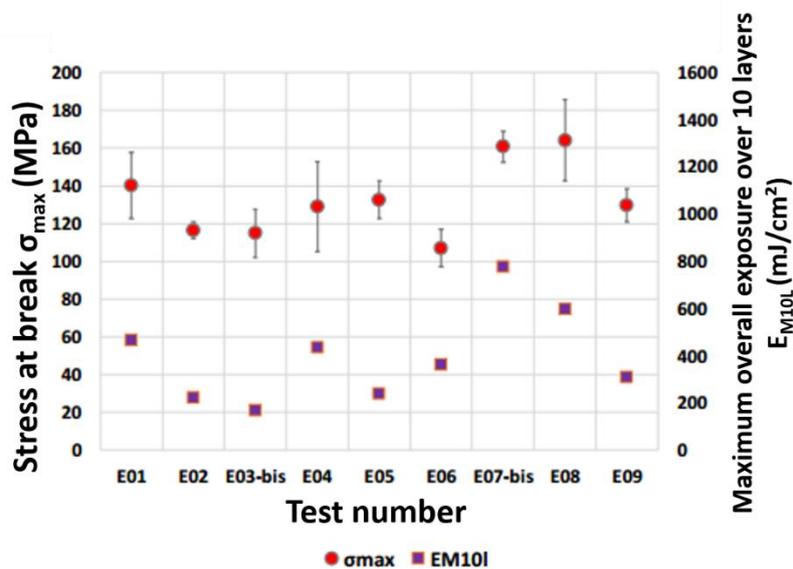
Figure 7.5 : Stress at break and exposure according to experiments (E03-bis = E03 and E07-bis = E07) [8]

The stress-at-break curve follows the same evolution as the exposure, except for experiment E05. This result indicates for the second time that the exposure received during the manufacture of green parts has an impact on the mechanical behavior of sintered parts.

As for elastic characteristics, the value of the stress at break of a material will depend on the arrangement of the grains in its microstructure but it is also impacted by the defects present

within it [8]. However, these differences do not seem to be related to porosities because for all samples, the porosity rate is similar.

7.3. Impact of layer thickness on properties and microstructure

Because of the layer-by-layer construction, SLA samples are subject to delamination or cracking along the boundaries of two adjacent layers. Therefore, in SLA, the micro-mechanical properties across the thickness direction (or along the building direction) are crucial to determine.

Li et al. [16] recently studied the impact of layer thickness on microstructure and on mechanical properties at microscale of green and sintered alumina parts, through nanoindentation (appendix 1.5). Nanoindentation tests provide a better understanding of the role of homogeneity between adjacent layers.

They used a ceramic suspension with 48vol% of alumina powder (SAO-030A, SINOCERA, China) with an acrylate polymer and the samples were printed by a commercial SLA manufacturing system AMC150 (ZRApid Tech., China). They tested 4 different thicknesses, from 30µm to 120µm with a step of 30µm and the samples are respectively named LT30, LT60, LT90 and LT120 (LT for "Layer Thickness"), while laser and scanning speed are the same for all experiments.

Samples were debound by heating in air at $0.5\,°C\,min^{-1}$ from room temperature to 330 °C and then at a rate of $0.2\,°C\,min^{-1}$ until 600 °C. It was kept at 70, 330 and 600 °C for 2 h, respectively. Sintering of the debound body was carried out at $5\,°C\,min^{-1}$ to 1580 °C with dwell time of 2 h.

7.3.1. Microstructure analysis of the green and sintered alumina with different layer thickness

- **Green alumina parts**

For a layer thickness of 30 µm (*Figure 7.6 (a)*) no interface between layers can be seen, the cross-section being perfectly continuous. This means that for thin layers, the curing of each recoating layer is sufficient. However, for thicker layers (*Figure 7.6 (b), (c) and (d)*), parallel lines are visible by a regular contrast indicated by black arrows on relative pictures. The researchers attributed these lines to an insufficient curing between adjacent layers, caused by a limited penetration depth into the suspension. These results show that the thicker the layers are, the greater the risk of cracking along the recoating direction is.

Thanks to the enlargement visible at the top right of the pictures, it can be seen that ceramic powders are interconnected by the cured binder and uniformly distributed for LT30, TL60 and LT90 (*Figure 7.6 (a), (b) and (c)*). However, for LT120, the distribution is not uniform and grain powders tend to agglomerate, resulting in a rougher morphology.

Regarding porosity, this latter start to be critical when the thickness reaches 90µm (white arrows on *Figure 7.6 (c) and (d)).* Pores are probably generated by bubble formation during the

spreading suspension phase. These pores can lead to fracture after sintering if the sample is submitted to stress.
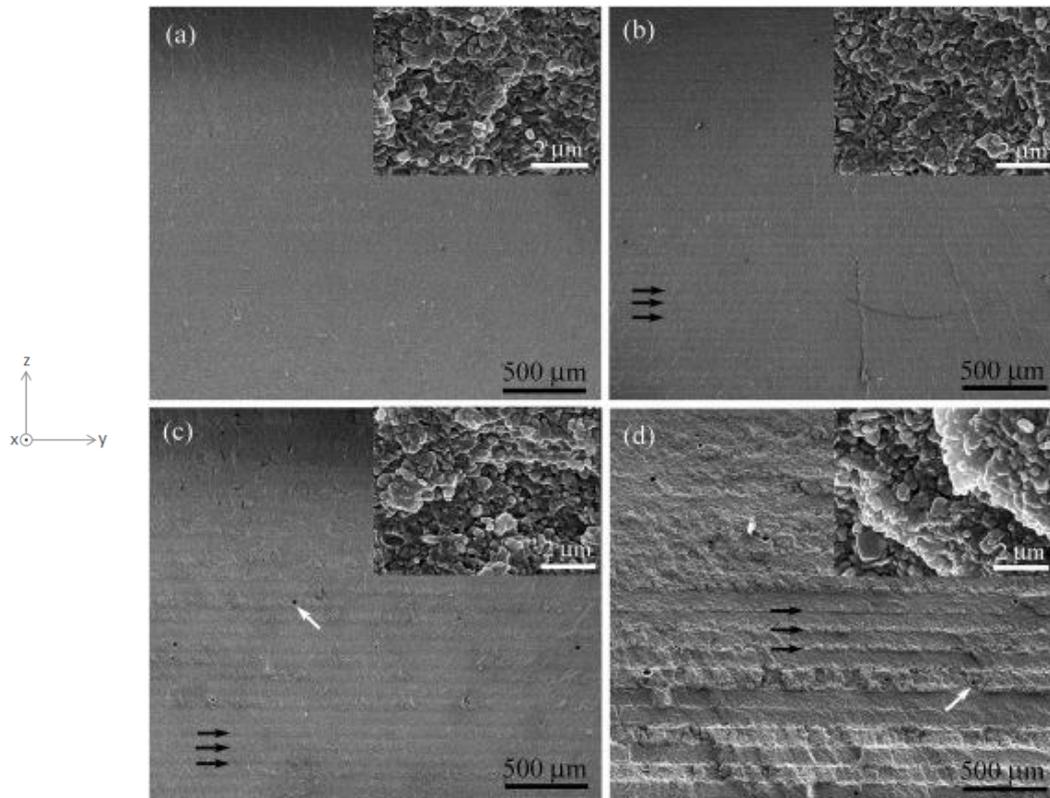
Figure 7.6 : Micrographs of green bodies with different layer thickness: (a) 30; (b) 60; (c) 90; (d) 120 μm.
[16]

- **Sintered alumina parts**

After sintering, the difference of powder grain distribution between LT120 sample and the others disappear. For the four groups (*Figure 7.7 (a) to (d)*), microstructures obtained show a uniform distribution across the thickness direction, without any indication of layer bonding between adjacent layers. This means that insufficient curing does not necessarily lead to cracking or delamination between interfaces, since partially cured interfaces are finally sintered. Porosity is still visible with a lower diameter, about 40-50 μm.

Figure 7.7 : SEM micrographs for the cross-sectional surfaces of sintered alumina with different layer thickness (a) LT30; (b)LT 60; (c) LT90; (d) LT120. [16]

7.3.2. Comparisons of shrinkage and density

Shrinkage rate and relative density have been measured for the four sample groups. There are no significant differences between the groups and length shrinkage is about 21%, width shrinkage ab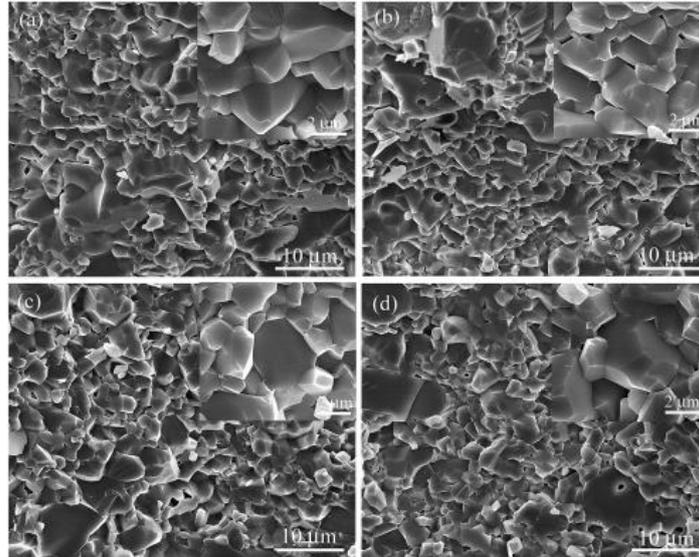out 20%, thickness shrinkage about 23% and volume shrinkage about 51%. Even though there was no clear difference in volume shrinkage rate, the relative density continued to decrease with increasing layer thickness, from 99,1% for LT30 to 97,8% for LT120, which is in line with porosity rate found in microstructures of (*Figure 7.7*).

7.3.3. Variations of hardness and elastic modulus with layer thickness

Hardness and elastic modulus have been plotted as a function of layer thickness (*Figure 7.8*).
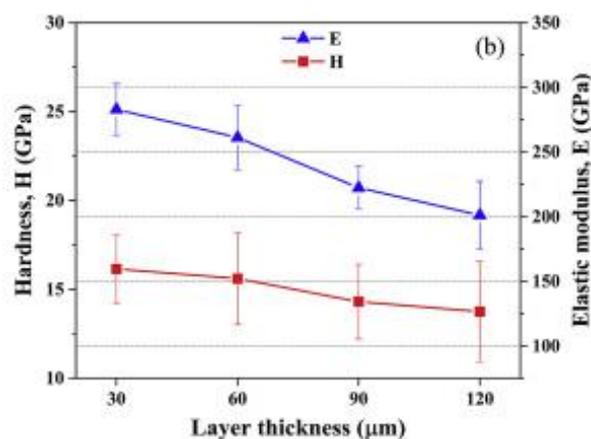
Figure 7.8 : Variations of hardness and elastic modulus of four samples [16]

The average value of hardness H decreases slightly with increasing layer thickness, from 16.2 ± 1.9 GPa to 13.8 ± 2.8 GPa. Authors from the study outline that except the micron-sized pores, low porosity existed at the triple junctions of grains. Therefore, the decrease of H values

is gradual and not dramatic, and these results are in agreement with the microstructure presented above, the latter maintaining its integrity in SLA.

Young's modulus E decreases more sharply with increasing layer thickness. It is likely that these unequal effects on H and E performances are due to lower relative density and by consequence higher porosity for higher layer thickness.

8. Impact of post-process parameters on microstructure and properties

8.1. Microstructures before and after debinding and sintering

A recent study from F. Azarmi and A. Amiri [17] attempted to evaluate the microstructural characteristics of alumina parts manufactured by SLA, before and after debinding and sintering. A second study by F. Azarmi and another author, I.Sevostianov [3] continues the previous research with emphasis on the characterization of elastic and thermal properties of ceramic components produced by SLA before and after sintering.

They used SLA technology (Ceramaker 900) developed by 3D CERAM (Limoges, France) and a confidential alumina suspension, also formulated by the company (called 3DMIX). Nevertheless, it is known that the nominal size of alumina particles used to make the paste were in the range of 2–10 µm. Furthermore, the purity of alumina was $\geq 99.8\%$ with density approximation of 3.9 g/cm^3.

The samples were placed in a furnace for 70-90 hours at 1000°C to burn the residual resin and obtain pure alumina (debinding). Then, the samples were sintered at 1200-1700°C for approximately 20 hours (time depending on the thickness of the sample). All specimens were cut parallel to the printing direction.

8.1.1. Microstructure and composition before and after post-processing

SEM images of microstructures obtained after debinding and sintering are shown in *Figure 8.1*. According to EDS analysis (appendix 1.6), the dark areas are porosities and voids and those in light grey correspond to alumina [17].
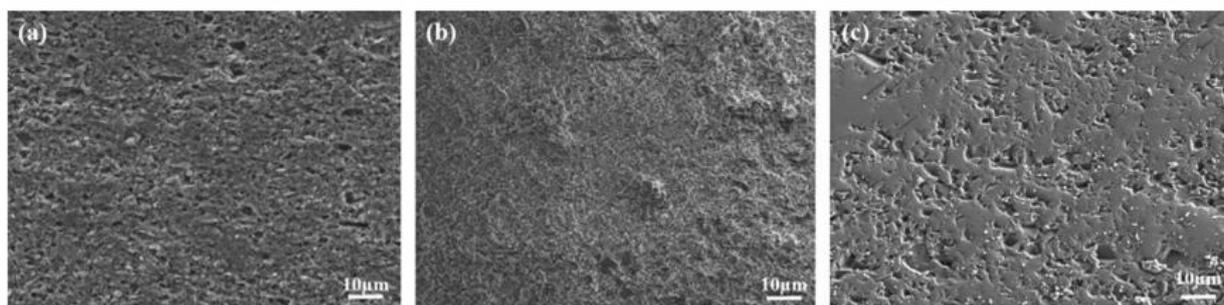
Figure 8.1: SEM images of 3D printed alumina samples (a) as-printed (b) after debinding and (c) after sintering [17]

As expected, microstructural changes are visible from as-printed sample to debinded, and finally to the sintered one and the as-printed sample is very porous due to random agglomeration. However, the sample after debinding (*Figure 8.1 (b)*) appears to have less porosity than the as-print sample (*Figure 8.1(a)*), which is contrary to expectations. Indeed, the evaporation of the resin should lead to a more porous sample by leaving voids behind. The authors hypothesize that the disruption of the intermolecular bonds during debinding resulted

in a "softening" of the sample. Therefore, during surface preparation (grinding and polishing), the pores were coated with soft surface alumina. This cannot therefore result in a mechanical strengthening of the sample by decreasing the porosity, since the porosity has not disappeared, but is simply covered and hidden at the surface. Thus, no conclusions could be drawn on these microstructural changes from the SEM images for sample after debinding.

However, alumina from the sintered sample appears to have grown and to agglomerate more, with noticeable reduction in porosity and voids in the microstructure, compared to as-printed sample. This observation is in agreement with previous reports showing the effect of sintering of alumina processed by conventional methods [9].

Image analysis performed on SEM images together with density measurements have been used to calculate porosity rate and average size of porosity and results are shown in (*Table 8.1*). No results are indicated for the porosity size of debinded samples since images are not reliable and for density of as printed sample since the density is not those of pure alumina but alumina and resin. As expected, porosity rate drastically decreases after debinding, more than 40%. However, if debinding and sintering cause the elimination of porosity, they have not significantly changed the size of remaining voids. Density value after sintering is slightly below the nominal density reported by 3D Ceram (3.9 g/m^3) and the value reported for ideal alumina in literature, 3.98 g/m^3 [2]. Density of samples after sintering increase about 9% compared to only debinded samples, as expected.

Table 8.1 : Results of images analysis and density measurements of as-printed, debinded and sintered alumina samples [17]

Sample	%porosity	Average size of voids and porosity (µm)	Density (g/cm³)
As-printed	19.01 ± 1.12	3.1 ± 0.85	-
Debinded	10.10 ± 3.01	-	3.43 ± 0.14
Sintered	$8.14 \pm 0,85$	2.2 ± 0.63	3.78 ± 0.1

Researchers proceeded to EDS analysis on 5 different zones of each samples and average results are presented in the following table:

Table 8.2 : Chemical composition determined by EDS, Ms% [17]

Constituent	As-printed	Debinded	Sintered
C	23.65 ± 1.32	10.60 ± 0.12	6.02 ± 0.42
O	38.40 ± 0.93	47.42 ± 0.55	54.37 ± 1.26
Al	36.49 ± 0.56	42.98 ± 0.67	39.61 ± 1.69

As said before, the formulation of the suspension is protected by confidentiality, but it is assumed that the resin is based on hydrocarbon molecule. Thus, as expected for a hydrocarbon, a high amount of carbon is present and this amount decreases drastically after debinding which

is a proof of successful elimination of the binder (resin) in the sample. However, carbon decreases even more after sintering, meaning that not all the resin is burned after debinding stage. At contrary, the percentage of aluminum and oxygen increase after debinding and sintering processes.

In addition, XRD analysis (appendix 1.7) have been made on the samples (but not for the paste in order to protect the confidentiality). Patterns were identical for the 3 samples, meaning that the phase is the same before and after post-processing, and the phase corresponds to an α-Al_2O_3 with a rhombohedral structure, known as "corundum". It is logical that during printing and post-processing no phase changing occurs since α-Al_2O_3 is the most stable alumina phase at temperatures above 1200 °C.

8.1.2. Properties before and after post-processing

- **Young's modulus**

Resonant frequency (RFA) measurements, a technique similar to those of ultrasound method (appendix 1.2), have been performed on at least three specimens from each alumina sample [3]. However, no results have been obtained for samples after debinding because of their softness and fragility. For sample as-printed, the average measured Young's modulus was 15.3 GPa and for sample after debinding and sintering, it was 363.3 GPa. Values of Young's modulus before sintering are relative to samples which are composites of polymer and ceramic, and polymers are known to have low Young's modulus (*Table 1.1*). As for J. Tarabeux [8], results show that SLA is a reliable process since stiffness of sintered parts is similar to sample made by conventional methods (*Table 1.2*). However, J. Tarabeux [8] found a Young's modulus of 1.5 GPa for green parts, an order of magnitude lower than the one found by F. Azarmi and I. Sevostianov [3]. This difference is difficult to explain since they both used a commercial alumina paste from 3DCeram. Thus, it is probably due to different printing parameters (unknown for F. Azarmi and I. Sevostianov [3]) and to the different method of characterizations used (micro-traction tests were carried out for J. Tarabeux and F. Azarmi and I. Sevostianov measured by bending vibration method).

- **Thermal conductivity**

Measurements of thermal conductivity coefficient have been performed for each sample and results are shown in *Table 8.3*. The literature value from CES Edupack 2018 for α-Al_2O_3 (which is the only alumina phase detected in all samples in this study) is also included in this table for comparison.

Results show that coefficient of thermal conductivity increases from sample as-printed to sample sintered but as for Young's modulus, the lower conductivity of as-printed model can be explained by the presence of resin, which conductivity is about 0,3 W/m°C (*Table 1.1*). The obtained value for sample after sintering is in the range reported for sintered alumina produced by conventional methods.

Sample	Thermal conductivity coefficient W/m$^\circ$C
As-printed	5.17 ± 1.05
Debinded	8.37 ± 1.78
Sintered	26.81 ± 3.5
Alumina (α-Al$_2$O$_3$) - Highly porous	7–10
Alumina (α-Al$_2$O$_3$) - Cold pressed, Sintered	22–30

8.2. Influence of different drying types on material integrity

Although drying seems to be an anecdotal step in the manufacture of parts, it is to be taken into account since poor drying can lead to defects in the material when using system based on aqueous acrylamide. Zhou et al. [18] tried to optimize drying and debinding in order to produce a defect-free alumina cutting tool via SLA. Two different ways of drying have been tested: a traditional natural drying method in air ("traditional drying") and a drying method using a liquid desiccant ("special drying"). For this latter, samples are immersed on Polyethylene glycol (PEG) as liquid desiccant.

The ceramic suspension is composed of an aqueous acrylamide solution, alumina powders (30 vol%), a dispersant, a photo-initiator. Details on ceramic suspension preparation can be found in the paper [18].

Figure 8.2 (a) shows a sample after traditional drying and *Figure 8.2 (b)* shows samples after special drying and it is clearly visible that when sample goes through traditional drying, it is subjected to deformation because of inhomogeneous shrinkage. This can be attributed to anisotropy of the water evaporation rate which is caused by an inhomogeneous air flow on the surfaces. In contrast, the application of the liquid desiccant resulted in a more uniform water extraction rate and which led to a much more homogeneous shrinkage.
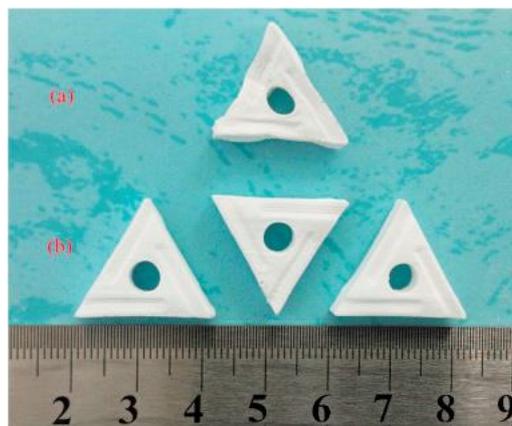

Figure 8.2 : (a) The green body dried via a natural drying process and (b) the green body dried via a liquid desiccant (PEG)-assisted drying process. [18]

Researchers [18] noticed also that relative density after the same sintering but with different drying approaches was different. Indeed, the relative density of the sample dried in air is 96.2% and the one of the samples dried via the PEG-based approach is 99.3%. During traditional drying in air, surfaces always dry before bulk material and thus, surfaces shrink first. Consequently, water inside the body is trapped and cannot escape during density measurement.

8.3. Influence of the debinding type and parameters on defects and density

8.3.1. Influence of the debinding type on defects

In the study of Zhou et al. [18], the type of debinding was also investigated to obtain defects-free parts. Three different cycles have been tested: a pyrolysis in air, a debinding in vacuum and a two-step debinding profile consisting of a vacuum step followed by pyrolysis in air. The air pyrolysis debinding and the vacuum debinding profile are shown in *Figure 8.3(a)*, and the two-step debinding profile is shown in *Figure 8.3(b)*.
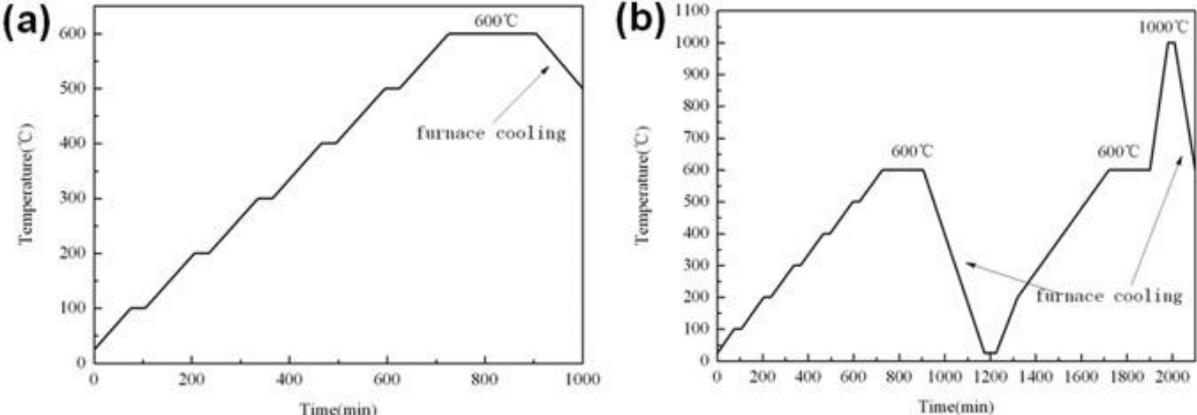

Figure 8.3 : (a) The air pyrolysis debinding and the vacuum debinding profile and (b) the two-step debinding profile. [18]

Debinding in air have led to a numerous number defects such as delamination (*Figure 8.4 (a)*) and cracks (*Figure 8.4(b)*) at the macroscale. Authors attribute these defects "to the very high pyrolysis rate of the organic compound". During pyrolysis, gas is created because of decomposition but it cannot escape from the sample, generating a high pressure inside the body which results in delamination and cracks.
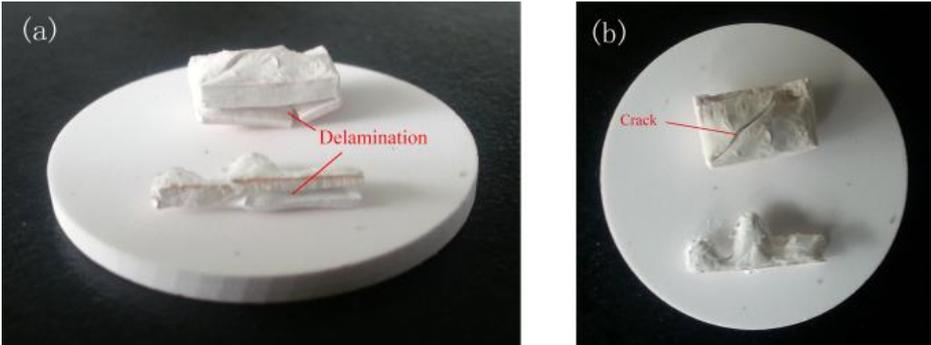

Figure 8.4 : Defects for samples debound in air (a) delamination (b) cracks

Pyrolysis rate can be lowered by using vacuum: in fact in this way gas, during debinding, can escape more easily. However, even if they observed less defects, some cracks appeared as well (*Figure 8.5 (b)*), probably because the residual carbon in the sample after debinding produces gas during the subsequent sintering process.
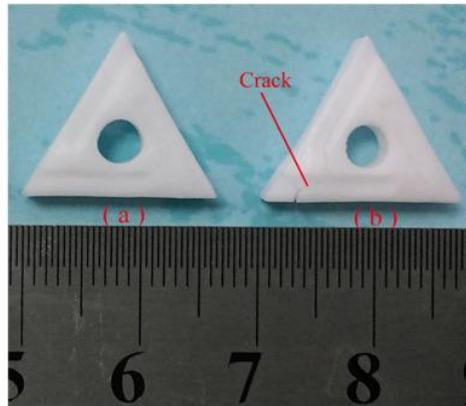

Figure 8.5 : Sintered body obtained from (a) a two-step profile debinding; (b) vacuum debinding. [18]

Finally, to obtain defects-free parts, they adopted a two-step debinding. The first step is identical as the vacuum debinding (*Figure 8.3(a)*) and a second step, in air was done according to *Figure 8.3(b)*. This second step is aimed to eliminate the residual carbon before sintering process and consequently to prevent cracks. With this third method, no defects were observed, so it seems to be the most appropriate. Moreover, cumulating the drying by PEG and the two-step debinding, they obtained a density of 99.3% and a Vickers hardness of about 17,5 GPa, which is suitable for cutting tool. However, debinding is at least twice longer than simple air or vacuum pyrolysis and manufacturers will have to choose between less defect or a quicker method.

8.3.2. Influence of the debinding type on density

In a study mentioned previously by Wu et al. [13], researchers have worked on different grain size distributions for particles in the suspension and on two different debinding methods: thermal debinding and vacuum debinding. Indeed, to select an optimal sintering path guarantees a high density of the green body.

Compared to thermal debinding process, a vacuum debinding process combines the debinding and the sintering cycle into a single processing step and allows to minimize damages caused by the handling of the fragile debound parts. For recall, three different samples have been tested:

Samples	Starting material
Sample 1	Micro-sized Al_2O_3 powder
Sample 2	Mixture of micro-sized powder and nano-sized Al_2O_3 nanoparticles
Sample 3	Nano-sized Al_2O_3 powder

The vacuum debinding was conducted in a tubular furnace under low vacuum conditions. In order to determine the cycles, TGA analysis (appendix 1.8) has been carried out and the curves for the three different samples turned out to be the same. Different exothermic peaks appeared, corresponding at the decomposition of the organics and in order to completely remove the organic components, the debinding process should reflect every detail of the observed decomposition behavior. The temperature was kept constant for a certain period of time when the temperature had reached a value corresponding to one of the exothermic peaks, and the holding time was the same for each of those temperatures (*Figure 8.6*).
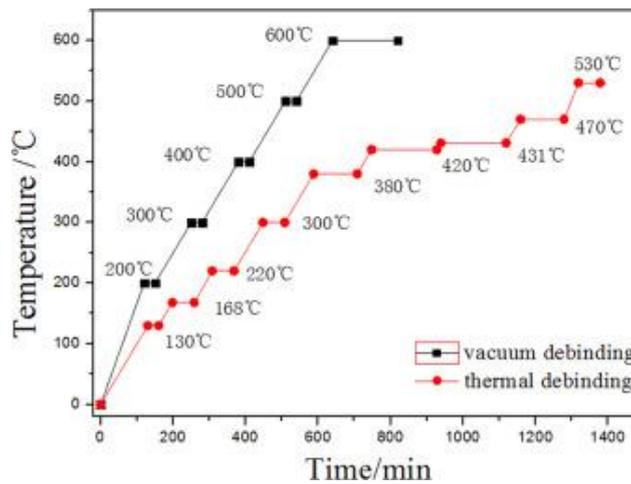
Figure 8.6 : Temperature curves used for the debinding of the Al_2O_3 ceramics prepared through SLA [13]

The cross-section morphology of the samples subjected to the vacuum debinding can be seen in *Figure 8.7*, together with the one of samples subjected to the thermal debinding (*Figure 6.2* is the same as figure *Figure 8.8*, just for comparison with *Figure 8.7*). Furthermore, the relative density is compared in *Figure 8.9*.
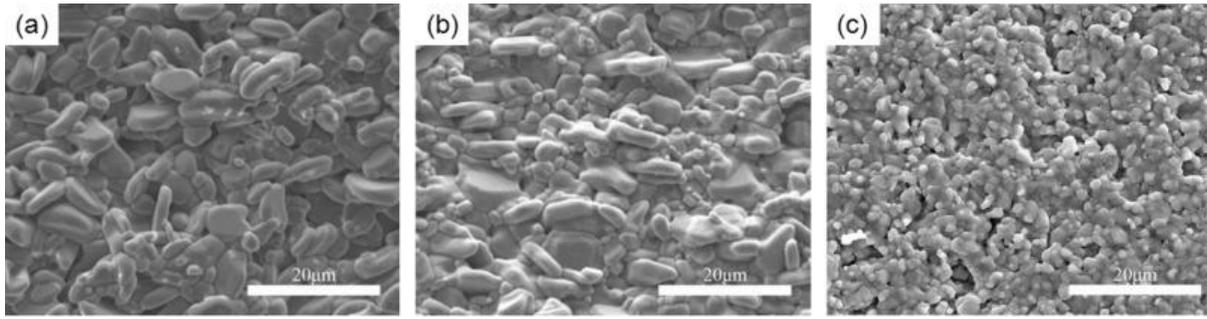
*Figure 8.7 : SEM images revealing the morphology of the samples subjected to the **vacuum debinding** process: (a) sample 1, (b) sample 2, (c) sample 3. [13]*
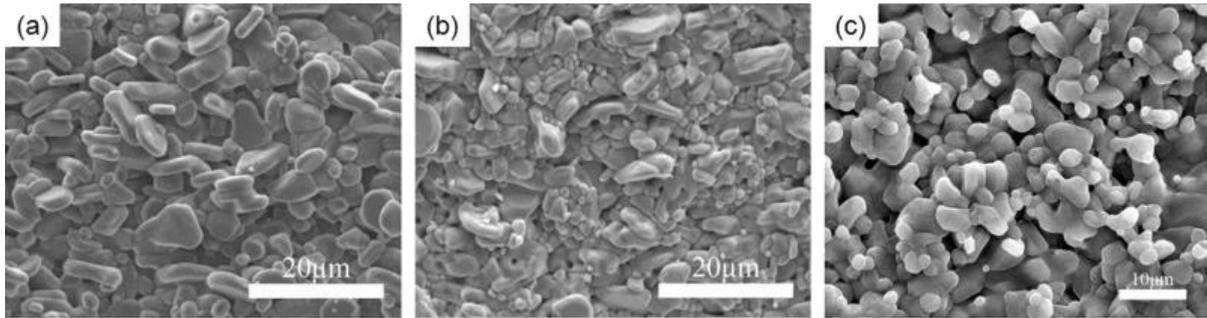

*Figure 8.8 : SEM images revealing the morphology of the samples subjected to the **thermal debinding** process: (a) sample 1, (b) sample 2, (c) sample 3. [13]*

For both debinding methods, there was no obvious delamination and no cracks formed. Morphologies are almost similar for the two methods. However, sample 2 and sample 3 present more pores when the sample has been subjected to thermal debinding than the same samples subjected to vacuum debinding. This is confirmed by the variation in relative density (*Figure 8.9*) , which is 83.2% and 82.2% respectively for samples 2 and 3 subjected to thermal debinding, compared to 91.2% and 89.2% for samples subjected to vacuum debinding. Thus, except for samples 1 with micro-sized particles where density is very low and similar for both methods, vacuum debinding is beneficial for density.
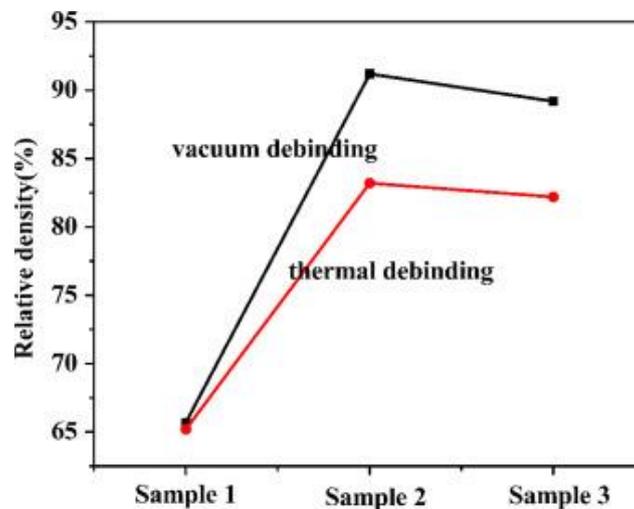

Figure 8.9 : Comparison of the relative densities of the different samples after the vacuum and thermal debinding. [13]

It can be noted in *Figure 8.9* that density evolution of samples subjected to thermal and vacuum debinding follows the same trend i.e samples 2 have the highest density and sample 1 the lowest, but vacuum debinding is more efficient since relative density is higher.

To conclude the considerations for this study [13], the highest density is obtained for samples containing a bimodal distribution of particles in the suspension. In addition, vacuum debinding has a positive effect on final density.

8.4. Microstructure and properties according to sintering temperature

Li et. al [15] investigated the evolution of the microstructure and of the physical and mechanical properties as a function of sintering temperature of alumina cores manufactured by SLA and vacuum sintered. The use of vacuum is intended to eliminate the formation of defects such as cracks caused by residual carbon (from the resin) during sintering and for a better control of shrinkage and thus deformation. Debinding temperature is the same for all experiment but seven different sintering temperatures have been tested, from 1100°C to 1350°C with a delta of 50°C. Details on temperature cycles used and size particle distribution can be found in appendix 2.

8.4.1. Microstructure of samples sintered in vacuum according to sintering temperature

For all sintering temperatures studied, the samples presented delamination (*Figure 8.10*) but no cracks appears, probably thanks to the slow heating rate and vacuum atmosphere that promote junction formation between alumina particles. During sintering, particles grow and connect to each other, but due to the large distance between adjacent layers and thus between particles, an interlayer spacing is formed. To prevent delamination between layers by regulating only sintering temperature does not seem possible.

To ensure continuous bonding between layers, laser penetration depth must be larger than the thickness of the layer spread. Furthermore, as discussed before, interfacial joining between layers is caused by exposure along the Z direction. However, energy along Z direction is distributed less uniformly than in X-Y plane, resulting in weaker connection between layers.
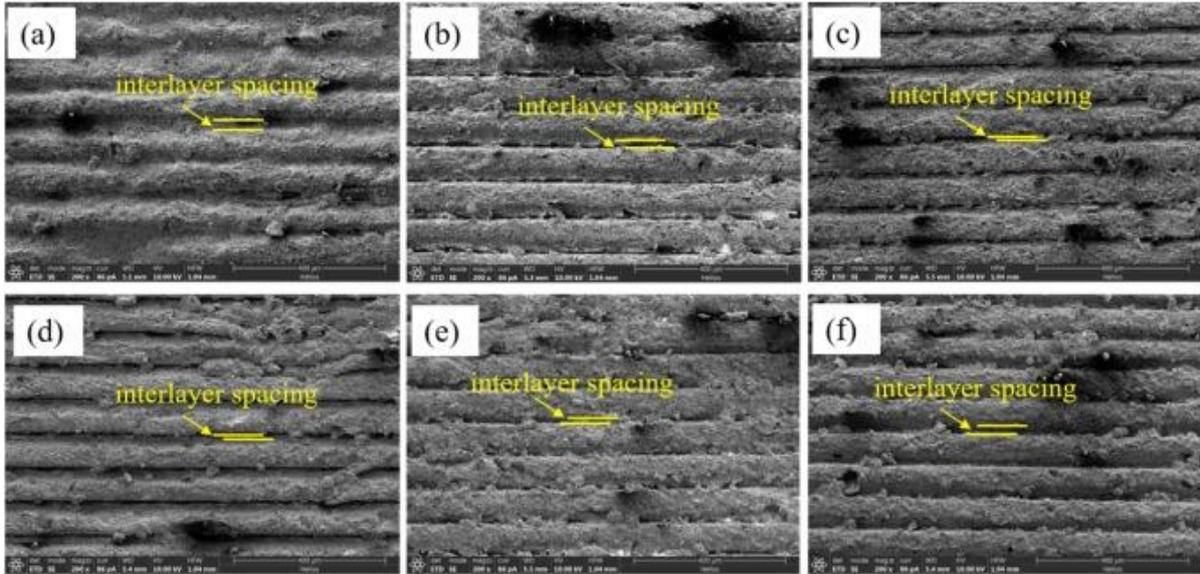
Figure 8.10 : SEM images showing delamination during sintering at (a) 1100, (b) 1150, (c) 1200, (d) 1250, (e) 1300, and (f) 1350 °C. [15]

The evolution of the interlayer spacing is shown in *Figure 8.11*. This distance first decreases, reaching a minimum value of 5.94 μm for sintering at 1200 °C, and then increases as the sintering temperature increased. Alumina sintered at 1100°C has a greater interlayer distance than all other samples because of resin volatilization. Resin volatilization for higher temperatures is compensated by the driving force (reduction of the powder surface energy). Indeed, when the temperature reaches 1150°C, the driving force of the sintering increases and promotes better interlayer bonding and thus the spacing between layers decreases. However, once the temperature reaches 1300°C, the shrinkage of the sample increases considerably, causing an increase in delamination.
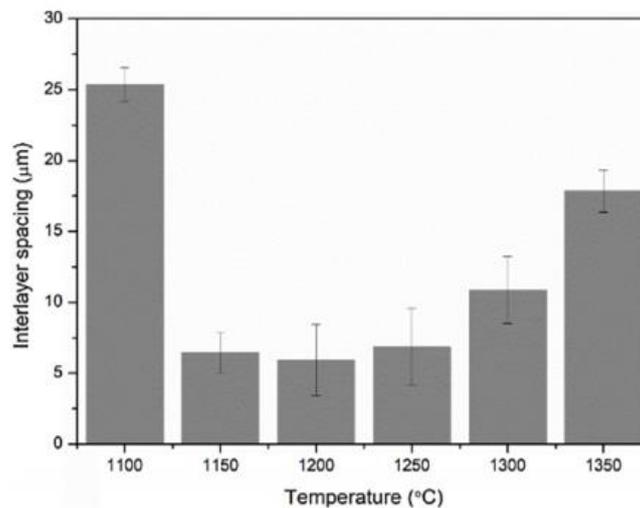

Figure 8.11 : Variation of interlayer spacing according to sintering temperature [15]

A magnification has been made to see the dispersion and combination of particles by SEM (*Figure 8.12*). These SEM images showed that even after sintering, alumina particles are weakly combined and that large particles are surrounded by smaller particles randomly scattered and attached to each other. Nevertheless, it seemed that the higher the sintering temperature, the more compact the intergranular bond is, and therefore there are fewer voids and pores. Thus, when the sintering temperature reaches relatively high values, such as 1300°C, most of the particles become interconnected. The authors of the study [15] explained that "when the sintering temperature increases, the vapor pressure increases exponentially and the growth rate accelerates, which densifies the material during sintering." Thus, particles tend to combine at high sintering temperature, while they remain independently dispersed at lower temperature.
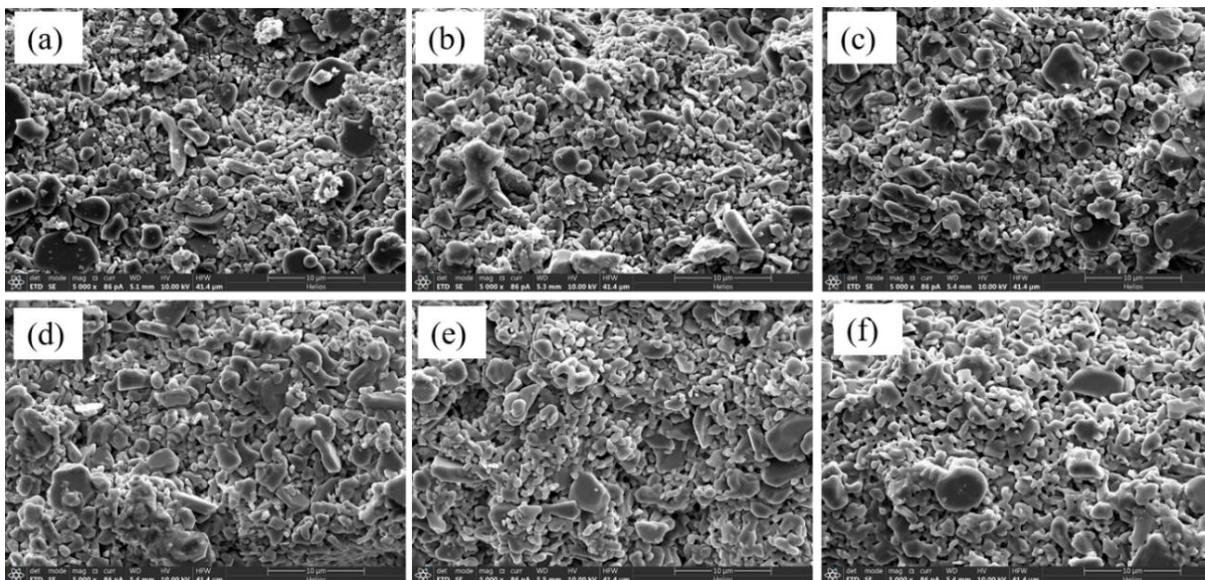
Figure 8.12 : SEM of sintered samples (5000×): (a) 1100ºC; (b) 1150ºC; (c) 1200ºC; (d) 1250ºC; (e) 1300ºC; (f) 1350ºC. [15]

Figure 8.13 shows the average particle size which has been measured for each sample. According to authors "the particle size increases as the sintering temperature increases". This observation seemed to be true until 1250°C but should be nuanced for higher sintering temperature since the figure shows that particle size decreases slightly and might even stabilize when temperature reaches 1300°C. Thus, it would be interesting to repeat these experiments and test higher temperatures to see if there is a stabilization or not.

Figure 8.13 : Particle size of the samples after sintered at different temperatures [15]

Thanks to the further magnification of the samples shown in *Figure 8.14*, it can be seen that large particles tend to form ledges. Indeed, the α-Al2O3 grows into the transition alumina matrix and then thickens via a l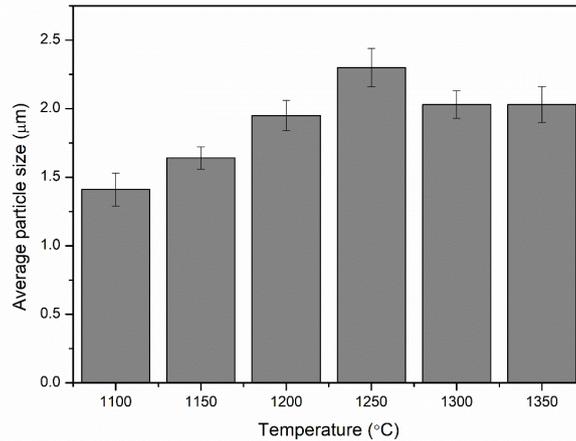edge growth mechanism. It means that large α-Al$_2$O$_3$ particles, which have curved edges, frequently overlap with smaller grains in the transition alumina matrix and this growth is accompanied by a thickening of the α phase.
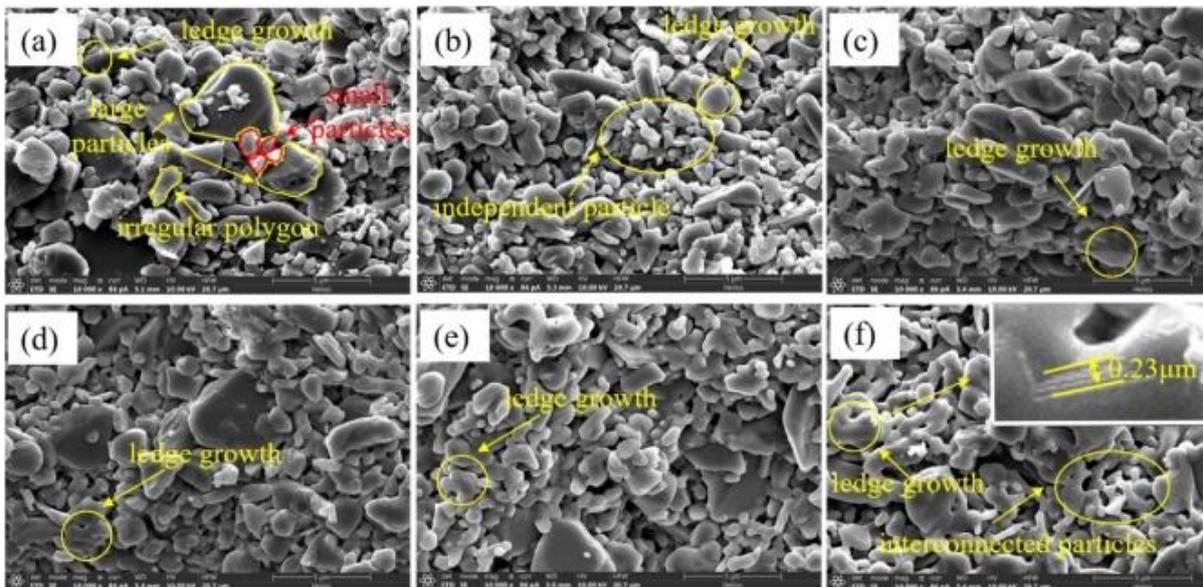
Figure 8.14 : SEM images (10,000× magnification) of samples sintered at (a) 1100, (b) 1150, (c) 1200, (d) 1250, (e) 1300, and (f) 1350 °C. [15]

In this study [15], resulting microstructures presented a relatively uniform distribution of particles. However, microstructures sintered in normal pressures would result in less uniform distribution. Indeed, the driving force when sintering is conducted in vacuum is higher than for normal pressures, especially after the pores are formed. Here, small particles could grow fast due to the high driving force during sintering which have led to the uniform distributed particles.

Finally, thanks to XRD analysis, the researcher showed that all samples are α-alumina and thanks to Raman analysis they showed that the chemical bonds are the same in all samples and thus sintering temperature in vacuum does not affect the chemical bond structure.

8.4.2. Physical properties of samples sintered in vacuum according to sintering temperature

In the study of Li et al. [15], the effects of shrinkage in samples sintered at different temperatures in vacuum was also investigated, as shown in *Figure 8.15*. Shrinkage increases with the sintering temperature and it is different depending on the axis. It is similar along X and Y directions, but it is larger along Z direction (or building direction). Indeed, shrinkage increases by 5% in X and Y directions, while it increases by 8% in Z direction as the sintering temperature increasing from 1100 to 1350 °C. This non uniform shrinkage could be due to the gaps between layers that can be seen in *Figure 8.10*, gaps which result in weaker bonds between the layers along the Z direction.

The weaker the bond, the larger delamination and shrinkage are in Z direction, thus confirming the hypothesis put forward by J. Tarabeux [8] in paragraph 8.2.2.1 which showed that E_{33} was lower than E_{11}.
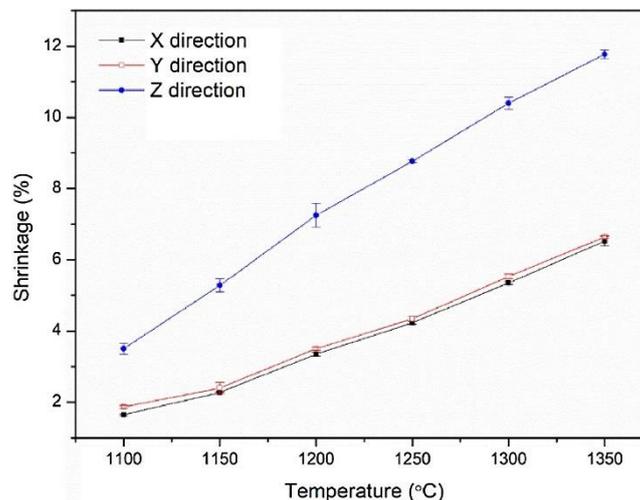
Figure 8.15 : Shrinkage in samples sintered at different temperatures in vacuum [15]

This uneven shrinkage can lead to deformation during sintering and thus, anisotropic shrinkage is dangerous for the integrity of the part. To reduce shrinkage, it is possible to increase powder content in the slurry and to decrease heating rate during sintering. However, increasing powder content can cause problem in the spreading phase since it would increase viscosity and decrease fluidity. Thus, one solution could be to reduce sintering temperature.

8.4.3. Mechanical properties of samples sintered in vacuum according to sintering temperature

It has been shown with bending tests that for samples sintered in vacuum [15], flexural strength increased from 20.3MPa to 138.9 MPa as the sintering temperature increased from 1100 to 1350 °C. Thus, the higher the sintering temperature is, the higher the bending strength is. Furthermore, the authors of the study [15] showed that sample density increases by about 9% and open porosities decrease from 38.7 to 22.8% with increasing sintering temperature from

1100°C to 1350°C. According to Ryskewitsch [53], flexural strength decreases exponentially with increasing porosity and that would explain the results of the study : since higher temperature results in fewer porosity, it can be concluded that flexural strength decreases with increasing porosity.

Open porosity tends to decrease mechanical properties but for some applications, such as ceramic cores, it must be kept. In fact, ceramic cores require a quantity of open porosity > 20 % to ensure air permeability during investment casting and liquid permeability during removal of the part, so a compromise must be done between mechanical properties and porosity rate.

9. Conclusion

Stereolithography is a recent process for manufacturing ceramic parts and as for all additive manufacturing processes, it allows the rapid production of prototypes or complex parts. This method involves the polymerization, layer by layer, of a photo-sensitive suspension using laser energy. The suspension is composed of a photosensitive resin and a high content of powder grains, which will be trapped in the polymer matrix after polymerization. Here, the material studied is alumina, one of the most common material in SLA, used for its great properties such as wear resistance, high electrical resistivity and high mechanical stability. After hardening, a green part is obtained and is submitted to debinding and sintering. Many parameters influence the quality of the final part, from the formulation of the suspension to the choice of process and post-process parameters.

First, it is possible to adapt the raw material and the formulation of the ceramic suspension. Wu et. al. [13] obtained the higher densities with a bimodal powder distribution, by mixing nano and micro sized grains. The small grains tend to agglomerate around the larger grains and thus fill holes, contrary to grains with unimodal distribution. Furthermore, they showed that an exclusive use of micro-sized grains was not appropriate because it leads to low density.

Then, the choice of parameters during the process is crucial. The combination of different laser speed and laser power values lead to different values of exposure, which is the energy received by the photosensitive system by unit area. J. Tarabeux [8] and K. Cieżki [14] showed that the greater the value of exposure is, the higher the stress at break is. In the same way, the greater the value of exposure is, the stiffer the part is, with the increase of Young's modulus. Furthermore, Young's modulus along printing direction Z is always lower than Young's modulus along X or Y direction, meaning that samples produced by SLA are transverse isotropic. This difference can be explained by the delamination present on microstructure between layers along Z axis, which weakens the part along this direction [15].

Li et al. [16] showed that for thin layers (30μm), the curing of each recoating layer is sufficient since no interface can be seen in the microstructure. This is not true for thicker layers. These results show that the thicker the layers are, the greater the risk of cracking along the recoating direction is. Moreover, for the thickest layer tested (120 μm), the distribution of grains in the microstructure is not uniform and grain powders tend to agglomerate, resulting in a rougher morphology. Porosity becomes critical when the layer thickness is 90μm and above. Shrinkage is not different among samples but it is always greater in Z direction. Regarding hardness and stiffness, they both decrease with the increase of layer thickness but not in a significant way for hardness, while Young's modulus decreases about 80Mpa from LT30 to LT120, because of the decrease of density.

Finally, post-process parameters must be studied carefully, from the drying to the debinding and sintering. Zhou et al. [18] showed that to dry parts via a liquid desiccant (PEG) was more adapted since with this drying method shrinkage was homogeneous and no deformation appeared, contrary to traditional air drying. They also obtained higher density.

Regarding debinding, an appropriate two-step debinding (vacuum pyrolysis step followed by pyrolysis in air.) is better than a single vacuum pyrolysis which is better than a simple pyrolysis. Indeed, no defects appeared with the two-step debinding. Furthermore, Wu et. al. [13] showed that a vacuum debinding provides higher density.

Regarding sintering, Li et al. [15] tested sintering in vacuum at different temperature. They noticed that the interlaying distance in the microstructure first decreases, reaching a minimum value for sintering at 1200 °C, and then increases as the sintering temperature increases. Moreover, the higher the sintering temperature is, the higher the bending strength is, thanks to the decrease of porosity and shrinkage increases with the sintering temperature. Thus, in the conditions used in this study, the best sintering temperature is 1150°C, which allows to have the smallest interlayer spacing, a small shrinkage and a correct resistance.

Apart from the stress at break in J. Tarabeux thesis [8], all results are of the same order of magnitude as the results found for traditional process, meaning that it is a reliable process for manufacturing alumina parts.

It is difficult, if not impossible to compare the different studies present in literature and thus to give precise values to use in order to have the best characteristics. Indeed, researchers use different conditions: resins with different formulation, different type of post-processing, etc. Moreover, most of the time they do not specify the parameters used, such as the laser power and speed, etc. However, in theory, to compare significant results, conditions must be the same. Thus, in the future, it would be interesting to perform some experiments in repeatable and comparable conditions, with at least same amount of powder in the suspension, same debinding and sintering parameters, etc.

It is important to notice that industrialists will often have to choose between performance and building time. For instance, parts with thin layers present better mechanical properties but are much longer to produce, as well as using two-step debinding stage.

References

[1] C. Hinczewski, 'Stéréolithographie pour la fabrication additive', Institut national polytechnique de Lorraine, 1998.

[2] P. Auerkari, 'Mechanical and physical properties of engineering alumina ceramics', p. 26.

[3] F. Azarmi and I. Sevostianov, 'Evolution of thermo-mechanical properties in the process of alumina manufacturing using laser stereolithography technique', *International Journal of Engineering Science*, vol. 144, Nov. 2019, doi: 10.1016/j.ijengsci.2019.103125.

[4] L. Iuliano, 'Tecniche di fabbricazione additiva'. Ecole Polytechnique de Turin, 2018.

[5] C. Hull, 'Apparatus for production', 4575330.

[6] T. Chartier, V. Pateloup, and C. Chaput, 'Élaboration de pièces céramiques par fabrication additive', *Techniques de l'Ingénieur*. p. 32, 2018.

[7] C. Hinczewski, 'Stéréolithographie pour la fabrication additive', Institut national polytechnique de Lorraine, 1998.

[8] J. Tarabeux, 'Prédiction de la polymérisation et des propriétés mécaniques - Optimisation du procédé', Université de Limoges, IRCER - Institut de Recherche sur les Céramiques, 2019.

[9] A. R. Olszyna, P. Marchlewski, and K. J. Kurzydłowski, 'Sintering of high-density, high-purity alumina ceramics', *Ceramics International*, vol. 23, no. 4, pp. 323–328, Jan. 1997, doi: 10.1016/S0272-8842(96)00031-4.

[10] P. Auerkari, 'Mechanical and physical properties of engineering alumina ceramics', p. 26.

[11] J. Tarabeux, V. Pateloup, P. Michaud, and T. Chartier, 'Development of a numerical simulation model for predicting the curing of ceramic systems in the stereolithography process', *Journal of the European Ceramic Society*, vol. 38, no. 11, Art. no. 11, Sep. 2018, doi: 10.1016/j.jeurceramsoc.2018.03.052.

[12] S. P. Gentry and J. W. Halloran, 'Depth and width of cured lines in photopolymerizable ceramic suspensions', *Journal of the European Ceramic Society*, vol. 33, no. 10, Art. no. 10, Sep. 2013, doi: 10.1016/j.jeurceramsoc.2013.02.033.

[13] H. Wu *et al.*, 'Effect of the particle size and the debinding process on the density of alumina ceramics fabricated by 3D printing based on stereolithography', *Ceramics International*, vol. 42, no. 15, pp. 17290–17294, Nov. 2016, doi: 10.1016/j.ceramint.2016.08.024.

[14] K. Ciężki, 'Study of the mechanical properties of dense ceramic parts obtained by stereolithograpy', IRCER - Institut de Recherche sur les Céramiques, Rapport de stage Master, 2019.

[15] H. Li *et al.*, 'Evolution of the microstructure and mechanical properties of stereolithography formed alumina cores sintered in vacuum', *Journal of the European Ceramic Society*, p. S0955221919307927, Nov. 2019, doi: 10.1016/j.jeurceramsoc.2019.11.047.

[16] W. Li, W. Liu, F. Qi, Y. Chen, and Z. Xing, 'Determination of micro-mechanical properties of additive manufactured alumina ceramics by nanoindentation and scratching', *Ceramics International*, vol. 45, no. 8, pp. 10612–10618, Jun. 2019, doi: 10.1016/j.ceramint.2019.02.128.

[17] F. Azarmi and A. Amiri, 'Microstructural evolution during fabrication of alumina via laser stereolithography technique', *Ceramics International*, vol. 45, no. 1, Art. no. 1, Jan. 2019, doi: 10.1016/j.ceramint.2018.09.163.

[18] M. Zhou *et al.*, 'Preparation of a defect-free alumina cutting tool via additive manufacturing based on stereolithography – Optimization of the drying and debinding processes', *Ceramics International*, vol. 42, no. 10, pp. 11598–11602, Aug. 2016, doi: 10.1016/j.ceramint.2016.04.050.

[19] P. Lefort, 'Céramiques - Caractéristiques et technologies', p. 24, 2018.

[20] J. Poirier, 'Céramiques réfractaires', *Techniques de l'Ingénieur*. p. 26, 2014.

[21] S. Lamouri *et al.*, 'Control of the γ-alumina to α-alumina phase transformation for an optimized alumina densification', *Boletín de la Sociedad Española de Cerámica y Vidrio*, vol. 56, no. 2, pp. 47–54, Mar. 2017, doi: 10.1016/j.bsecv.2016.10.001.

[22] 'Focus application Alumine'. http://guichon-vannes.com/focus-application-alumine/ (accessed May 19, 2020).

[23] P. Blazy and E.-A. Jdid, 'Métallurgie extractive - Pyrométallurgie', *Techniques de l'Ingénieur*. p. 34, Mar. 10, 1998.

[24] P. B. Parikh, 'Alumina Ceramics: Engineering Applications and Domestic Market Potential', *Transactions of the Indian Ceramic Society*, vol. 54, no. 5, pp. 179–184, Jan. 1995, doi: 10.1080/0371750X.1995.10804716.

[25] D. Mauduit, 'Caractérisation et modélisation probabiliste de la rupture fragile de l'AlSi CE9F et d'une alumine cofrittée pour composants embarqués à applications spatiales', Université de Toulouse, 2017.

[26] A. A. Griffith, 'VI. The phenomena of rupture and flow in solids', *Phil. Trans. R. Soc. Lond. A*, vol. 221, no. 582–593, Art. no. 582–593, Jan. 1921, doi: 10.1098/rsta.1921.0006.

[27] Y. Xu, L. Cheng, L. Zhang, D. Yan, and C. You, 'Optimization of sample number for Weibull function of brittle materials strength', *Ceramics International*, vol. 27, no. 2, Art. no. 2, Jan. 2001, doi: 10.1016/S0272-8842(00)00056-0.

[28] F. Hild, 'De la rupture des materiaux à comportement fragile', Université Pierre et Marie Curie, Paris VI, 1992.

[29] S. K. Hubadillah *et al.*, 'Fabrications and applications of low cost ceramic membrane from kaolin: A comprehensive review', *Ceramics International*, vol. 44, no. 5, pp. 4538–4560, Apr. 2018, doi: 10.1016/j.ceramint.2017.12.215.

[30] sachin, 'Plastic State Forming', *D'Source*, Sep. 14, 2015. http://www.dsource.in/course/ceramics/plastic-state-forming (accessed May 25, 2020).

[31] 'Cold isostatic pressing', *OpenLearn*. https://www.open.edu/openlearn/science-maths-technology/engineering-technology/manupedia/cold-isostatic-pressing (accessed May 25, 2020).

[32] 'Additive manufacturing of ceramics | CTTC'. https://www.cttc.fr/en/videos-downloads/additive-manufacturing-of-ceramics/ (accessed Sep. 11, 2020).

[33] F. Laverne, F. Segonds, and P. Dubois, 'Fabrication additive - Principes généraux', *Techniques de l'Ingénieur*. p. 20, 2018.

[34] R. Vaidya and S. Anand, 'Optimum Support Structure Generation for Additive Manufacturing Using Unit Cell Structures and Support Removal Constraint', *Procedia Manufacturing*, vol. 5, pp. 1043–1059, 2016, doi: 10.1016/j.promfg.2016.08.072.

[35] D. Deradjat and T. Minshall, 'Decision trees for implementing rapid manufacturing for mass customisation', *CIRP Journal of Manufacturing Science and Technology*, vol. 23, pp. 156–171, Nov. 2018, doi: 10.1016/j.cirpj.2017.12.003.

[36] 'What is Sheet Lamination?', *Engineering Product Design*. https://engineeringproductdesign.com/knowledge-base/sheet-lamination/ (accessed Jul. 20, 2020).

[37] S. Agarwala, G. Guo Liang, and W. Y. Yeong, 'Optimizing Aerosol Jet Printing Process of Silver Ink for Printed Electronics', Jan. 2017.

[38] 'PROFORM prototypage rapide, stéréolithographie, impression 3D, moulage sous vide, prototypes - Stéréolithographie, microstéréolithographie, impression 3D, prototypes', May 11, 2020. http://www.proform.ch/fr/procedes/stereolithographie.html (accessed May 11, 2020).

[39] S. Forget, 'Optique des lasers & faisceaux gaussiens', Laboratoire de Physique des Lasers, Université Paris Nord/13.

[40] C. Hinczewski, S. Corbel, and T. Chartier, 'Ceramic suspensions suitable for stereolithography', *Journal of the European Ceramic Society*, vol. 18, pp. 583–590, 1998.

[41] M. Ilie, J.-C. Kneip, S. Matteï, A. Nichici, C. Roze, and T. Girasole, 'Laser beam scattering effects in non-absorbent inhomogenous polymers', *Optics and Lasers in Engineering*, vol. 45, no. 3, pp. 405–412, Mar. 2007, doi: 10.1016/j.optlaseng.2006.07.004.

[42] G. V. Salmoria, C. H. Ahrens, V. E. Beal, A. T. N. Pires, and V. Soldi, 'Evaluation of post-curing and laser manufacturing parameters on the properties of SOMOS 7110 photosensitive resin used in stereolithography', *Materials & Design*, vol. 30, no. 3, Art. no. 3, Mar. 2009, doi: 10.1016/j.matdes.2008.05.016.

[43] J. W. Halloran, 'Ceramic Stereolithography: Additive Manufacturing for Ceramics by Photopolymerization', *Annu. Rev. Mater. Res.*, vol. 46, no. 1, pp. 19–40, Jul. 2016, doi: 10.1146/annurev-matsci-070115-031841.

[44] M. Pfaffinger, G. Mitteramskogler, R. Gmeiner, and J. Stampfl, 'Thermal Debinding of Ceramic-Filled Photopolymers', *MSF*, vol. 825–826, pp. 75–81, Jul. 2015, doi: 10.4028/www.scientific.net/MSF.825-826.75.

[45] D. Bernache-Assollant and J.-P. Bonnet, 'Frittage : aspects physico-chimiques - Partie 1 : frittage en phase solide', *Techniques de l'Ingénieur*. p. 25, 2005.

[46] D. Dopfer *et al.*, 'Adhesion mechanisms between water soluble particles', *Powder Technology*, vol. 238, pp. 35–49, Apr. 2013, doi: 10.1016/j.powtec.2012.06.029.

[47] P. Gonzalez, E. Schwarzer, U. Scheithauer, N. Kooijmans, and T. Moritz, 'Additive Manufacturing of Functionally Graded Ceramic Materials by Stereolithography', *JoVE*, no. 143, p. 57943, Jan. 2019, doi: 10.3791/57943.

[48] K. Li and Z. Zhao, 'The effect of the surfactants on the formulation of UV-curable SLA alumina suspension', *Ceramics International*, vol. 43, no. 6, pp. 4761–4767, Apr. 2017, doi: 10.1016/j.ceramint.2016.11.143.

[49] K. Zhang *et al.*, 'High solid loading, low viscosity photosensitive Al2O3 slurry for stereolithography based additive manufacturing', *Ceramics International*, vol. 45, no. 1, pp. 203–208, Jan. 2019, doi: 10.1016/j.ceramint.2018.09.152.

[50] G. Tarì, J. M. F. Ferreira, A. T. Fonseca, and O. Lyckfeldt, 'Influence of particle size distribution on colloidal processing of alumina', *Journal of the European Ceramic Society*, vol. 18, no. 3, pp. 249–253, Jan. 1998, doi: 10.1016/S0955-2219(97)00113-1.

[51] W. Piekarczyk and D. Kata, 'Methodology for determining material constants of anisotropic materials belonging to the transversely isotropic system by ultrasound method', *Ultrasonics*, vol. 71, pp. 199–204, Sep. 2016, doi: 10.1016/j.ultras.2016.06.015.

[52] S. M. Jeong, S. E. Park, and H. L. Lee, 'Fracture behaviour of alumina ceramics by biaxial ball-on-3-ball test', *Journal of the European Ceramic Society*, vol. 22, no. 7, Art. no. 7, Jul. 2002, doi: 10.1016/S0955-2219(01)00430-7.

[53] J. Yu, Y. Wang, F. Zhou, L. Wang, and Z. Pan, 'Laser remelting of plasma-sprayed nanostructured Al 2 O 3 –20 wt.% ZrO 2 coatings onto 316L stainless steel', *Applied Surface Science*, vol. 431, pp. 112–121, Feb. 2018, doi: 10.1016/j.apsusc.2017.06.204.

[54] 'Étude d'un séisme | Annabac', May 11, 2020. https://www.annabac.com/annales-bac/etude-d-un-seisme (accessed May 11, 2020).

[55] K. Boussois, 'Céramiques silicatées à résistance mécanique et ténacité élevées', Faculté des Sciences et Techniques, Limoges, 2013.

[56] A. R. Boccaccini, 'Dependence of ceramics fracture properties on porosity', *Journal of Materials Science Letters*, vol. 16, no. 8, Art. no. 8, 1997, doi: 10.1023/A:1018596023077.

[57] J. D. Lord and R. Morrell, 'Measurement Good Practice Guide No. 98 Elastic Modulus Measurement', p. 100.

[58] E. De Bilbao, E. Blond, C. Michel, T. Cutard, and J. Poirier, 'Identification du module d'Young de matériaux réfractaires à base SiC', p. 6, 2010.

[59] 'Scanning Electron Microscope (SEM)', *Bioscience Notes*, Jun. 16, 2018. http://www.biosciencenotes.com/scanning-electron-microscope-sem/ (accessed Sep. 15, 2020).

[60] H. Ali, 'Study of surface passivation behavior of crystalline silicon solar cells', 2017, doi: 10.13140/RG.2.2.16990.28489.

[61] 'Diffraction des rayons X, analyse XRD'. https://www.eaglabs.fr/cm/xrd.html (accessed Sep. 15, 2020).

[62] 'Bragg's Law'. http://hyperphysics.phy-astr.gsu.edu/hbase/quantum/bragg.html (accessed Sep. 15, 2020).

[63] B. Wunderlich, 'Thermal Analysis', in *Encyclopedia of Materials: Science and Technology*, Elsevier, 2001, pp. 9134–9141.

[64] C. De Blasio, 'Thermogravimetric Analysis (TGA)', in *Fundamentals of Biofuels Engineering and Technology*, Cham: Springer International Publishing, 2019, pp. 91–102.

10. Appendices

Appendix 1: Experimental and analysis methods

Appendix 1.1: Archimedean buoyancy method

The Archimedean thrust method can be used, according to standard NF EN 993-1.

The dry samples are weighed and placed in a vacuum chamber at a pressure of 0.7 mbar for 15 min. Water is then poured into the chamber to cover the samples and the pressure is lowered again for 30 min to allow water to enter the pores. The samples are weighed again, once in the water, and a second time just after removal from the water, to obtain the mass of the sample with the pores filled with water.

The apparent density ρ_b (in g/cm^3) is given by the equation:

$$\rho_b = \frac{m_1}{m_3 - m_2} \times \rho_{liq} \tag{10.1}$$

Open porosity, Π_a, total porosity Π_t and closed porosity Π_f, expressed as a percentage by volume, are given by the equations:

$$\Pi_a = \frac{m_3 - m_1}{m_3 - m_2} \times 100 \tag{10.2}$$

$$\Pi_t = \frac{\rho_t - \rho_b}{\rho_t} \times 100 \tag{10.13}$$

$$\Pi_f = \Pi_t - \Pi_a \tag{10.4}$$

With:

m_1, m_2, and m_3, respectively the mass of the dry test piece, the apparent mass of the immersed test piece, and the mass of the soaked test piece, expressed in grams.

ρ_t and ρ_{liq}, respectively the absolute density of the product and the density of the liquid used for immersion, expressed in g/cm^3.

Appendix 1.2: Ultrasound method for Young's modulus measurement

The method of determining the elastic constants of a material by ultrasound is a non-destructive method. It is based on measurements of propagation velocities of an ultrasonic wave passing through the sample [51].

Ultrasonic waves are mechanical vibrations of the medium with a high frequency ranging from 20 kHz to several hundred kHz. The use of these high frequencies makes it possible to consider the sample as "infinite", because the resulting wavelength is negligible compared to the dimensions of the sample, which is a condition for method validation.

In this method, both longitudinal (V_L) and transverse (V_T) propagation velocities are measured. According to [51] by measuring V_L and V_T, it is possible to calculate the transverse and longitudinal Young's modulus of an anisotropic material.

The longitudinal wave propagates in the direction of the vibration while the transverse wave propagates perpendicularly to that direction (*Figure 10.1*).
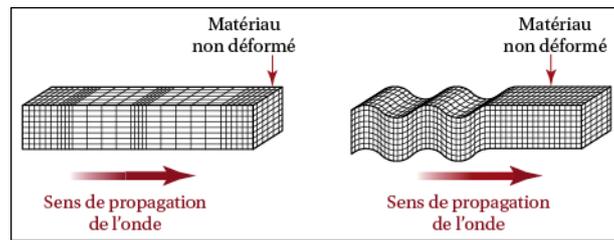

Figure 10.1 : Diagram of a longitudinal (left) and transverse (right) wave [54]

Considering a transverse isotropy of the material, the generalized Hooke's law is written:

$$[\sigma] = [C][\varepsilon] = \begin{bmatrix} C_{11} & C_{12} & C_{13} & 0 & 0 & 0 \\ C_{12} & C_{11} & C_{13} & 0 & 0 & 0 \\ C_{13} & C_{13} & C_{33} & 0 & 0 & 0 \\ 0 & 0 & 0 & C_{44} & 0 & 0 \\ 0 & 0 & 0 & 0 & C_{44} & 0 \\ 0 & 0 & 0 & 0 & 0 & C_{66} \end{bmatrix} \begin{bmatrix} \varepsilon_{11} \\ \varepsilon_{22} \\ \varepsilon_{23} \\ \gamma_{23} \\ \gamma_{31} \\ \gamma_{12} \end{bmatrix} \qquad (10.5)$$

Where [C] is the stiffness matrix.

The coefficients Cij are expressed as a function of the wave velocities P and S (19) :

$$C_{11} = \rho V^2_{1/1} \qquad (10.6)$$

$$C_{33} = \rho V^2_{3/3} \qquad (10.7)$$

$$C_{44} = \rho V^2_{1/3} \qquad (10.8)$$

$$C_{66} = \rho V^2_{1/2} = \rho V^2_{2/1} \qquad (10.9)$$

$$C_{12} = C_{11} - 2C_{66} = \rho[V^2_{1/1} + 2\, V^2_{1/3} - 4V^2_{13/2}] \qquad (10.10)$$

$$C_{13} = [(C_{11} - C_{44} - 2\rho V^2_{13/13})\, (C_{44} + C_{33} - 2\, \rho V^2_{13/13})]^{1/2} - C_{44} \qquad (10.11)$$

Where :

$V_{1/1}$- Velocity of a longitudinal wave propagating in the x-direction and with a movement of particles in the x-direction

$V_{1/2}$- Velocity of a transverse wave propagating in the x-direction and with a particle motion in the y-direction

$V_{13/2}$- Velocity of a transverse wave propagating along an x-z plane (angle of 45°) with a movement of the particles in the y-direction

$V_{13/13}$- Velocity of transverse or longitudinal waves propagating in the x-z plane (45° angle) with a particle movement in the x-z plane

For a transverse isotropic material, certain velocities are equal:

$$V_{1/1} = V_{2/2} \tag{10.12}$$

$$V_{1/2} = V_{2/1} \tag{10.13}$$

$$V_{1/3} = V_{3/1} = V_{2/3} = V_{3/2} \tag{10.14}$$

$$V_{13/13} = V_{23/23} \tag{10.15}$$

$$V_{13/2} = V_{23/1}. \tag{10.16}$$

As the equations of the previous coefficients show the density ρ, it is necessary to measure the density, taking into account possible porosities (with the Archimede's method showed in appendix 1.1).

Finally, the Young's modulus E_{11}, which corresponds to the Young's modulus in the direction perpendicular to the printing direction, and E_{33}, which corresponds to the Young's modulus in the direction of part construction, are expressed as:

$$E\perp_{(11)} = \frac{(C_{11}-C_{12})(C_{11}C_{33}+C_{12}C_{33}-2C^2_{13})}{C_{11}C_{33}+C^2_{13}} \tag{10.17}$$

$$E_{\parallel (33)} = \frac{C_{33}(C_{11}+C_{12})-2C^2_{13})}{C_{11}+C_{12}} \tag{10.18}$$

Appendix 1.3: Biaxial bending's method to calculate maximum stress at break

The method used in the laboratory is the ball-on-ring method. It consists in depositing and centring a circular sample on a support ring and applying a load P to the centre of the sample using a ball-on-ring tip.
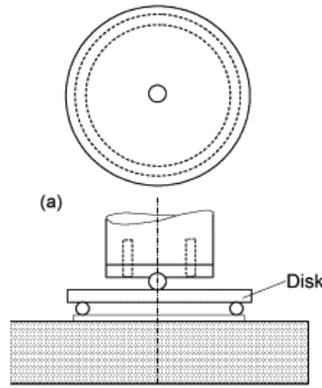
Figure 10.2: Diagram of the biaxial ball-on-ring method [55]

The load is assumed to be uniformly distributed and the test is performed according to the standard ASTM F394-78. According to [55], the value of the maximum stress at break can be calculated using the following expression :

$$\sigma_{max} = \frac{3P(1+\nu)}{4\pi e^2}\left(1 + 2\ln\left(\frac{A}{B}\right) + \left(\frac{1-\nu}{1+\nu}\right)\left(1 - \frac{B^2}{2A^2}\right)\frac{A^2}{C^2}\right) \qquad (10.19)$$

With :

P the load at break (N); ν the Poisson's ratio (0.25 for alumina); e the thickness of the sample (mm)

A = 20 mm - the radius of the support ring; B = 10 mm - the radius of the bale; C = the radius of the sample (disc)

Appendix 1.4: Four-point bending test for determination of maximum stress and Young's modulus

There are two types of bending tests: three-point and four-point. The four-point bending test has the advantage that the load is not applied in the area of failure. The advantage of the four-point bending test is that the load is not applied in the area of failure, since a central support can damage the specimen and erroneous results can lead to early failure of the specimen.

For the four-point bending tests, a strip of the test material is placed on two supports and an increasing force is applied at two points equidistant from the edge (d_1 in) until failure.
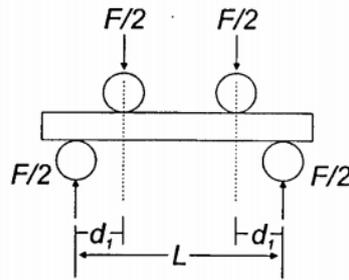
Figure 10.3 : Diagram of the four-point bending test [56]

The maximum stress [57] and Young's modulus [58] can be calculated using the following equations:

$$\sigma_{max} = \frac{3 F_m\, d_1}{b h^2} \quad (10.20)\,; \qquad E = \frac{F_m}{\Delta y}\, \frac{1}{8 b h^3}(L\text{-}l)(2L^2\text{+}2Ll\text{-}l^2) \quad (10.21)$$

With:

F_m = the maximum applied force (N)

d_1 = the distance between the outer support and the cylindrical loading arm (mm)

b = the width of the sample (mm)

h = the thickness of the sample (mm)

Δy = sample deflection (arrow)

L = the length between the two lower supports (mm)

$l = L - 2d_1$ = the length between the two upper supports (mm)

Appendix 1.5: Nanoindentation tests

The indentation test consists in making a tip, also called "indenter" or "penetrator", of known geometry and mechanical properties penetrate into a material to deduce its mechanical properties. It consists of measuring the local resistance of a material to plastic deformation. The effort applied F is known and removed after a certain amount of time. After removing the load, a residual imprint remains in the material.

Vickers hardness and Young's modulus can be calculated according the following equations:

$$H = \frac{F_{Max}}{A} \hspace{6cm} (10.22)$$

$$E_r = \frac{\sqrt{\pi}}{2}\, \frac{S}{\sqrt{A}} \hspace{5.5cm} (10.23)$$

where H is the hardness, F_{Max} is the maximum load, A is the projected contact area at maximum load (*Figure 10.4*).
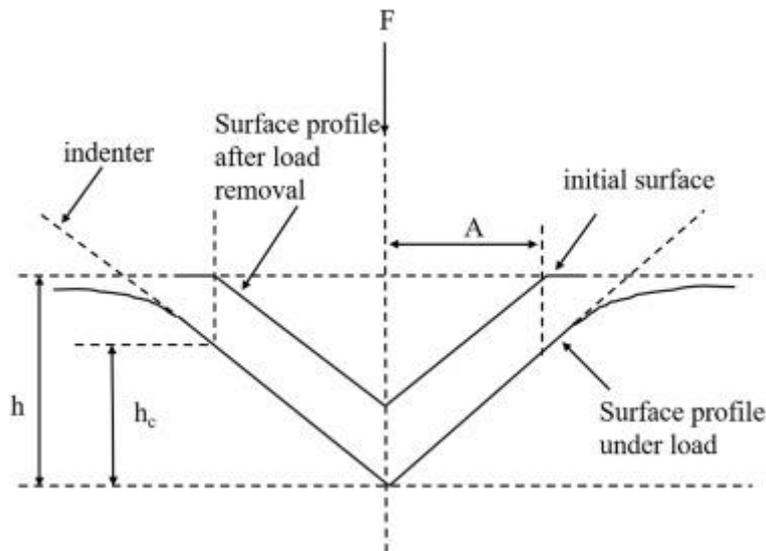

Figure 10.4 : Nanoindentation schematic. [59]

Appendix 1.6 : SEM and EDS

The Scanning Electron Microscope (SEM) is a microscope for observing the topography of surfaces. As shown in *Figure 10.5,* it is composed of [59]:

- An electronic column (kept under vacuum)

- An electron gun comprising a source and a high-voltage device for accelerating primary electrons

- A set of electron lenses (the condensers) designed to form an electron beam.

- A lens, the "final condenser", and a diaphragm that allows a fine electron beam to be focused on the surface to be examined, as parallel as possible.

- A deflection device controlled by a scanning generator

- A mobile plate to carry the sample to be analysed

- An electron detector (mainly secondary) and a signal amplification device

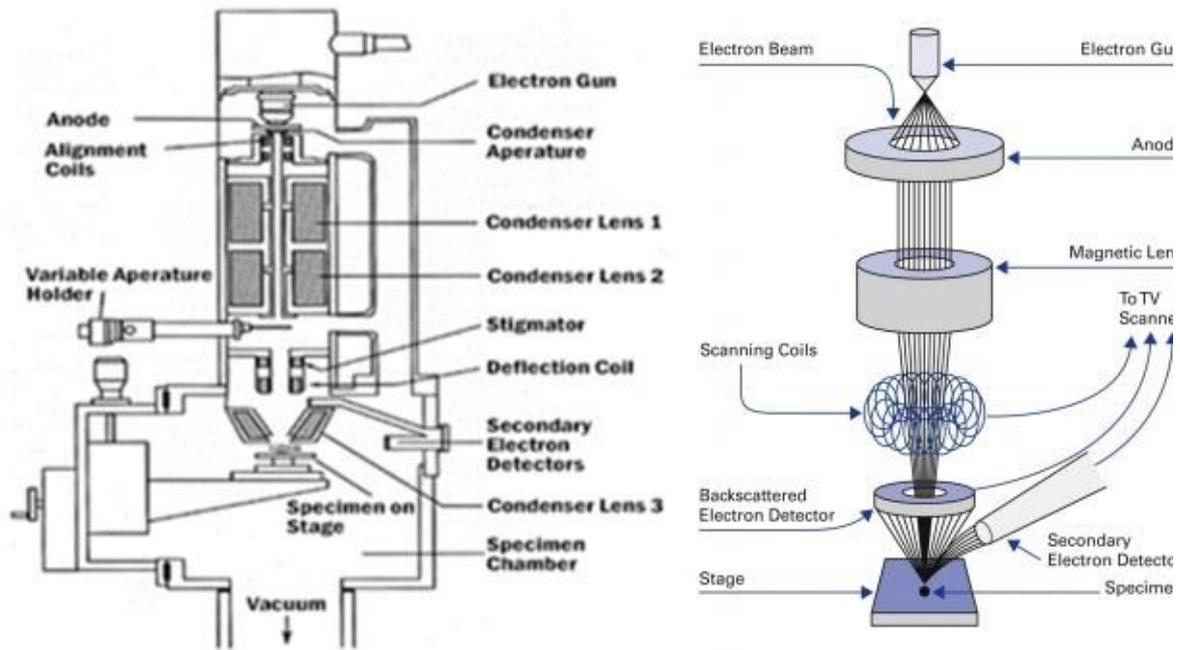- An image display system synchronously coupled to the same scan generator

Figure 10.5 : SEM drawing [59]

Primary electrons in the form of a beam are bombarded onto the surface to be analysed. These electrons will interact with the matter to be analysed and this will re-emit several types of electrons: backscattered electrons, secondary electrons and Auger electrons (*Figure 10.6*).
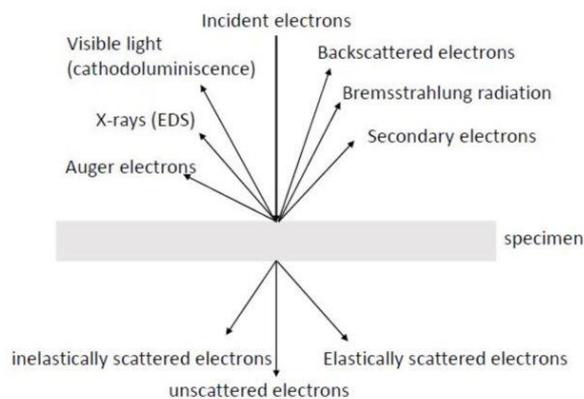

Figure 10.6 : Electron interaction with matter [60]

In the case of the SEM, it is mainly the secondary electrons that are analysed. The intensity of the signal detected by the secondary electron detectors depends on the nature of the sample being analysed and its topography at the point in question. It is thus possible to obtain a map of the scanned area.

The EDS (Energy Dispersive X-ray Spectrometry) detector makes it possible to identify the elements contained in matter, by analysing the photons (X-rays) emitted by matter following electronic excitation. These are sorted according to their energy, which makes it possible to recognise the elements with which the electrons have interacted. The heavier a chemical element is, the brighter it appears on the screen.

Appendix 1.7: XRD

X-ray diffractometry (XRD) is an analytical technique based on the diffraction of X-rays by matter, especially when it is crystalline [61]. The principle is as follows: the X-ray beams are sent to the sample in which they are deflected by the atoms (*Figure 10.7*). These diffracted beams interfere with each other, leading to the production of an intense signal in specific areas of space. This signal is collected by the detector, and plotted as a curve (diffractogram) that has peaks at specific diffraction angles. The position of these peaks is a true signature of the arrangement of atoms within a crystal (distance between atoms, between intracrystalline planes). The empirical relationship between the angles at which peaks are observed and the distances between atomic planes is Bragg's law, which is given by:

$$2d\sin\theta = n\lambda \tag{10.24}$$

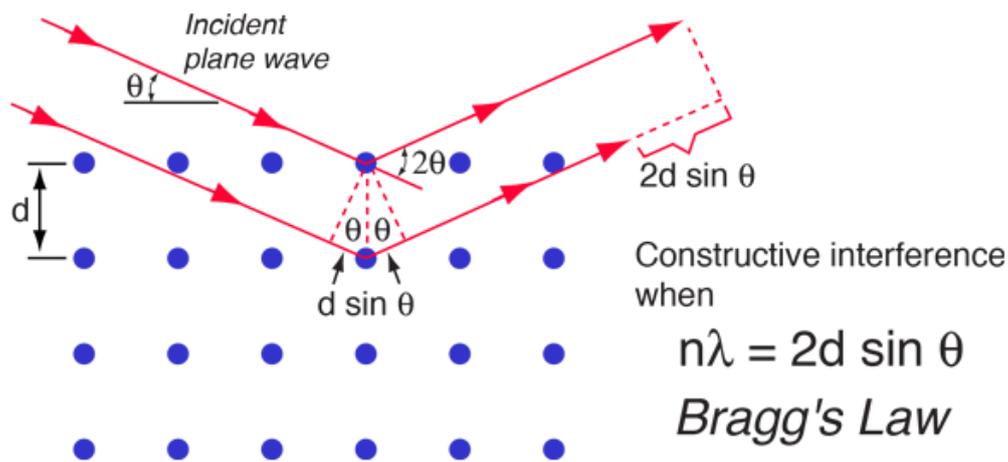where *n* is a positive integer and λ is the wavelength of the incident wave.

Figure 10.7 : Illustration of Bragg's law [62]

X-ray diffraction makes it possible to distinguish products with the same chemical composition but with different atomic arrangements. For example, calcium carbonates such as calcite and aragonite, which have the same chemical formula ($CaCO_3$), have different diffraction patterns. On the other hand, phases of different chemical nature but whose atoms are arranged in the same arrangement have great similarities, i.e. diffraction peaks located at the same angular positions.

To summarize, X-ray diffraction is based on the recording of a diffractogram and on the analysis of the peaks of this diagram which allows the crystallites present in the sample to be characterised from the following elements:

- Position of the peaks: qualitative analysis, identification of crystalline phases present

- Peak widths: crystallite size and shape, internal constraints

-   Peak intensities: chemical composition estimation, quantitative analysis, preferential orientation

For example, the XRD patterns obtained from samples sintered at different temperatures in vacuum from the study of Li. et al. [15] can be seen in the *Figure 10.8*.
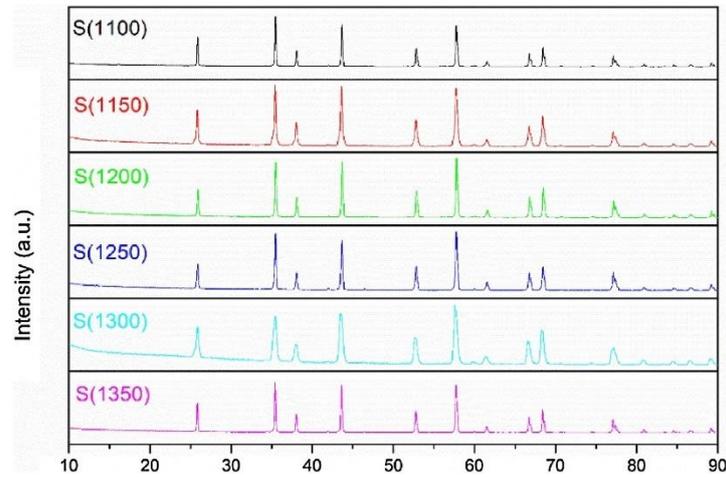

Figure 10.8 : XRD patterns from samples sintered at different temperatures in vacuum [15]

Appendix 1.8: TGA

The aim of thermogravimetric analysis (TGA) or thermogravimetry is to characterise materials by direct measurement of their mass as a function of temperature and/or time. An apparatus typically consists of a sealed chamber for controlling the atmosphere of the sample, an oven for managing the temperature, a weighing module (microbalance), a thermocouple for measuring the temperature and a computer for controlling the assembly and recording the data (*Figure 10.9*).
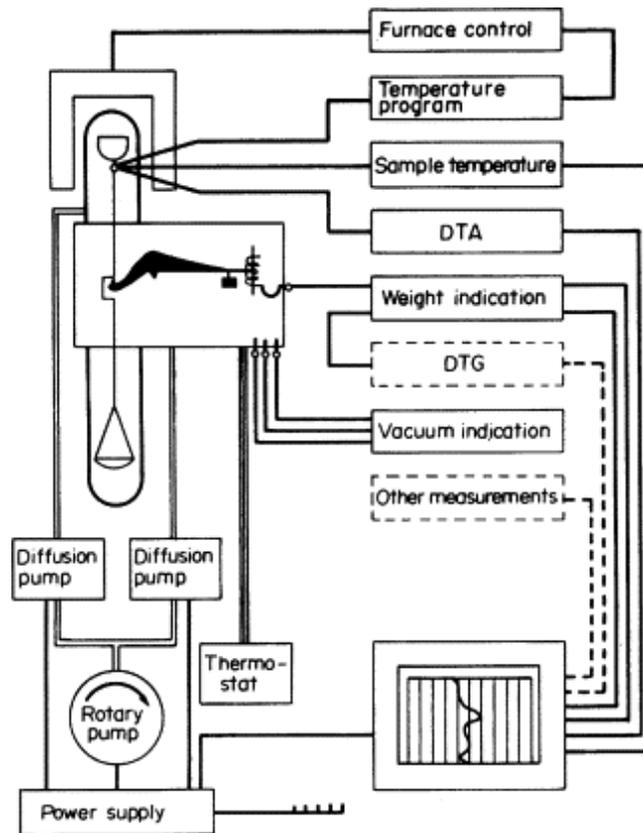
Figure 10.9 : TGA apparatus [63]

The TGA curbe obtained in the study of Wu. et al [13] is shown in the following figure:
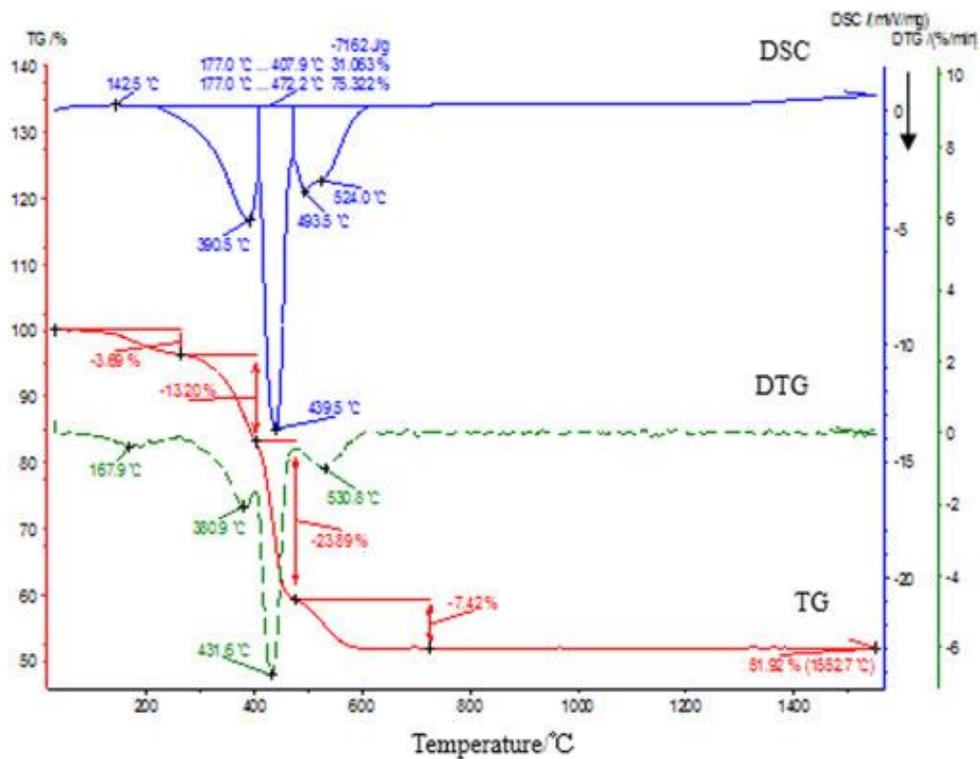

Figure 10.10 : Thermal decomposition behavior of the green bodies. (The DTG curve is the derivative of the TGA curve.).

In figure *Figure 10.10* appears a DSC curve. Differential scanning calorimetry (DSC) monitors heat effects associated with phase transitions and chemical reactions as a function of temperature. It measures the differences in heat exchange between a sample to be analysed and a reference (e.g. air). It is used to determine phase transitions [64]:

- the glass transition temperature (Tg) of amorphous materials: polymers, glasses (inorganic, organic or metallic) and ionic liquids;

- the melting and crystallisation temperatures;

- the enthalpies of reaction, to know the cross-linking rates of certain polymers.

Appendix 2: Particle size distribution and cycles

For information, particles size distribution of Al_2O_3 powders in the study of Li. et al [15] is shown in *Figure 10.11*.
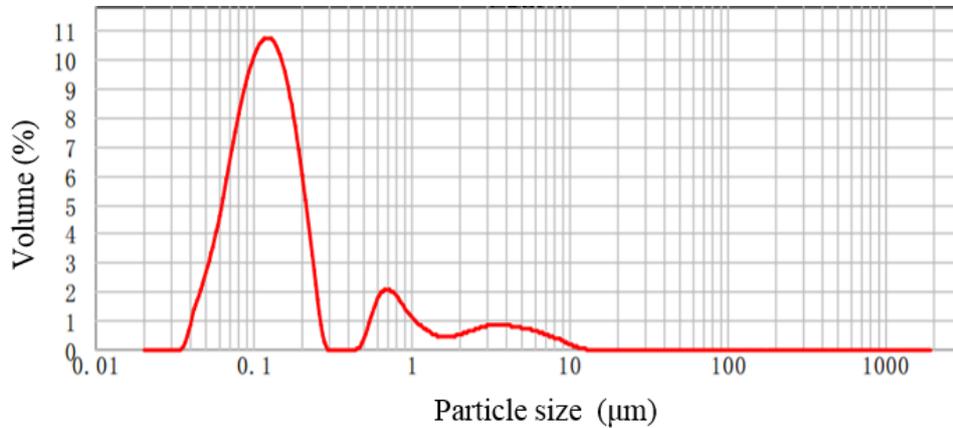

Figure 10.11 : Particle size distribution of Al_2O_3 powders. [15]

Samples from the study of Li. et al [15] where submitted to the debinding from *Figure 10.12 (a)* and to the sintering from *Figure 10.12 (b)*, where the cycle depends on the maximum sintering temperature reached.
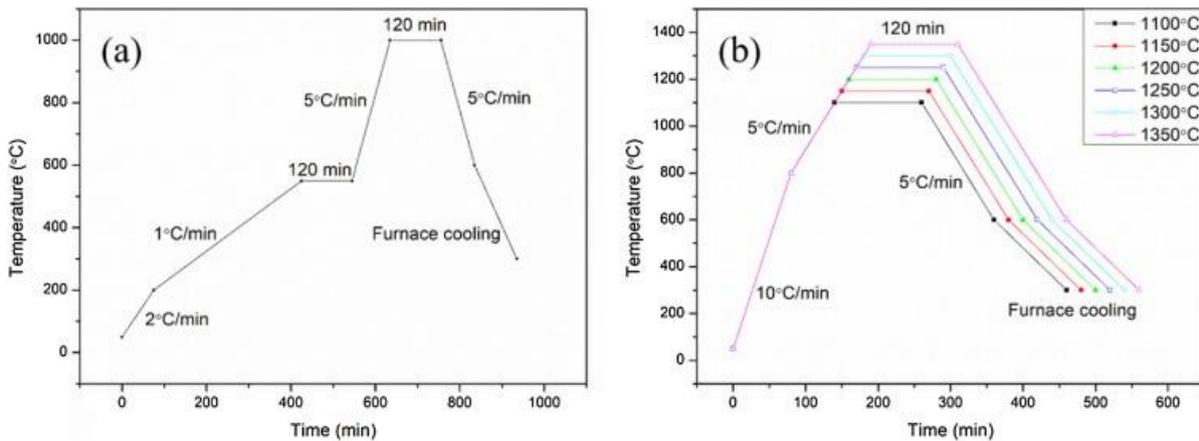

Figure 10.12 : Thermal cycles of green bodies: (a) debinding; (b) sintering [15]